The Effects of Deposit Thermal History on Microstructure Produced by Uniform Droplet Spray Forming

by

Jean-Pei Jeanie Cherng

B.S. Mechanical Engineering
Massachusetts Institute of Technology, 1995

M.S. Mechanical Engineering
Massachusetts Institute of Technology, 1997

Submitted to the Department of Mechanical Engineering
in Partial Fulfillment of the Requirements for the Degree of
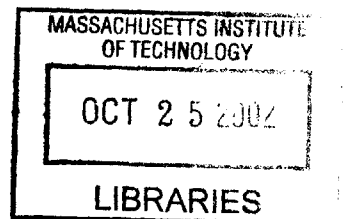
DOCTOR OF PHILOSOPHY IN MECHANICAL ENGINEERING

at the

MASSACHUSETTS INSTITUTE OF TECHNOLOGY

February 2002

Signature of Author:_____
Department of Mechanical Engineering
February 2002

Certified by:_____
Jung-Hoon Chun
Professor of Mechanical Engineering
Chairman, Doctoral Thesis Committee

Accepted by:_____
Ain A. Sonin
Professor of Mechanical Engineering
Chairman, Department Graduate Committee

The Effects of Deposit Thermal History on Microstructure

Produced by Uniform Droplet Spray Forming

by

Jean-Pei Jeanie Cherng

ABSTRACT

Uniform droplet spray forming is a process aimed at producing near-net-shape parts directly from the liquid melt by spraying micron-sized droplets onto a movable target. In spray forming, the solidification rate of the deposited material is a key parameter that influences its microstructure formation and consequently, its mechanical properties. Ideal deposit microstructure has fine grain size and minimal segregation.

The purpose of this thesis is to quantify the effects of deposit thermal history on the microstructure produced by the UDS forming process. Experiments were conducted with Zn-20wt% Sn alloy droplets using different process parameters to vary the deposit solidification rate from 6°C/s to 27°C/s immediately after deposition. The temperature of the sprayed deposits was measured *in situ* with a fiber-optic infrared thermometer and a contact thermocouple. Furthermore, a 2-D axisymmetric finite element model was developed to predict the temperature of the deposit during and after deposition. The simulation results show that radial heat conduction cannot be neglected when the thermal diffusivity of the substrate material is comparable to the diffusivity of the deposit material. Simulation results showed good agreement with the measured temperature data.

The resultant deposit microstructures were examined with scanning electron microscopy, which revealed that the deposit microstructure includes a mixture of solidified phases formed inside the droplets before impact. The characteristic cell size of the microstructure was shown to vary inversely with the square root of the deposit solidification rate. This implies that the growth of the microstructure is interface-controlled rather than diffusion-controlled, due to the high volume fraction of solid during deposition. Furthermore, the homogeneity of the deposit microstructure across its thickness suggests that the rapid solidification rate of the individual droplet layers upon impact played a minor role in determining the final deposit microstructure.

In conclusion, this research has developed a new methodology for studying the evolution of deposit microstructure in uniform droplet spray forming. The processing regime that promotes the layer-wise growth of deposits without porosity or liquid overflow has produced fine-scale deposit microstructure. The coarsening kinetics of the microstructure are interface-controlled by the deposit solidification rate. A uniform local solidification rate after deposition resulted in homogeneous deposit microstructure.

ACKNOWLEDGMENTS

3

TABLE OF CONTENTS

LIST OF FIGURES

7

8

LIST OF TABLES

9

Chapter 1. INTRODUCTION

1.1 Background

Spray forming produces near-net-shape products directly from the melt by spraying micron-sized droplets onto a stationary or movable substrate. Since its invention in the early-1970's, spray forming has been presented as an attractive alternative to conventional ingot metallurgy because spray formed products possess refined grain sizes, reduced phase segregation, and increased solubility of alloying elements [Singer and Evans 1983, Grant et al. 1991, Leatham and Lawley 1993]. As a result, the tensile strength, fatigue resistance, workability, and machinability of spray formed products are superior to those of cast products. Common applications of spray forming include the production of superplastic Al alloy sheets, cylindrical billets of Al alloys with high Si content, and Ni superalloy rings for automotive and aerospace components [Dai et al. 1998, Butzer and Bowen 1998, Srivastava et al. 2001]. Another application for spray forming is the rapid prototyping of injection molding dies by spraying tool steel onto patterned substrates [Amon et al. 1998, Hu et al. 2000, DeGaspari 2000].

Although much progress has been made to commercialize spray forming, process optimization is limited by the highly coupled process parameters used to control droplet generation. Conventional spray forming utilizes high-pressure gas jets to atomize a liquid metal stream into droplets that have a wide distribution of sizes. Typically, the mass-median droplet diameter in a gas-atomized spray varies inversely with the ratio of the gas to metal flow rate. Consequently, the size distribution and velocities of the droplets in the spray cannot be independently controlled, and their relationship can only be empirically correlated to the process parameters [Doherty et al. 1997, Zhou et al. 1997]. Since these values also determine the heat flux of the spray, systematic studies to reduce defect formation, such as porosity and grain size inhomogeneity, are often tedious or difficult to conduct.

The uniform droplet spray (UDS) process was developed at MIT to overcome the shortcomings of conventional spray forming [Chun and Passow 1993]. The UDS process produces a spray of metal droplets that are uniform in size. Based on Rayleigh's laminar jet instability principle, the droplet size and velocity, and hence, the heat flux of the spray can be precisely controlled in the UDS process. The process has been successfully applied to spray uniform droplets of Sn alloys, Zn alloys, Al alloys, and Cu alloys with diameters ranging from 75 μm to 800 μm. However, uniform droplet generation is only the first step in producing near net shapes.

10

1.2   Uniform Droplet Spray Forming

A schematic of the basic UDS apparatus is shown in Figure 1.1. The charge material is melted inside a crucible in an inert atmosphere. By pressurizing the crucible with inert gas, a laminar jet of liquid metal is ejected through an orifice mounted in the center of the crucible bottom. The jet is broken into a stream of uniform droplets by imposing sinusoidal vibrations inside the melt with a stack of piezoelectric transducers, which is connected to a rod immersed in the melt. As the droplets break from the jet, they pass through a charging plate. The capacitance between the plate and jet electrically charges the droplets to the same polarity to prevent them from merging into each other. The electrical repulsion of the charged droplets creates a diverging spray whose diameter depends on the amount of applied voltage. The spray is deposited onto a temperature- and motion-controlled substrate where the droplets consolidate to form a deposit with desired microstructure and geometry.

Deposit microstructure and geometry are the final outputs of the UDS forming process. Figure 1.2 illustrates the general process-parameter relationships. The process output depends on three key design parameters: the thermal state of the incoming droplets, the distribution of mass flux deposited on the substrate, and the thermal state of the growing deposit. Thermal state is defined here as the temperature and volume fraction of solid at a given location and time in the spray forming process.   Unlike conventional spray forming, the design parameters can be independently controlled by the process parameters in the UDS process. This feature simplifies process control and allows for greater range of processing conditions and attainable microstructures. Therefore, two stages of process modeling and understanding are necessary to optimize the final output. First, a model to predict the values of the key design parameters given the operating process parameters is necessary.   Then, a model to predict the deposit microstructure and geometry based on the key design parameters is needed.

1.3   Thesis Motivation

The uniform droplet size greatly facilitates the prediction of key design parameters, since each droplet in the spray is considered to have the same velocity and thermal state. However, there are fewer tools available to model the complexity of deposit microstructure formation. The motivation behind this thesis is to advance the understanding of deposit microstructure formation in uniform droplet spray forming. The deposit microstructure is critical since it dictates the mechanical properties of the sprayed material. Although refined microstructure has been demonstrated with conventional spray forming, the process yield is significantly reduced by defects such as porosity and grain size inhomogeneity [Mingard et al. 1998, Xu and Lavernia 1999, Hu et al. 2000, Brinksmeier and Schunemann 2001]. Furthermore, process optimization

11

has been constrained by highly coupled process parameters and empirical process models. Ideally, the UDS process with its unique process control capability can be developed to produce refined microstructure without defects for applications such as rapid prototyping.

1.4 Prior Work

Microstructure evolution begins with the cooling of the droplets during flight and is completed after the consolidated deposit is fully solidified. Prior work by Chen [1996] established a numerical model to predict the thermal state of binary alloy droplets during flight. Since the velocity of the droplet affects its cooling rate, the droplet thermal model incorporates a droplet flight trajectory model developed by Passow [1992]. The droplet thermal model assumes that the droplets experience Newtonian cooling and that solute redistribution during solidification is governed by the Scheil equation. Chen verified the droplet thermal model by measuring the solid fraction of Zn-20wt% Sn alloy droplets at different flight distances. The experimental results showed excellent agreement with the predicted values.

By utilizing the droplet thermal model, Chen showed that the thermal state of the droplets prior to impact affects the morphology of the deposit microstructure. Chen produced a fine-equiaxed microstructure in Sn-5wt% Pb alloy deposits by spraying droplets with 30% volume fraction solid onto a copper substrate at an initial temperature of 173°C. Furthermore, he showed that spraying fully liquid or superheated droplets onto the substrate at the same temperature did not produce equiaxed grains, but rather an epitaxial columnar microstructure. Therefore, he concluded that the absence of pre-solidified phases in the liquid droplets prevented equiaxed grain growth in the deposit. His conclusion concurs with that of other spray forming investigators who have proposed that the equiaxed grain structure observed in spray formed material is the result of a high density of potent nuclei delivered to the deposit [Grant et al. 1991, Liang and Lavernia 1994].

Assuming that partially solid droplets are sprayed onto the deposit, it is important to understand what controls the degree of microstructural refinement that occurs during and after deposition. Isothermal annealing studies of conventionally spray formed materials have been conducted to simulate the microstructure development after deposition [Annavarapu and Doherty 1995, Underhill et al. 1995, Manson-Whitton et al. 1998]. These studies have shown that grain coarsening within the reheated material increases with the annealing time and temperature in the solid-plus-liquid regime, while showing negligible coarsening in the fully solid regime. Therefore, the solidification rate or time and the thermal state of the deposit material during solidification are believed to control the extent of grain growth after deposition. For example, variations within a spray formed microstructure have been attributed to non-uniform thermal conditions experienced at different locations in the deposit [Liang and Lavernia 1994, Mingard

et al. 1998, Xu and Lavernia 1999].

To control the deposit thermal state during solidification, Acquaviva [1995] made the first attempt to model and measure the deposit thermal history in the UDS forming process. The temperature of a Sn-15wt% Pb deposit was measured at several locations by placing thermocouples onto the deposit surface as the spray was turned on and off several times. However, the one-dimensional finite difference model that was employed to predict the deposit thermal history greatly overestimated the measured temperatures. Acquaviva attributed the discrepancy between the measured and calculated thermal histories to neglecting transverse heat conduction in his model. In addition, Acquaviva observed that the microstructure of the sprayed Sn-15wt% Pb deposit exhibited coarser grains at the top of the deposit than at the bottom. He suggested that the temperature gradient across the deposit, about 0.5°C/mm, which corresponded to a 45% variation in liquid fraction during solidification led to the formation of inhomogeneous microstructure

1.5 Thesis Objectives

Acquaviva demonstrated that the deposit thermal history plays a significant role in the formation of deposit microstructure in uniform droplet spray forming. However, a systematic study of its effects has yet to be conducted. Therefore, the objective of this thesis is to examine the effects of the deposit thermal history during solidification on the refinement, homogeneity, and phase segregation in the final deposit microstructure. The scope of this investigation does not include the effects of deposit thermal state on porosity formation.

This thesis describes a series of deposition experiments conducted with Zn-20wt% Sn alloy droplets using different process parameters to vary the deposit thermal history. The thermal histories of the deposits are measured with a fiber-optic infrared thermometer and thermocouple. Furthermore, a 1-D and a 2-D axisymmetric finite element model are developed to predict the deposit thermal history. The deposit thermal model is applied to the experimental conditions and the results are compared to the temperature data acquired during the deposition experiments. Finally, the deposit microstructures are examined to quantify the effects of the deposit thermal history.

13
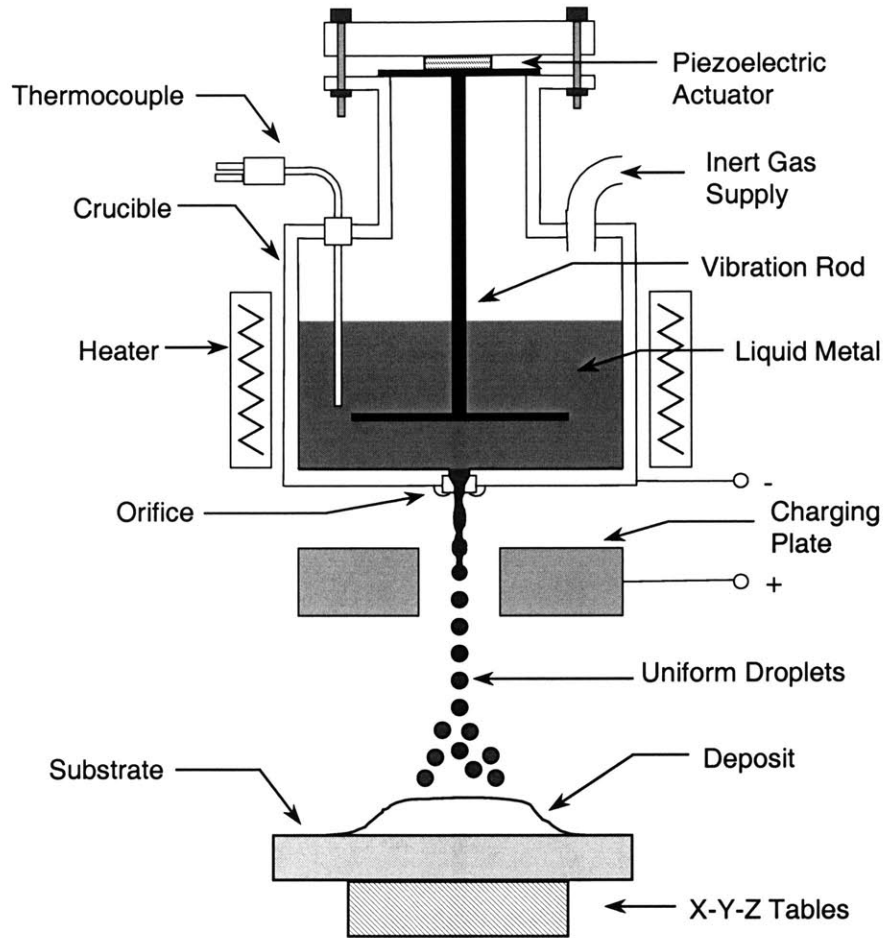
Figure 1.1. Schematic of the uniform droplet spray apparatus.
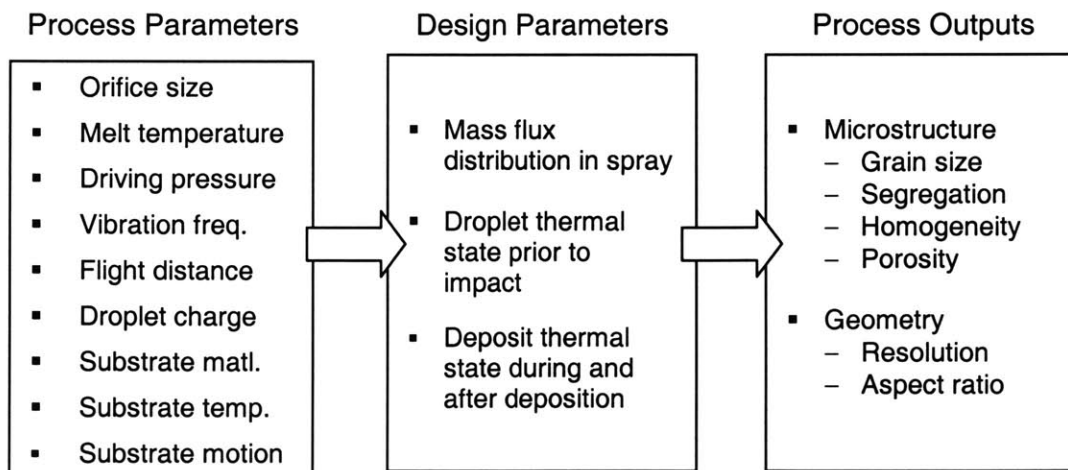
Figure 1.2. Process-parameter relationships in UDS forming.

14

Chapter 2. DEPOSITION EXPERIMENTS

2.1 Introduction

The purpose of the experimental study is two-fold. The first part is to develop a technique to measure the temperature of the deposit during the UDS forming process. The second part is to produce deposits with different thermal histories in order to examine how the deposit thermal history affects its microstructure. In this chapter, the experimental apparatus and the temperature measurement of the deposits sprayed with varying process parameters are discussed, while the resulting deposit microstructures are addressed later in Chapter 4.

2.2 Experimental Apparatus

A schematic of the experimental apparatus used in this study is shown in Figure 2.1. The apparatus consists of several major components, namely the uniform droplet spray generator and its instrument panel, the spray chamber, the substrate and its motion control system, and the deposit temperature sensors with the data acquisition system.

The basic UDS generator as described in Chapter 1 consists of a crucible with a bottom orifice, a heater and thermocouple, a vibration rod connected to a stack of piezoelectric transducers, and a droplet charging plate. In this study, a stainless steel crucible, which can hold about 180 cm^3 of melt, is used and internally coated with a boron-nitride paint to prevent reaction with the melt. The crucible heater is a 500 W resistance band heater and the melt temperature is controlled by a type-K thermocouple sheathed in a ceramic tube. The crucible nozzle is a laser-drilled sapphire orifice and secured with high-temperature ceramic adhesive. The vibration rod is a 6.3-mm diameter, aluminum oxide rod to insulate the piezoelectric transducers from heat. The piezoelectric transducers are 12.7-mm diameter and 2.5-mm thick disks sandwiched between brass electrodes. The droplet charging plate is located about 4 mm below the crucible orifice and has an 8-mm wide and 12-mm tall channel through which the droplet stream passes.

The spray generator is mounted to the glass tee-section above the spray chamber. The generator is connected to an instrument panel that regulates the gas supply, controls the crucible and substrate temperatures, and generates the voltage signals to the piezoelectric transducers and charging plate. Detailed information about the spray generator can be found elsewhere [Passow 1992]. The glass tee-section allows the stream break-up to be monitored with a CCD camera and

digital stroboscope. The flash rate of the stroboscope is synchronized with the jet break-up frequency, which causes the stream of uniform droplets to appear frozen on the monitor screen. During experiments, a ceramic waste cup is manipulated through the tee-section to start and stop deposition.

Because oxidation of the liquid metal will prevent uniform jet break-up, the UDS process takes place within a spray chamber that is evacuated and filled with nitrogen forming gas (95%N_2-5%H_2). The main body of the aluminum spray chamber is 1 m in diameter and 1 m in length. It houses three linear motion tables to move the substrate in x-, y-, and z-directions. Individual stepper motors, an amplifier, and a PC controller board with a programmable user interface drive the motion tables. Five flanged portholes are provided on the spray chamber for glass view ports and electrical feed-through connections.

At the base of the substrate is a 100 mm x 200 mm x 25 mm copper block that is imbedded with four 100 W cartridge heaters. The copper block is thermally insulated on its sides and bottom to prevent heat loss and to protect the motion tables. A titanium plate, 100 mm x 200 mm x 12 mm, is fastened on top of the copper heating block to act as the semi-infinite substrate material. Two thermocouples (3.2 mm in diameter) are inserted through the copper block to measure the top and bottom surface temperatures of the titanium plate. Power to the heaters in the copper block is regulated in order to maintain a constant temperature at the bottom surface of the titanium plate. In addition, plates with different thermal conductivity, such as glass and aluminum plates, were placed on top of the titanium plate to change the thermal history of the deposit.

2.3   Material Selection and Preparation

The spray material used in all of the experiments is a Zn-20wt% Sn alloy, whose equilibrium phase diagram is shown in Appendix A. This simple two-phase binary alloy allows for better microstructural characterization. The very limited solid solubility of Sn in the first solidified Zn phase leads to clearly defined dendritic or cellular boundaries. Furthermore, previous research by Chen [1996] was successful in developing a numerical model to predict the thermal state of Zn-20wt% Sn droplets during flight. Information on the droplet thermal state during flight is required to predict and control the subsequent deposit thermal history.

The Zn-20wt% Sn alloy is prepared by melting proportional masses of 99.99% pure Zn and 99.99% pure Sn in air in a stainless steel crucible coated with boron nitride. The molten alloy is stirred while it cools to ensure a uniform distribution of the Sn solute. The oxide layer on the surface of the solidified ingot is machined off, and then the ingot is cut into smaller pieces to fit inside the spray generator. The pieces are deburred and cleaned with methanol. Compared to

the coarse dendritic structure of a typical cast Zn-15wt% Sn alloy, Figure 2.2 shows that the microstructure of the as-prepared alloy is well mixed. Using wavelength dispersive spectroscopy, the dark dendritic phase is measured to be more than 99wt% Zn, while the light matrix is on average 96wt% Sn. Thus, by measuring the area fraction of the Sn-rich phase, the average composition of the bulk material is determined to be 20.6wt% Sn.

Different substrate materials are used in these experiments to vary the cooling rate of the deposit. To decrease the deposit cooling rate, a soda-lime glass plate, 100 mm x 100 mm x 2.3 mm, is pasted on top of the titanium substrate with highly conductive, silicone thermal paste (Omegatherm 201). To increase the deposit cooling rate, a commercially pure aluminum plate, 75 mm x 50 mm x 1.5 mm, is pasted on top of the titanium substrate. The thermal properties of the substrate materials are given in Table 2.1.

2.4 Sensors and Data Acquisition

The temperature of the deposit is measured *in situ* with two sensors that would least interfere with the spray deposition process. First, a non-contact, infrared thermometer, called the Accufiber Model 10 by Luxtron Corporation (Santa Clara, CA) is used to measure the temperature of the deposit surface. Second, a type-K thermocouple, sheathed in 0.5-mm diameter stainless steel, is fastened on top of the substrate surface to measure the temperature of the bottom surface of the sprayed deposit. Figure 2.3 shows the location of both sensors with respect to a deposit sprayed onto the substrate.

The Accufiber system uses an optical pyrometer to detect the radiant power emitted from the deposit surface and transmits it through a fiber optic cable to an InGaAs photo-detector inside the electronic controller unit. The photo-detector converts the optical signal within a 0.8-μm to 1.7-μm wavelength band into an electrical signal that is proportional to temperature. The Accufiber system is one of the few commercially available, fiber-optic infrared thermometers that can measure the temperature of low emissive surfaces below 200°C.

The Accufiber system has a sampling rate of 10 samples/second, 0.01°C resolution, and 2°C accuracy. In addition to the alphanumeric display of temperature, the controller also provides an analog voltage signal from 0-10V that linearly corresponds to its temperature range from 100°C to 1000°C. The output voltage signal is filtered by the controller with a cutoff frequency of 2 kHz and recorded by a data acquisition (DAQ) system into a spreadsheet file. The DAQ system by National Instruments (Austin, TX) consists of a shielded connector board (USB-100), a high-speed, 16-bit, DAQ computer board (PCI-6071E), and DAQ software called Labview version 5.1. The DAQ system acquires voltage data from the Accufiber sensor at 50 samples/second.

As shown in Figure 2.3, the Accufiber pyrometer is mounted above the substrate at a 55° angle from the horizontal plane, approximately 120 mm away, to avoid the spray. This renders a slightly elliptical measurement spot, about 4 mm in diameter, on the substrate. Shining a bright light through the end of the fiber optic cable illuminates the measurement spot of the pyrometer. Since the fiber optic cable should not be exposed to temperatures above 100°C, the pyrometer fixture is insulated from the substrate. The fiber optic transmission cable, 5 m in length, connects the pyrometer inside the spray chamber to the controller outside the spray chamber.

Figure 2.3 also shows the deposit thermocouple. The thermocouple is positioned on the substrate surface such that its tip is located on the right edge of the illuminated pyrometer spot. The alignment of the thermocouple compensates for the shift in the pyrometer spot as the deposit grows during deposition. After deposition, the thermocouple measures the temperature of the bottom surface of the deposit directly below the pyrometer spot. The DAQ system acquires the thermocouple signal at 50 samples/second after it filters noise above 5 hz with a digital low-pass filter.

2.4.1 Sensor calibration

The Accufiber sensor measures the infrared radiation emitted from the deposit surface and converts this power to temperature according to Planck's equation. Because the deposit surface does not behave as an ideal blackbody, its emissivity needs to be determined for accurate temperature conversion. Furthermore, because the Zn-20wt% Sn deposit surface is reflective, the pyrometer is susceptible to detecting background radiation [Gougeon and Moreau 1993]. To minimize the background radiation during data acquisition, the chamber view ports are covered and an aluminum shield is placed at the bottom of the glass tee-section. The shield is black-anodized on the downward surface and has a center hole (25 mm in diameter) that allows the spray to pass through, while blocking most of the radiant heat from the droplet generator from reaching the reflective deposit surface. After deposition, the ceramic waste cup is rotated to cover the center hole and eliminate background radiation completely.

Unfortunately, during deposition, the pyrometer is exposed to background radiation as well as incoming droplets that intersect with the optical path of the pyrometer. It is difficult to predict or measure how the droplets of the incoming spray will affect the pyrometer measurement. The droplets might reflect radiation emitted by the deposit surface or emit their own radiation, causing the pyrometer to overestimate the surface temperature of the growing deposit.

Before data acquisition, the Accufiber sensor requires the emissivity information of the target surface, so that the sensor can convert the radiant power measured by the photo-detector into temperature. The emissivity of a real surface changes with temperature and wavelength, but it can also be affected by various parameters such as surface roughness and oxidation. Most non-

18

oxidized metals have low emissivity, which limits the minimum temperature that can be detected by the photo-detector before significant signal-to-noise error. The minimum sensing temperature is also limited by the maximum wavelength of the photo-detector. A dual-wavelength or two-color pyrometer that does not require surface emissivity to be known was not commercially available for the temperature range of this application.

For the Accufiber sensor, the emissivity of the target surface can be expressed as a polynomial function of temperature. However, the sensor assumes that the target surface is a gray body, i.e., the surface emissivity is constant over the detected wavelength spectrum from 0.8 μm to 1.7 μm. To determine how the emissivity of a typical Zn-Sn deposit changes with temperature, a thermocouple (0.5 mm in diameter) was bonded to the surface of a previously sprayed deposit with silver epoxy (Epotech). The deposit was heated on the titanium substrate inside the spray chamber to temperatures between 180°C and 350°C. The pyrometer was focused on the deposit surface and the input value for emissivity was adjusted until the sensor output matched that of the thermocouple.

A plot of the calibration data of emissivity versus temperature for a typical Zn-Sn deposit surface is shown in Figure 2.4. The figure shows that emissivity slightly increased with temperature. However, upon closer examination of the deposit surface, the surface appeared to have oxidized during the lengthy heating cycle of the calibration experiment. Thus, the measured increase in emissivity may have been due to either temperature or surface oxidation. However, since the variation in emissivity over the measured temperature range is small, it was fixed at its average value of 0.15. As a result, the sensor measurement has at most ±3°C error due to emissivity variation, in addition to its instrument error of 2°C.

To test the emissivity calibration, a preliminary experiment was conducted in which the temperature of the deposit surface was measured *in situ* with the Accufiber sensor during and after deposition. The emissivity input value was set at 0.15. The temperature output of the Accufiber sensor is shown in Figure 2.5. The transient curve shows how the surface temperature of the deposit increased during deposition. After deposition, the deposit temperature decreased until it reaches a plateau, at which the temperature remained constant for about 10 seconds before it continued to decrease. This temperature plateau should correspond to the eutectic temperature of the Zn-20wt% Sn alloy at 198.5°C. However, the sensor output was about 9°C lower, which implies that the calibrated emissivity value was higher than that of the actual value.

Most likely, the steady-state temperature measurements performed on a previously sprayed deposit cannot accurately predict the emissivity value of every deposit surface because of unique variations in surface roughness and oxidation from deposit to deposit. However, the steady-state temperature measurements do reveal that the deposit surface emissivity does not change significantly from 180°C to 350°C. Therefore, it is necessary to determine the surface emissivity

uniquely and adjust the temperature output of the Accufiber sensor after the data is acquired.

2.4.2 Post-processing of the sensor output

Due to segregation, each Zn-20wt% Sn deposit undergoes eutectic solidification as it cools on the substrate. Therefore, it is convenient to use the temperature plateau in the sensor output to adjust the data after it has been acquired. The emissivity value should be changed so that the temperature plateau occurs at the eutectic temperature. Based on Planck's relationship, the emissivity value affects the way in which the total emissive power measured from the deposit surface is converted into temperature.

According to Planck's relation, the spectral emissive power E (W/m$^2 \cdot \mu$m), emitted by a diffuse surface at a given wavelength λ (μm), temperature T (K), and emissivity ε_λ, is given by:

$$E(\lambda,T) = \frac{\varepsilon_\lambda C_1}{\lambda^5 [\exp(C_2/\lambda T) - 1]}$$ (2.1)

where the first and second radiation constants are C_1=3.742x10^8 W$\cdot\mu$m^4/m^2 and C_2=1.439x10^4 μm$\cdot$K, respectively [Lienhard and Lienhard 2001]. Since the Accufiber sensor uses an InGaAs detector that detects radiation from 0.8 μm to 1.7 μm, it is necessary to integrate the emissive power across the wavelength range to calculate the total emissive power. However, this sensor has been shown to behave as an effective single wavelength detector [Hu 2001]. If the effective wavelength is known, then Eq. 2.1 can be used to determine the true emissivity of the deposit surface and to adjust the sensor temperature data accordingly.

To find the effective wavelength, calibration experiments were performed with a previously sprayed Zn-20wt% Sn deposit. The deposit was heated on the titanium substrate inside the spray chamber and maintained at a surface temperature of 175°C. The pyrometer was focused on the deposit surface and the input value for emissivity was adjusted incrementally from 0.095 to 0.6. The temperature output of the Accufiber sensor was recorded at each emissivity level. Figure 2.6 shows how the temperature output changed with respect to the emissivity input value. Because the deposit surface temperature was actually constant, the radiant power detected by the Accufiber sensor should also be constant at the effective wavelength. Using Eq. 2.1 and the temperature-emissivity data in Fig. 2.6, the spectral radiant power was calculated for wavelengths between 0.8 μm and 1.7 μm. It was found that when λ=1.59 μm, the variation in radiant power was minimized to less than 0.5%. Therefore, the single effective wavelength, λ_{eff}, of the Accufiber sensor was determined to be 1.59 μm.

By substituting λ_{eff} into Eq. 2.1, the temperature output of the Accufiber sensor acquired for each experiment can be adjusted, if necessary. For example, the temperature curve of the preliminary

20

experiment shown in Fig. 2.5 has the plateau temperature at 190°C, because the emissivity value was set at 0.15. The true emissivity of the deposit surface can be calculated by taking a ratio of emissive powers:

$$\ln\left[\frac{\varepsilon_t}{\varepsilon_f}\right] = \frac{C_2}{\lambda_{eff}} \cdot \left[\frac{1}{T_t} - \frac{1}{T_f}\right]$$

(2.2)

where ε_f and ε_t are the false and true emissivity values, respectively. T_f and T_t are the corresponding false and true temperatures, respectively [Zentner et al. 1994]. After the true emissivity value is determined at the eutectic temperature, it can be applied to recalculate the entire temperature output of the Accufiber sensor. Figure 2.7 shows how the temperature curve from Fig. 2.5 shifts upward such that the plateau occurs at the eutectic temperature. In this example, the emissivity value was corrected from 0.15 to 0.10.

Given the effective wavelength of the detector, Eq. 2.1 can also be used to determine the temperature error due to an uncertainty in the emissivity value. Taking the derivative of temperature in Eq. 2.1 with respect to emissivity gives:

$$\frac{\partial T}{\partial \varepsilon} = -\frac{T^2 \lambda_{eff}}{C_2 \varepsilon}$$

(2.3)

For example, at 200°C, a 20% increase in emissivity correlates to a 4.9°C error in temperature.

2.5   Experimental Parameters and Procedure

The following experiments were designed to produce deposits with different thermal histories by varying the process parameters. For a certain deposition time, the thermal history of the deposit depends on the rate of heat input of the droplet spray and the rate of heat extraction through the substrate and to the surrounding gas. The rate of heat input is determined by the thermal state of the incoming droplets and the mass flux of the spray. These design parameters are controlled by the process parameters used to generate the spray, such as the vibration frequency and droplet-charging voltage, as described in Fig. 1.2. The droplet thermal model discussed in Chapter 1 is used to predict the droplet thermal state and the average mass flux from the spray parameters. With a stationary substrate, the rate of heat extraction depends on the substrate material and substrate temperature.

The different combinations of the process parameters are limited by two factors. First, the balance between the rates of heat input and heat extraction should prevent porosity formation in

21

the deposit. Furthermore, the process parameters should encourage the deposit to grow in a layer-wise upward manner, rather than as a burgeoning liquid pool. These conditions not only improve the deposit microstructure, but also facilitate modeling of the deposit thermal history, as discussed in the next chapter. Prior to the model development, the process parameters for optimal deposition were determined empirically. Table 2.2 lists the eleven experiments, labeled A through K, that were conducted with different combinations of process parameters to produce deposits with different thermal histories.

In these experiments, the rate of heat input was varied by decreasing the droplet temperature at impact from 377.4°C to 373.3°C, which corresponds to a decrease in droplet solid fraction from 91.7% to 75.6%. The average mass flux of the spray was also varied from 1.2 $g/s \cdot mm^2$ to 2.4 $g/s \cdot mm^2$. Mass flux is defined as the amount of mass per unit time per unit area delivered to the deposit. Due to the electrical repulsion among the droplets, the mass flux of the spray is not uniform over the deposit area. Rather, the mass flux tends to be concentrated in a concentric ring around the center of the deposit, as shown in Figure 2.8. However, for the purpose of characterizing the rate of heat input, an average mass flux is used.

The rate of heat extraction was changed by spraying onto different substrate materials at different initial temperatures. The heater controller maintained the titanium substrate at either 125°C or 175°C. When a glass plate or aluminum plate was pasted above the titanium substrate, the initial steady-state temperature of the plate surface was measured by the deposit thermocouple before deposition. For the glass plate, its surface temperature was at 120°C and 160°C, when the titanium substrate was at 125°C and 175°C, respectively. The temperature of the aluminum plate was 170°C. The substrate temperature cannot exceed the solidus temperature of the Zn-20wt% Sn alloy, which is 198.5°C. The standard operating procedure used in these experiments is described below.

The experimental procedure begins by loading the droplet generator with 300 g of prepared Zn-20wt% Sn alloy. After the generator is assembled, it is fastened to the top flange of the spray chamber. The substrate surface is cleaned with methanol. If the substrate requires a glass or aluminum plate, then the plate is pasted on top of the titanium substrate with a thin layer of the conductive silicone paste. By illuminating the target spot, the plate is centered with respect to the measurement or target spot of the pyrometer. The thermocouple is positioned on the substrate surface such that its tip is located on the right edge of the spot. A grid is marked on the substrate to aid positioning the substrate under the spray.

The spray chamber is vacuumed below 200 mTorr and refilled with nitrogen forming gas. This sequence is repeated three times. On the third refill, the inert gas fills the chamber to 7-kPa gage pressure. The oxygen concentration of the chamber is measured by flowing sample gas through an oxygen sensor. If the partial pressure of oxygen is more than 20 ppm, the chamber should be

22

vacuumed and refilled again. Afterwards, the heater controllers for the crucible and substrate are turned on. The Accufiber controller unit is also turned on and an emissivity value of 0.1 is entered. Using the motion control system, the substrate is moved to a "test position" such that the target spot of the pyrometer is not beneath the droplet spray. The test position is used to determine the trajectory and location of the droplet spray.

After the melt temperature and substrate temperature have stabilized at their setpoint values, the crucible is pressurized and a uniform droplet spray is generated. The spray is deposited onto the substrate at the test position for 10 s. The ceramic waste cup is used to stop and start deposition. Using the location of the test deposit as a reference, the target spot of the pyrometer is positioned directly below the spray generator. The chamber view port is covered and the data acquisition software begins to acquire the temperature data from the Accufiber sensor and the thermocouple. Finally, the spray is deposited onto the substrate at the target spot for 10 s. The spray duration is limited to 10 s, so that the resulting growth in deposit height does not significantly change the thermal state of the droplets at impact during deposition. Figure 2.9 shows the change in droplet thermal state during flight under typical process parameters predicted by the droplet thermal model. Data acquisition continues for about 200 s after deposition.

After data acquisition, the substrate and crucible heaters are turned off and allowed to cool. The spray chamber is opened, and the measurement spot of the pyrometer is illuminated and marked on the sprayed deposit. The spray deposit is removed from the substrate and weighed with ±0.1g uncertainty. The weight of the deposit divided by the spray duration gives the mass flow rate of the experiment. The bottom surface of the deposit is scanned into a digital file from which image analysis software (Scion Image v.4) is used to measure the deposit area with ±5mm^2 uncertainty. The average mass flux of the experiment is calculated by dividing the mass flow rate by the surface area of the deposit bottom.

2.6   Results

Using the experimental procedure described above and the parameters listed in Table 2.2, the temperature histories of eleven deposits were recorded. When necessary, the temperature output of the Accufiber sensor was adjusted by finding the emissivity value of the deposit surface at the eutectic temperature. The emissivity value used for post-processing the data of each deposition experiment is also listed in Table 2.2.

2.6.1   Deposition experiments on glass substrates

In Experiments A, B, C, and D, the sprays were collected on glass plates whose initial surface temperature was 160°C. The deposit temperature curves measured by the pyrometer and

thermocouple in these experiments are shown in Figure 2.10. Experiments B, C and D were designed to test the individual effect of decreasing droplet temperature on the deposit thermal history. However, the combination of process parameters in Experiment D produced a deposit with large-scale porosity. Therefore, droplet temperature was not reduced below 373.3°C, which corresponds to a 75% liquid fraction.

In Experiments E, F, and G, the deposits were sprayed with decreasing rates of heat input onto glass plates whose initial temperature was 120°C. The deposit temperature curves are shown in Figure 2.11. Experiments F and G show the individual effect of decreasing mass flux on the deposit thermal history. In addition, the effect of changing substrate temperature is shown by comparing Experiments A and E, in which the deposits were sprayed with about the same heat flux but onto glass substrates at different temperatures.

2.6.2 Deposition experiments on metal substrates

Figure 2.12 shows the temperature curves recorded during Experiments H, J, K, and I. In Experiments H and I, the deposits were sprayed onto the titanium substrate at 175°C with decreasing heat flux. However, in these experiments, the data from the thermocouple was obscured by noise due to poor grounding of the thermocouple to dissipate the electric charge of the spray. Therefore, Figure 2.12 only shows the pyrometer curves from Experiments H and I. The titanium substrate with an initial temperature of 125°C was used in Experiment K and an aluminum plate initially at 170°C was used in Experiment J. Comparing Experiments K and F shows the effect of changing substrate material on deposit thermal history.

2.7 Discussion

As depicted in Fig. 2.5 and revealed in all the experimental results, the deposits undergo four different thermal stages: heating during deposition, segregated solidification, eutectic solidification, and solid-phase cooling. By comparing the pyrometer temperature curve with the thermocouple curve, information about the thermal gradient across the thickness of the deposit is obtained. Furthermore, the accuracy of the pyrometer measurement, which is more vulnerable to error, can be evaluated. The effects of changing the process parameters on the deposit thermal history are observed by comparing the deposit thermal histories.

2.7.1 Deposit thermal history

At the start of deposition, the measured temperature curves quickly rise above the eutectic temperature and increase steadily during deposition. The droplets, which prior to impact have 8% to 24% solid fraction, lose a significant amount of their latent heat upon impact with the

24

substrate and growing deposit. However, continuous deposition reheats the partially solidified splats. During this stage, the growing deposits are entirely in a mushy state ranging from about 63% to 77% solid fraction, or from 351°C to 240°C, respectively. The droplets sprayed onto metal substrates lead to deposits with lower temperatures and faster cooling rates after deposition.

The temperature curves exhibit a temperature gradient between the top and bottom surfaces of the growing deposit. Although it is possible that the pyrometer measurement is inflated by background radiation, the temperature gradient is greater in deposits that were sprayed onto metal substrates than those sprayed onto glass (except for Experiments C and D). This implies that the heat extraction rate through metal substrates is indeed faster than glass. However, in either case, the rate of heat extraction is slower than the rate of heat input since the temperature of the deposit continuously increases during deposition. The temperature gradients shown in Experiments C and D are caused by large-scale porosity present in these deposits, since porosity decreases the conductivity of the deposit material. After deposition, the top and bottom surface temperatures quickly converge and fall to the eutectic temperature.

During eutectic solidification, the temperature of the deposit should stay constant while the remaining liquid in the deposit solidifies into a single eutectic phase. The temperature measurement by the thermocouple indicates that contact resistance exists between the thermocouple and the deposit since the measured value is a few degrees below the eutectic temperature. Contact resistance may be caused by an air pocket around the thermocouple tip. Nevertheless, the thermocouple is still sensitive to the deposit temperature, since data show that the duration of the eutectic solidification decreases with decreasing substrate temperature and increasing substrate diffusivity. For example, in Experiment K, the heat extraction rate of the cold titanium substrate is so fast that the eutectic temperature plateau is very short.

In some cases, it is noticeable that the temperature measured by the pyrometer does not remain constant during eutectic solidification. Specifically, in Experiments A, B, and F, the pyrometer temperature increases about 5°C during eutectic solidification. Since this behavior is not present in the thermocouple data, the temperature rise is most likely due to an increase in the deposit surface emissivity, rather than an actual increase in deposit temperature. The change in emissivity may be caused by oxidation on the deposit surface or by a change in surface roughness as the remaining liquid solidifies. If the pyrometer measurement does not remain constant during eutectic solidification, its temperature output is adjusted with a constant emissivity value such that the temperature of the deposit at the beginning of the eutectic region is equal to 198.5°C, as described in Sec. 2.4.2.

After solidification, the deposit cools to the steady-state temperature of the substrate heating block. Theoretically, the top surface temperature of the deposit should cool below the bottom

surface temperature due to convection and radiation. However, either an increase in the surface emissivity or the contact resistance between the thermocouple and the deposit causes the pyrometer curve to remain above the thermocouple curve in steady state.

In certain experiments, the temperature gap between the pyrometer and thermocouple curves increases over time. This is especially noticeable for experiments that have a steady-state temperature below 150°C, as shown in Figure 2.11. Although the pyrometer is quoted to have a temperature sensing range between 100°C and 1000°C, it is now believed that the temperature sensing range applies to ideal surfaces that behave as blackbodies. Using Eq. 2.2, it is possible to calculate the equivalent lower temperature limit for a surface that has an emissivity of 0.1. This lower limit is found to be 139°C, which explains why the pyrometer measurement reaches a false steady state in certain experiments.

2.7.2 Effect of process parameters on deposit thermal history

To compare the different thermal histories of the UDS deposits, it is useful to develop some metrics that describe the deposit thermal state as well as its rate of change. In Chapter 4, these metrics will be used to establish correlations between the deposit thermal history and the resultant deposit microstructure. Furthermore, since the deposits do not begin to solidify until after deposition, the extent of microstructure growth and coarsening is most likely controlled by the deposit thermal state after deposition. Thus, the following three metrics are developed: the solid fraction in the deposit just prior to solidification, the solidification rate of the deposit immediately after deposition, and the solidification time required for the deposit to reach the eutectic temperature after deposition.

Figure 2.13 shows all the cooling curves measured by the pyrometer during segregated solidification for all the deposition experiments. From these curves, the values of the metrics are determined and tabulated in Table 2.3. The deposit solid fractions just prior to solidification are measured to range from 63% to 75%. The initial solidification rate of the deposit is calculated by fitting a 3rd-order polynomial curve to the cooling curve data and taking the average of its derivative during the first two seconds after deposition. Thus, the solidification rates of the deposits immediately after deposition range from 6°C/s to 27°C/s. The deposit solidification times are measured to range from 9 s to 45 s.

Utilizing the unique process flexibility of the UDS process, four independent parameters were used in this experimental series to vary the deposit thermal history: droplet thermal state, spray mass flux, substrate temperature, and the thermal diffusivity of the substrate material. By comparing the cooling curves in Fig. 2.13, the role of each parameter in influencing the deposit thermal history is evaluated. For example, there is a noticeable gap between cooling curves of the deposits on glass substrates (A through G) and those of deposits on metal substrates (H

through K). The separation shows that substrate material, and hence its thermal diffusivity, has a greater effect than either the substrate temperature or the spray conditions in controlling the deposit thermal history. The deposits sprayed onto metal substrates have lower peak temperatures and faster cooling rates than any of the deposits sprayed onto glass substrates.

There is another gap between the cooling curves of Experiments A through D and E through G, in which the deposits were all sprayed onto glass. This gap suggests that the substrate temperature plays a stronger role than the spray conditions in determining the cooling rate of the deposit. For example, according to Table 2.2, the mass flux of the spray was decreased by about 25% from Experiment F to Experiment G. As a result, Table 2.3 shows an increase of about 1% in the deposit solidification rate. However, when the substrate temperature was decreased by about 25% from Experiment A to Experiment E, there was a 200% increase in deposit cooling rate.

2.8 Conclusions

This chapter has described the deposition experiments conducted with Zn-20wt% Sn alloy and aimed at producing deposits with different thermal histories. A new method of measuring the deposit thermal history during the UDS forming process has also been described and evaluated. In general, the data show strong correlation between the temperature curves measured by the infrared pyrometer and contact thermocouple, especially after deposition during the solidification stage. Fortunately, this area is where our main focus lies in determining the effects of deposit thermal history on the resultant microstructure. Although some uncertainty exists in the pyrometer measurement due to variations in surface emissivity, it should not be significant when the data is used in a relative manner for comparison. For example, by comparing the different deposit thermal histories, the data reveal that the substrate temperature and thermal diffusivity play a significantly greater role in determining the deposit thermal history than the spray conditions. In the next chapter, a finite element model of the deposition process is developed to predict and quantify the effects of process parameters on the deposit thermal history.

27
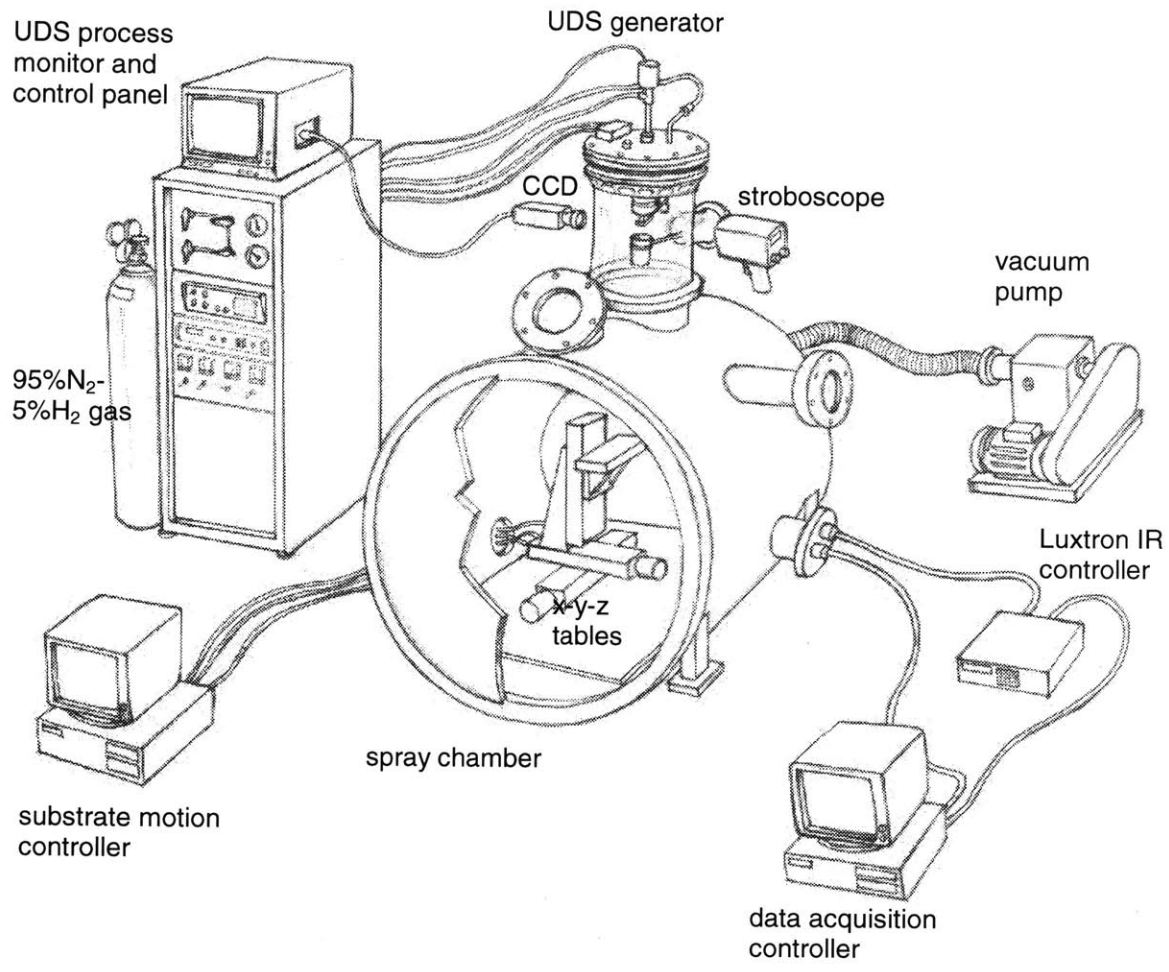
Figure 2.1. Schematic of the experimental apparatus used to produce and control spray deposition. (*Drawing courtesy of W. Hsiao, 2001*)
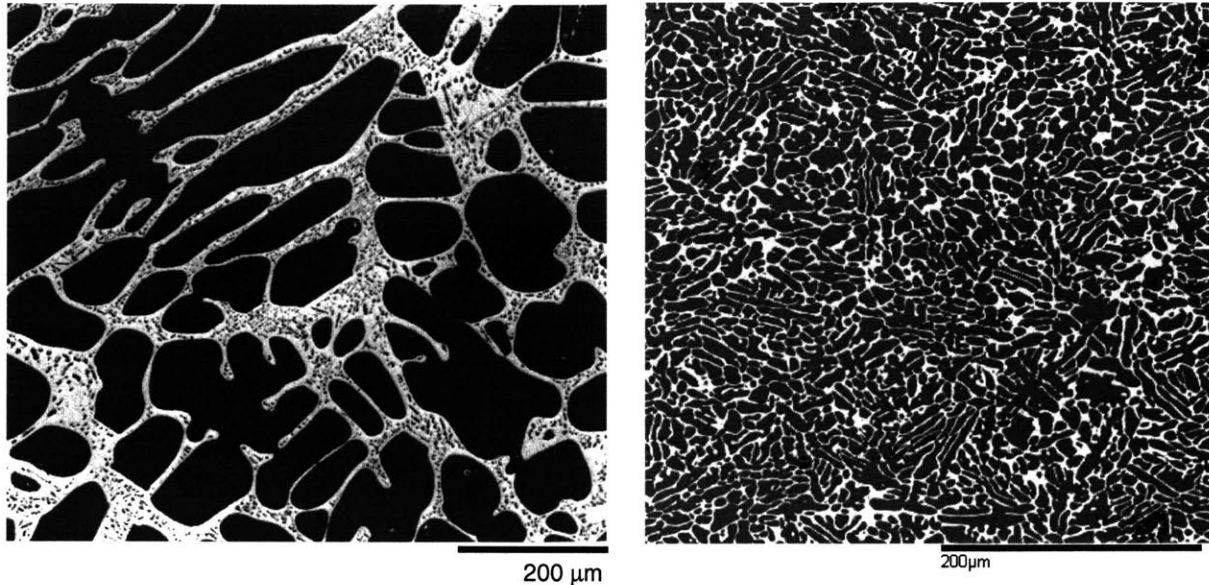
| (a) | (b) |

Figure 2.2. Microstructures of (a) an as-cast Zn-15wt% Sn alloy [Mehrabian et al. 1977] and (b) prepared Zn-20wt% Sn alloy.

Table 2.1. Thermophysical properties of substrate materials [Touloukian 1970, Brandes and Brook 1992, Omega Engineering, Inc.]

Material	ρ (kg/m^3)	T (K)	k (W/mK)	c_p (J/kgK)	α (10^{-6}m^2/s)
Soda-lime plate glass	2500	293	1.31	767	0.68
		366	1.52	871	
		478	1.73	996	
		589		1088	
Titanium (CP GR2)	4400	297	16.4	523	7.1
		373	15	540	
		473	15	569	
		673	14	619	
Aluminum (1200)	2700	297	237	903	97
		373	240	949	
		673	228	1033	

29

titanium
substrate

Zn-20wt% Sn
deposit

pyrometer

glass plate
with conductive
paste

thermocouple (0.5mm dia)
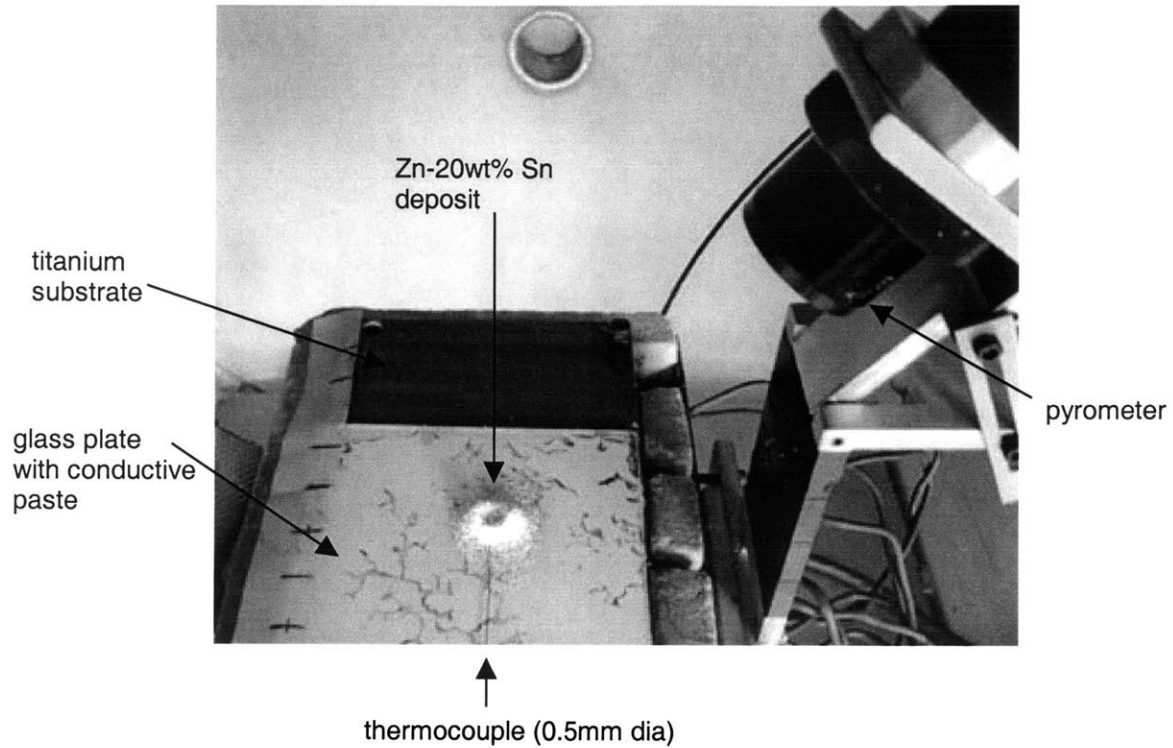
Figure 2.3. The Accufiber pyrometer is mounted above the substrate at a 55°
angle and a type-K thermocouple is fastened on top of the substrate surface.
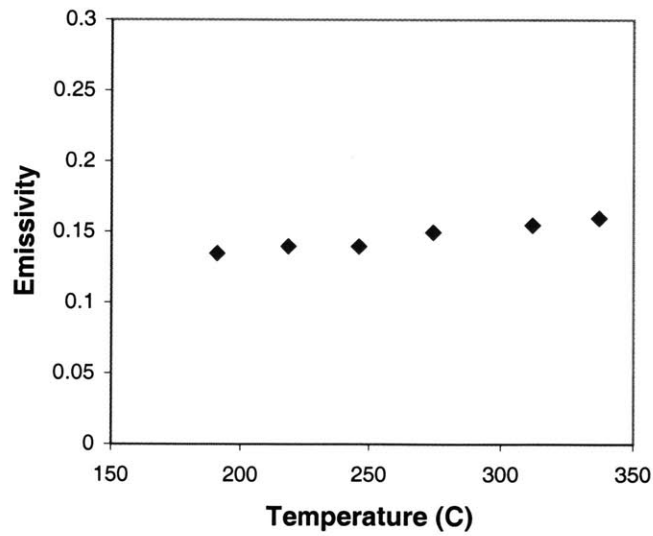
Figure 2.4. The emissivity of a typical Zn-20wt% Sn deposit over a range of
temperatures measured by a surface thermocouple.

30
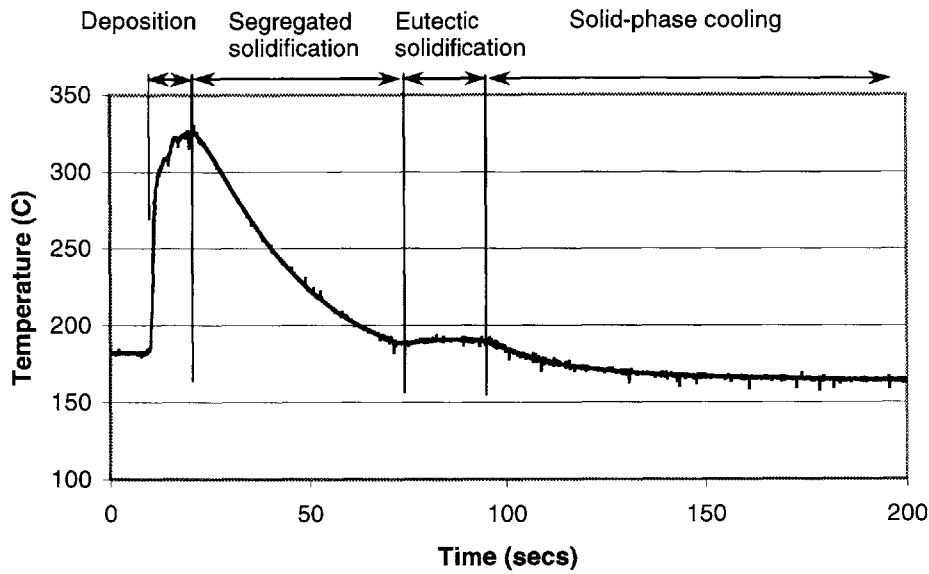
Figure 2.5. Preliminary temperature data acquired from the deposit surface *in situ* with the Accufiber sensor. Emissivity set at 0.15.
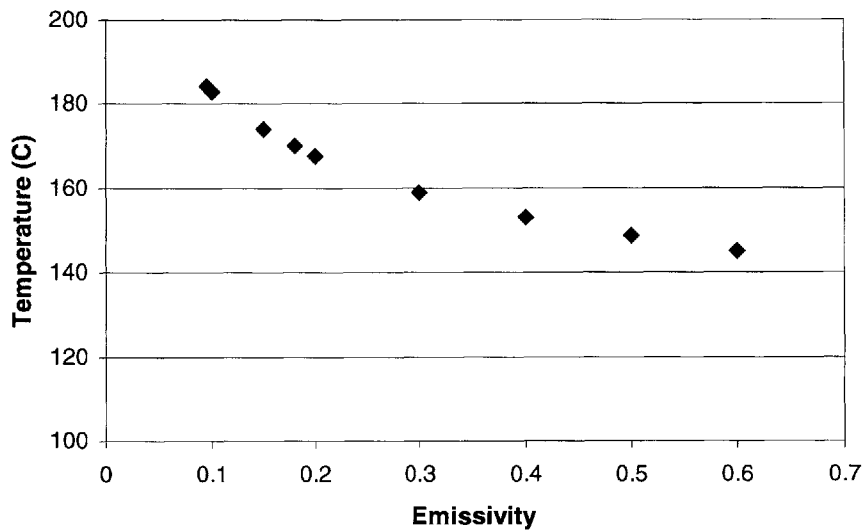
Figure 2.6. The effect of changing emissivity on the temperature output of the Accufiber sensor, while maintaining constant deposit temperature.
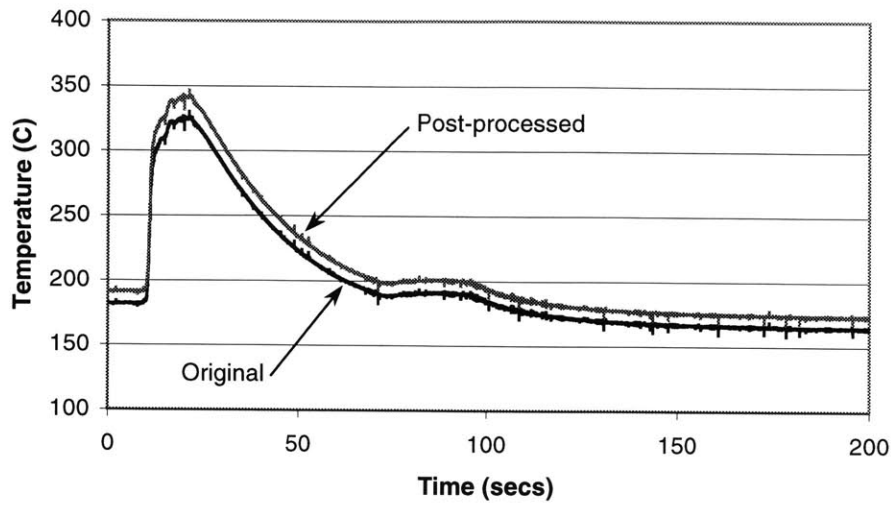
Figure 2.7. Post-processed temperature curve of the original Accufiber sensor output shown in Fig. 2.4.

10 mm
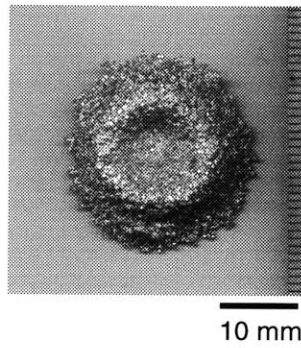
Figure 2.8. Photo of a typical UDS deposit.

Table 2.2. Process parameters along with design parameters used to spray eleven different deposits.

	A	B	C	D	E	F	G	H	I	J	K
substrate material	glass	glass	glass	glass	glass	glass	glass	titanium	titanium	aluminum	titanium
substrate temp [C]	160	160	160	160	120	120	120	175	175	170	125
orifice dia [μm]	175	200	150	150	200	200	200	200	200	200	200
breakup freq [khz]	4.38	4.3	4.17	4.37	4.37	4.36	4.35	4.37	4.36	4.35	4.36
melt temp [C]	438	437	442	442	437	438	439	437	438	440	438
mass flow rate [g/s]	0.62	0.62	0.41	0.38	0.75	0.7	0.72	0.75	0.71	0.74	0.7
spray area[mm²]	300	330	220	205	370	410	540	315	600	350	370
mass flux [g/s/mm²]	2.1	1.9	1.9	1.9	2.0	1.7	1.3	2.4	1.2	2.1	1.9
drop dia [μm]	344	346	304	292	366	358	362	366	360	365	358
drop temp [C]	376.9	375.8	374.6	373.3	377.0	376.3	376.3	377.2	376.3	377.4	376.6
drop lqd frac [%]	90	85	81	76	90	87	87	91	87	92	89
deposit emissivity	0.10	0.10	0.16	0.17	0.10	0.08	0.09	0.10	0.12	0.10	0.10

33

Table 2.3. Metrics derived to describe the deposit thermal history.

	A	B	C	D	E	F	G	H	I	J	K
deposit solid frac [%]	63	63	65	68	66	65	68	71	75	74	73
initial solid rate [C/s]	6.1	8.3	6.5	6.3	13.9	13.4	14.3	18.9	19.2	23.3	27.0
time to eutectic [s]	45.0	43.0	41.0	38.0	30.0	24.0	21.0	17.0	12.0	9.0	7.0
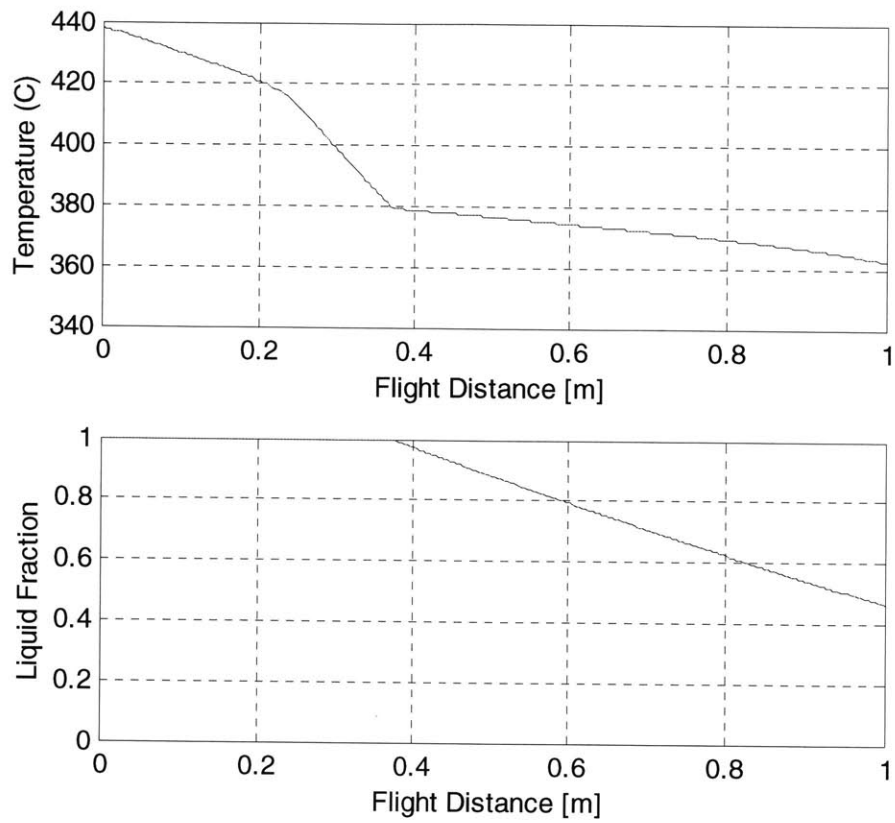
Figure 2.9. Droplet thermal state of a Zn-20wt% Sn droplet, 358 µm in diameter, traveling at 3.3 m/s, as predicted by the droplet thermal model.
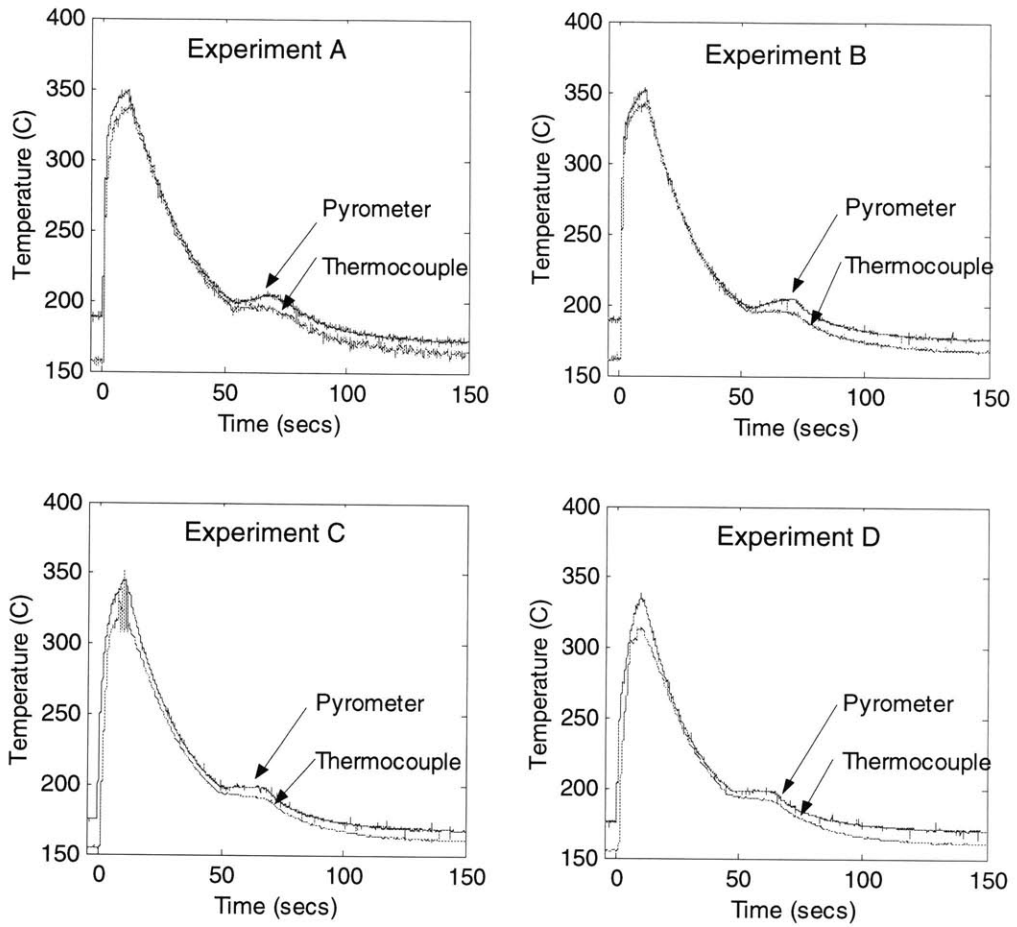
Figure 2.10. Temperature curves measured by the pyrometer and thermocouple during Experiments A through D, which were all sprayed onto glass plates with an initial surface temperature at 160˚C.
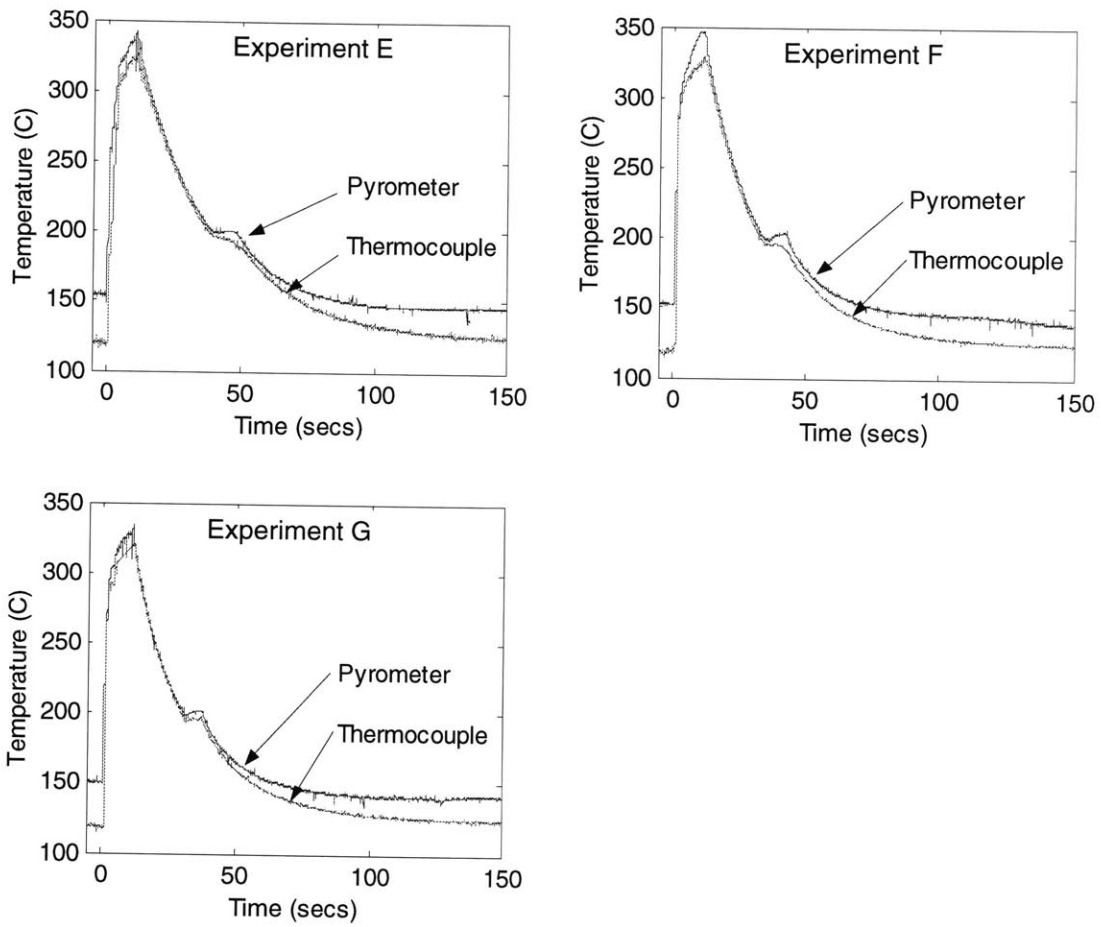
Figure 2.11. Temperature curves measured by the pyrometer and thermocouple during Experiments E through G, which were all sprayed onto glass plates with an initial surface temperature at 120°C.
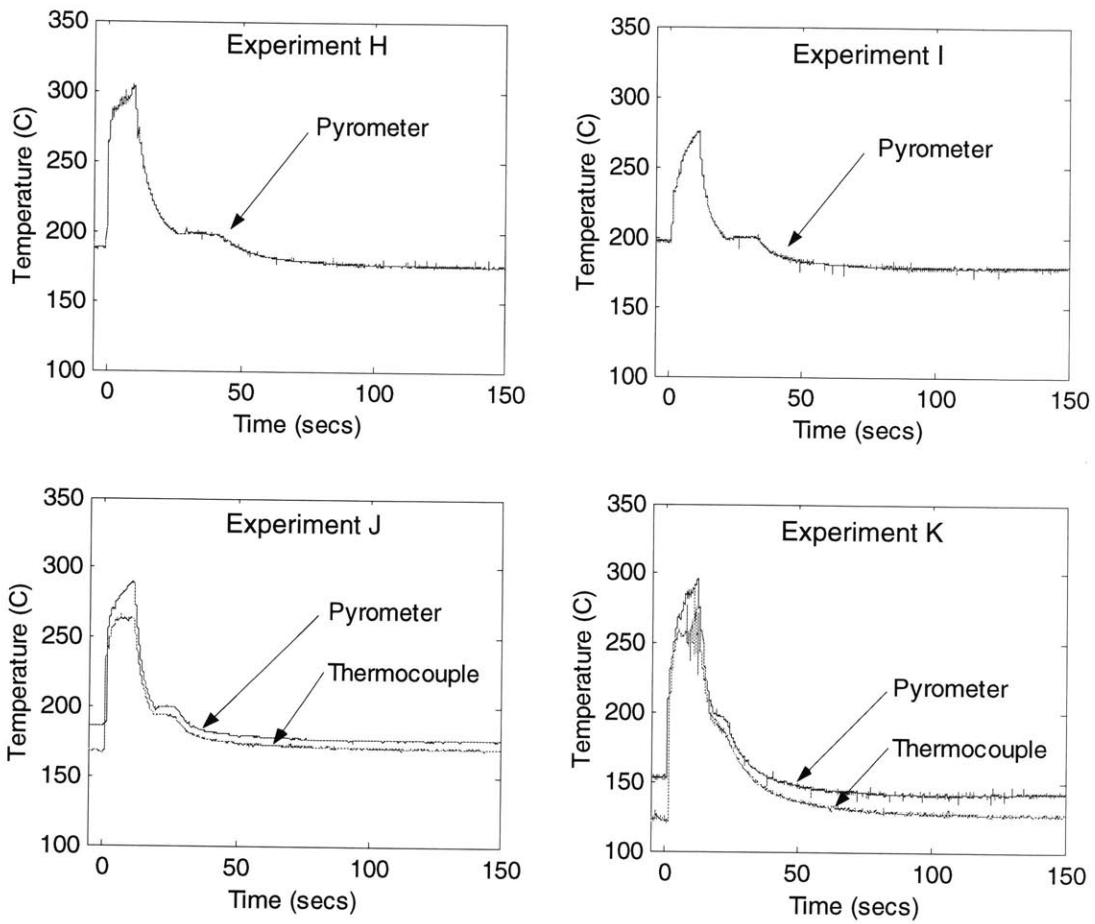
Figure 2.12. Temperature curves of deposits sprayed onto metal substrates, specifically Experiments H through K.
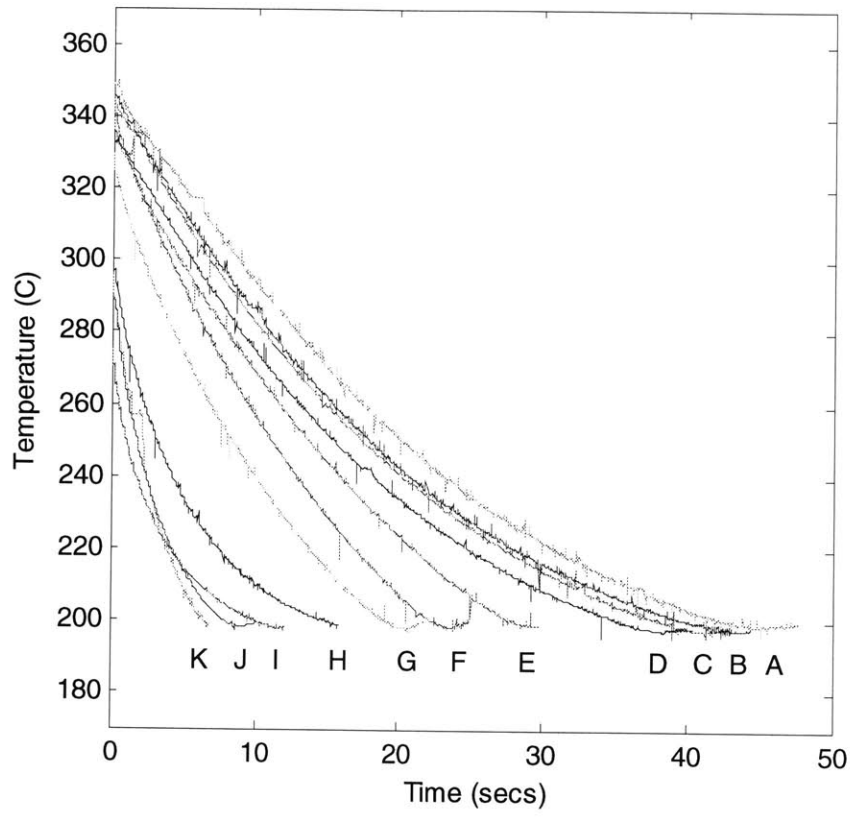
Figure 2.13. Compilation of the cooling curves during all the deposition experiments.

Chapter 3. DEPOSIT THERMAL MODEL

3.1 Introduction

In addition to measuring the deposit thermal history and its effect on deposit microstructure, another component of this study is developing a model to predict the thermal state of the deposit during and after deposition from the process parameters. Such a deposit thermal model allows for more thorough investigation of process parameter effects, which can thereby increase the controllability and flexibility of the UDS forming process.

Therefore, the deposit thermal model should be as robust as possible and allow for easy handling of the process parameters. After a survey of commercially available finite element software, ABAQUS (Hibbitt, Karlsson, and Sorensen, Inc., Pawtucket, RI) was chosen to model the transient heat transfer in the UDS process, mainly because its computation procedure is based on a sequence of events, or "steps." In each step, the user can apply new loads, boundary conditions, and/or time integration parameters. This feature is very convenient for modeling the incremental growth of the deposit material. Furthermore, the software is capable of computing the nonlinear effects of latent heat during alloy solidification.

The spray deposition process is simulated by considering the deposit to grow in continuous layers rather than in discrete individual droplets. This approximation is acceptable since the deposition rate is on the order of 10^3 droplets per second. In each analysis step, a layer of spray material is added to the deposit top surface and the deposit cools until the next layer is added. The appropriate thickness of each step layer is discussed in Section 3.6.3. After spray deposition, the deposit is allowed to cool to the steady state temperature. The model does not include the effects of convective liquid flow within the deposit or of the droplets as they impinge on the deposit. The release of latent heat during solidification is formulated by using an effective heat capacity method.

Since the thermal mass of the deposit is much smaller than that of the substrate, a one-dimensional model was initially developed to predict the deposit thermal state. However, this model was shown to be insufficient for deposits on metal substrates, so a two-dimensional, axisymmetric model was developed. This chapter describes the development of both 1-D and 2-D ABAQUS models and compares the results of the simulation to those of the deposition experiments.

40

3.2 Governing Equations

In general, the transient heat conduction within the deposit and substrate material is governed by the heat diffusion equation based on Fourier's Law:

$$\rho \frac{\partial H}{\partial t} = \nabla \cdot k \nabla T \qquad (3.1)$$

where ρ is the density of the material, H is the enthalpy per unit mass, k is the thermal conductivity, T is the temperature at any point in the material, and ∇ is a three-dimensional gradient vector operator that depends on the coordinate system employed. ABAQUS uses the specific heat, c_p, of a material to describe enthalpy as a function of temperature under constant pressure, as:

$$c_p(T) = \frac{\partial H}{\partial T} \qquad (3.2)$$

Therefore, the time rate of change of enthalpy can be expressed as:

$$\frac{\partial H}{\partial t} = c_p(T) \frac{\partial T}{\partial t} \qquad (3.3)$$

However, when the material experiences a phase change, ABAQUS includes the latent heat by increasing the effective specific heat, c_{eff}, of the material:

$$c_{eff} = c_p(T) + \frac{\Delta H_f}{(T_l - T_s)} \qquad (3.4)$$

where ΔH_f is the latent heat of fusion per unit mass and T_l and T_s are the liquidus and solidus temperatures, respectively. Equation 3.4 assumes that the latent heat is independent of temperature and that the solid fraction varies linearly with temperature between the T_l and T_s.

While this "straight-line approximation" of latent heat effects works well for pure metals or single-phase alloys, it ignores the solute diffusion during solidification in two-phase alloys, such as Zn-20wt% Sn. Therefore, to determine the enthalpy of the solid-plus-liquid mixture, or mushy zone, the Scheil segregation model is incorporated into the ABAQUS model.

41

3.3 Solute Redistribution in the Mushy Zone

Using ABAQUS, the heat transfer during deposit solidification is modeled macroscopically, neglecting any nucleation or growth undercooling. Furthermore, this model does not track the solidification front with separate solid and liquid regions because the Zn-20wt% Sn alloy has an appreciable mushy zone from 198.5°C to 379°C, as shown in the phase diagram in Appendix A. Therefore, the enthalpy of a representative unit volume in the mushy zone, H_m, is defined as:

$$H_m = f_s H_s + (1 - f_s)H_l \tag{3.5}$$

where f_s is the volume fraction of solid in the mushy zone, and H_l and H_s are the liquid phase and solid phase enthalpies, respectively [Poirier and Nandapurkar 1988]. H_l and H_s depend on their solute concentrations, as shown by:

$$H_l = C_l H_{Sn,l} + (1 - C_l)H_{Zn,l} \tag{3.6}$$

$$H_s = C_s H_{Sn,s} + (1 - C_s)H_{Zn,s} \tag{3.7}$$

where C_l and C_s are the weight percents of Sn in the liquid and solid phase, respectively, $H_{Sn,l}$ and $H_{Zn,l}$ are the enthalpies of pure Sn liquid and pure Zn liquid, respectively, and $H_{Sn,s}$ and $H_{Zn,s}$ are the enthalpies of pure Sn solid and pure Zn solid, respectively. The enthalpies of pure Sn and Zn are given as functions of temperature in Appendix A.

To incorporate Equation 3.5 into the ABAQUS model, f_s, C_l, and C_s must be expressed in terms of temperature. When the alloy is fully liquid above its liquidus temperature, f_s is equal to zero and C_l is equal to the original composition of the alloy. Likewise, when the alloy is fully solid below its solidus temperature, f_s is equal to one and C_s is equal to the original composition of the alloy. When alloy is in the mushy zone, f_s, C_l, and C_s depend on the segregation model used to describe solute redistribution.

The Scheil equation is employed in this simulation to determine f_s, C_l, and C_s. The Scheil equation assumes local equilibrium at the solid/liquid interface, complete solute mixing in the liquid, and no diffusion in the solid. As a result, the solute concentration in the liquid is related to the solid fraction in the system by the following expression:

$$C_l = C_o(1 - f_s)^{(k-1)} \tag{3.8}$$

where C_o is there original concentration of solute in the alloy system and k is the equilibrium partition coefficient [Kurz and Fisher 1998]. The equilibrium partition coefficient is defined as the ratio of the solute concentration in the solid to the solute concentration in the liquid at the solid/liquid interface. In the case of the Zn-20wt% Sn alloy, the solute concentration in the solid phase is nearly zero and thus, k is equal to zero. Equation 3.8 is rewritten as:

$$(1 - f_s) = \frac{C_o}{C_l} \tag{3.9}$$

where C_l is a function of temperature as described by the liquidus curve in the Zn-Sn phase diagram, shown in Appendix A.

With these relationships, the enthalpy of the Zn-20wt% Sn alloy can be directly related to temperature. Figure 3.1 shows a plot of the resulting enthalpy-temperature curve of the alloy compared to the straight-line approximation. This curve is incorporated into the ABAQUS model by tabulating the effective specific heat of the alloy as a function of temperature.

As the alloy material solidifies, solute redistribution stops when the temperature reaches the eutectic temperature of the Zn-Sn alloy system. In Figure 3.1, the enthalpy curve shows a discontinuous drop in enthalpy at the eutectic temperature. This is because the remaining fraction of liquid solidifies into a single-phase eutectic at a constant temperature. Eutectic solidification is simulated by using the latent heat option provided in ABAQUS. In this case, the straight-line approximation is appropriate. The liquidus temperature is set equal to the eutectic temperature and the solidus temperature is set one degree below the eutectic temperature. The latent heat input value is set equal to the remaining latent heat of fusion at the eutectic temperature.

3.4   Temperature-Dependent Material Properties

As noted previously, ABAQUS allows for temperature-dependent material properties to be tabulated. The density, thermal conductivity, and specific heat of the substrate materials: titanium, glass, and aluminum, are tabulated for a range of temperatures as shown previously in Table 2.1.

Similar to the enthalpy of the mushy zone, the phase change in the deposit material also affects the density and thermal conductivity of the deposit material. The density of the mushy zone is

equal to:

$$\rho_m = f_s \rho_s + (1 - f_s) \rho_l \tag{3.10}$$

where ρ_s and ρ_l are the densities of the solid and liquid phases of the alloy, respectively. While the ρ_s is simply equal to the solid density of pure Zn, ρ_l depends on the solute concentration, as shown by:

$$\rho_l = \left[\frac{C_l}{\rho_{Zn,l}} + \frac{1 - C_l}{\rho_{Sn,l}} \right]^{-1} \tag{3.11}$$

where $\rho_{Zn,l}$ and $\rho_{Sn,l}$ are the liquid densities of pure Zn and Sn, respectively.

The thermal conductivity of the mushy zone is commonly approximated by:

$$k_m = f_s k_s + (1 - f_s) k_l \tag{3.12}$$

where k_s and k_l are the conductivities of the solid and liquid phases of the alloy, respectively [Bianchi and Viskanta 1995]. While k_s is equal to the thermal conductivity of solid Zn, k_l is given by:

$$k_l = C_l k_{Sn,l} \frac{\rho_l}{\rho_{Sn,l}} + (1 - C_l) k_{Zn,l} \frac{\rho_l}{\rho_{Zn,l}} \tag{3.13}$$

where $k_{Sn,l}$ and $k_{Zn,l}$ are the conductivities of liquid Sn and liquid Zn, respectively.

The solid fraction-temperature relationship derived from the Scheil equation is used to tabulate the density and thermal conductivity of Zn-20wt% Sn as functions of temperature during solidification. Appendix A gives the results of these calculations for the alloy material properties. Figure 3.2 shows the effect of using the Scheil equation compared to using the straight-line approximation in a simple 1-D model of the deposit thermal history. As predicted by the enthalpy-temperature curves in Fig. 3.1, the straight-line approximation results in a significantly slower cooling rate.

3.5 Computational Considerations

ABAQUS uses an iterative Newton method modified to solve nonlinear heat transfer problems.

First order elements are preferred and utilized in these simulations to handle the strong latent heat effects. As a result, the heat capacity terms are lumped and the internal energy storage term is integrated at the nodes. A detailed description of the solution method for uncoupled heat transfer analysis can be found in the ABAQUS/Standard Theory Manual [2000].

Time integration in the transient problem is performed with the backward Euler method. Time is incremented automatically by ABAQUS based on the user-specified maximum allowable temperature change at any node. Automatic time increments reduce the number of computation steps as the temperature approaches a steady-state value. The user suggests the initial time increment from which ABAQUS will begin its iterations, and the time period at which each analysis step ends. For these simulations to converge, the initial time increment was specified to be 10^{-8} s. The maximum allowed change in temperature within each time increment was set at 50K during deposition, and at 10K after deposition to capture the eutectic solidification plateau.

3.6   One-Dimensional Deposit Thermal Model

The relatively high thermal conductivity and small thermal mass of the Zn-20wt% Sn deposit compared to that of the substrate material led to the assumption that transverse temperature gradients are negligible within the deposit and substrate. Therefore, a one-dimensional model was initially developed to predict the deposit thermal history. After constructing the model geometry and mesh, the model requires several additional inputs, including the incremental growth rate of the deposit, the initial and boundary conditions, and the interfacial contact resistances.

3.6.1   Model geometry and mesh

The deposit and substrate are modeled as a vertical column of quadrilateral solid elements of uniform width. Figure 3.3 shows the model geometry near the deposit/substrate interface. Rather than using 1-D link elements, quadrilateral elements were employed so that contact surfaces could be defined for thermal interaction. For example, as shown in Figure 3.3, there is a gap between the deposit and substrate. This gap is used to model the interfacial thermal contact resistance by prescribing a heat transfer coefficient between the two surfaces. Surface interactions are described in more detail in Section 3.6.4

While the width of the elements is arbitrary since there are no transverse temperature gradients, the thickness of the elements can affect the simulation accuracy. Mesh convergence tests were conducted to determine the appropriate deposit element thickness. The mesh spacing (i.e., element thickness) was varied while keeping the spray conditions constant: Zn-20wt% Sn spray material at 650K is deposited onto the titanium substrate at 448K. The deposit growth rate was

set at a typical growth rate: 100 µm per 0.4-s time step. Figure 3.4 shows the temperature curves of the deposit surface resulting from the simulations with 10-µm, 25-µm, 50-µm, and 100-µm uniform mesh spacing in the deposit. The results show that the temperature curves converge as the mesh spacing decreases to 10 µm. The temperature curve that resulted from using a 5-µm uniform mesh is equivalent to the curve shown for a 10-µm mesh. Thus, the deposit is discretized into elements of uniform thickness equal to 10 µm.

For the substrate, the 12-mm thick titanium block is modeled with elements of increasing thickness away from the deposit/substrate interface. The initial thickness of the substrate elements is equal to 10 µm and the final thickness is equal to 500 µm. When necessary, the 2.2-mm thick glass plate or the 1.6-mm thick aluminum plate is modeled above the titanium block with 10-µm thick elements.

3.6.2 Deposit growth rate

In the UDS forming process, the electrical repulsion among the droplets in a single-orifice spray creates a non-uniform distribution of mass flux over the deposit area. Figure 2.8 previously showed the crater-like geometry of a typical deposit. Therefore, the vertical growth rate of the deposit in the peak section is significantly faster than the growth rate in the valley section. It is unclear whether the non-uniform distribution of heat flux will lead to large temperature gradients across the deposit diameter, despite the high thermal conductivity of the deposit material.

If we assume there is no transverse heat conduction, then the 1-D deposit thermal model should correlate to the location of the temperature measurement on the deposit surface. For example, if the surface measurement was on a peak section, the deposit growth rate is set equal to the height of the peak section divided by the total spray duration. This method uses a local deposit growth rate.

An alternative model of the deposit growth rate is an average growth rate, which assumes that the incoming mass flux is distributed uniformly over the deposit area. In other words, the average growth rate, $(dh/dt)_{avg}$ is expressed by:

$$\left(\frac{dh}{dt} \right)_{avg} = \frac{\dot{m}}{\rho_{drop} A_{dep}} \tag{3.14}$$

where $\dot{m}$ is the mass flow rate of the spray, ρ_{drop} is the density of the incoming droplets, and A_{dep} is the surface area of the bottom of the deposit. Thus, the total height of this deposit model is equal to the average growth rate multiplied by the deposition time.

Figure 3.5 illustrates the two different methods of determining the growth rate of the deposit

assuming 1-D heat conduction. The local and average deposit growth rates are calculated for each experiment and applied to the 1-D thermal model for comparison. Given the deposit growth rate, it is also necessary to determine the thickness of the layer added to the deposit in each analysis step. The incremental layer thickness, referred to as step size, determines the time period of the step and it can affect the accuracy of the simulation.

3.6.3 Step size during deposition

Physically, the UDS deposit grows discretely one splat at a time. However, as mentioned before, the ABAQUS model idealizes the deposition process as the deposition of continuous layers. The minimum thickness of each layer can be physically related to the thickness of the splats. However, the splat morphology varies during deposition due to the changing thermal state and surface roughness of the growing deposit. Nonetheless, it is useful to use the initial splat thickness to model the step size during spray deposition. Thus, some splats were collected from the deposition experiments and their diameters were measured using an optical microscope. Assuming the splats resemble cylindrical disks, the average thickness of the splats was estimated to be about 150 μm, ranging from 60 μm to 180 μm in the different experiments conducted.

The sensitivity of the simulation to the step size during deposition was tested to justify neglecting variations in step size. Figure 3.6 shows the simulated temperature curves at the bottom deposit surface using different step sizes (while keeping overall growth rate constant) for the deposit produced in Experiment B. The temperature curves during deposition shows that using bigger step sizes and hence, longer time steps, increases the amplitude of the temperature oscillations. However, from a step size of 50 μm to 200 μm, there is little change in the overall temperature history of the deposit. Therefore, a step size of 150 μm is employed in all of the 1-D deposition simulations.

3.6.4 Initial and boundary conditions

The initial temperature of the deposit elements is determined from the process parameters and droplet solidification model described in Chapter 1. The deposit elements are added to the model at the same initial temperature since the effect of the growing deposit height is negligible. The initial temperature across the titanium substrate block was measured by a pair of imbedded thermocouples. Since the thermocouples measured less than a 5°C temperature gradient across the titanium thickness, the titanium substrate block is modeled to be initially isothermal. The temperature of the top surface of the glass plate was measured by a surface thermocouple, and indicated a bigger gradient within the glass plate than the titanium block. Thus, the nodes within the glass plate elements are assigned initial temperatures that correspond to a linear gradient from the top surface of the glass to the top surface of the isothermal titanium block. The surface temperature of the aluminum plate measured by the thermocouple shows less than a 5°C

47

temperature gradient within the aluminum plate. Therefore, the initial temperature of the aluminum plate is also modeled to be isothermal.

A constant temperature boundary condition is applied to the bottom surface of the titanium substrate block. The left and right surfaces of all the quadrilateral elements are modeled as adiabatic for 1-D heat conduction. The top surface of the deposit at the end of deposition experiences natural convection and radiation to the environment. The temperature of the ambient gas was measured and modeled to be 30°C.

The natural convection heat transfer coefficient, h_{conv}, from the deposit surface can be approximated by an empirical correlation for a heated horizontal plate [Incropera and DeWitt 1990]

$$h_{conv} = 0.54 \frac{k_g}{L} Ra_L^{0.25}$$ (3.15)

where k_g is the thermal conductivity of the ambient gas at the film temperature, L is the characteristic length the horizontal plate, and Ra_L is the associated Rayleigh number. L is equal to the plate surface area divided by its perimeter, and Ra_L is defined as:

$$Ra_L = \frac{g\beta(T_s - T_\infty)L^3}{v_g \alpha_g}$$ (3.16)

where g is gravitational acceleration, β is the volumetric thermal expansion coefficient equal to $1/T_f$ for an ideal gas, T_s is the deposit surface temperature, T_∞ is the ambient gas temperature, and α_g and v_g are the thermal diffusivity and kinematic viscosity of the ambient gas, respectively. All material properties of the gas are evaluated at the film temperature, $T_f = (T_s + T_\infty)/2$.

For the sprayed deposit, to approximate L, the top surface area is assumed to be a flat circular area equal to the bottom surface area of the deposit. Thus, a typical value of L is 5.4 mm and the average heat transfer coefficient for natural convection is 22.5 W/m²K. By assuming the surface of the sprayed deposit to be flat, the derived heat transfer coefficient becomes an upper-bound estimate since underestimating the surface area within the perimeter of the deposit decreases L, which increases h. The sensitivity of the 1-D thermal model to the coefficient for natural convection was tested. Figure 3.7 shows that decreasing the value of h_{conv} reduces its effect on the deposit cooling behavior.

Radiation from the deposit surface after spray deposition is also included in the ABAQUS model by specifying the surface emissivity, ε, ambient gas temperature and the Stefan-Boltzman constant, σ. For comparison to h_{conv}, the heat transfer coefficient for radiation, h_{rad}, is calculated by:

48

$$h_{rad} = \frac{\varepsilon\sigma(T_s^4 - T_\infty^4)}{(T_s - T_\infty)} \qquad (3.17)$$

where T_s and T_∞ are expressed in terms of Kelvin. The maximum radiative heat transfer coefficient for the deposit surface is found to be about 2.5 W/m^2K.

To gauge the accuracy of the predicted values of h_{conv} and h_{rad}, the steady-state heat loss from the surface of the bare titanium substrate at 175°C was measured with the imbedded thermocouples in the substrate. Energy balance requires that the rate of conduction through the titanium substrate is equal to the rate of convection from the substrate surface. As a result, the data revealed an effective heat transfer coefficient to the ambient gas of about 18 W/m^2K. This value is comparable to the sum of the predicted heat transfer coefficients for natural convection and radiation from the deposit surface.

3.6.5 Contact resistance

As mentioned before, the 1-D deposit thermal model includes the interfacial contact resistance between the deposit and the substrate by prescribing a heat transfer coefficient between the two surfaces. Within the deposit, the deposit layers are assumed to be in perfect contact.

The value of the interfacial heat transfer coefficient between spray-formed materials and their substrates has been the subject of much research. A survey of literature found that reported coefficient values range from 5×10^3 to 2×10^5 W/m^2K for a variety of materials and spray conditions [Annavarapu et al. 1990, Wang and Matthys 1996, Waldvogel and Poulikakos 1997, Pasandideh-Fard et al. 1998]. Furthermore, many authors report that the heat transfer coefficient decreases during solidification of the deposit material, due to material shrinkage [Annavarapu et al. 1990, Wang and Matthys 1996].

Due to the uncertainty of the interfacial heat transfer coefficient, h_{int}, a constant value of 10^5 W/m^2K was initially assigned in the thermal model. The relatively high value of h_{int} is supported by evidence of strong adhesion between the sprayed deposit and glass substrate. Sensitivity of the thermal model to a constant heat transfer coefficient value was tested for different substrate materials. Figure 3.8 shows that model is more sensitive to the coefficient value when the substrate material is titanium than when it is glass.

Contact resistance also exists in the composite substrate. In the case of the aluminum plate, the silicone paste is modeled as an interfacial contact resistance between the aluminum plate and titanium block. The contact heat transfer coefficient was measured to be about 2×10^3 W/m^2K when the bottom surface temperature of the titanium block was set at 175°C. Since the thermal conductivity of the silicone paste (2.31 W/mK) is very similar to that of the glass plate, the glass plate is modeled to be in perfect contact with the titanium block.

3.6.6 Results from the 1-D deposit thermal model

Using the experimental conditions listed in Table 2.2, the deposit thermal histories were simulated with the 1-D thermal model and compared with the measured temperature curves for Experiments B, F, H, J, and K. As described in Sec. 3.6.2, two methods of representing deposit growth rate, local and average, were applied to the thermal model.

Since the thermal model calculates the temperature at each node location over time, it is necessary to compile the temperature data to track the temperature of the growing deposit surface. Furthermore, since the spray deposition is simulated as the addition of discrete layers, the temperature at any location in the deposit oscillates like a saw-tooth curve, as shown in Figure 3.6. The amplitude of the temperature oscillation subsides as the deposit thickness increases, except when tracking the temperature of the deposit surface. Therefore, for ease of comparison, the deposit surface temperature at the end of each time step is used to trace its temperature history during spray deposition.

Figures 3.9 compares the deposit surface temperature curves predicted by the 1-D thermal model to the deposit surface temperature measured *in-situ* by the pyrometer for Experiments B and F. As shown in this figure, using the average growth rate with the 1-D thermal model gives significantly better agreement with the experimental data than using the local deposit growth rate. The local growth rate, which is typically more than two times faster than the average growth rate, overestimates the deposit temperature significantly.

The 1-D thermal model was also used to simulate the spray conditions in Experiments H, J, and K using local and average growth rates. The simulation results are compared with the experimental data and shown in Figures 3.10 and 3.11. Unlike the deposition experiments on glass, neither of the temperature curves predicted by the 1-D thermal model agrees well with the pyrometer measurement. Both the local and average growth rates overestimate the solidification time of the sprayed deposits.

3.6.7 Discussion

For deposits sprayed onto a glass substrate, the 1-D thermal model more closely approximates the experimental temperature curves when using an average growth rate rather than the local growth rate. Since the local growth rate strictly assumes that the heat flux of the incoming droplets diffuses without any transverse conduction inside the deposit, it overestimates the deposit temperature significantly. Physically, the non-uniform distribution of heat flux arriving on the deposit probably leads to transverse conduction within the deposit since the deposit material has high thermal diffusivity. Therefore, the average growth rate gives a better approximation of the deposit thermal history since it averages the incoming heat flux across the

50

deposit surface area. This also explains how the 1-D thermal model can closely predict the solidification time of the deposit after deposition, although it cannot accurately predict the transient deposit temperature during spray deposition.

However, for deposits sprayed onto metal substrates, neither the local nor average growth rate gives a good approximation of the deposit solidification behavior. Therefore, there must be another source of heat loss that the model does not capture. Most likely, since the thermal diffusivities of the metal substrates are comparable to the diffusivity of the deposit material, the transverse heat conduction inside the substrate must also be considered. In contrast, the glass plate has lower diffusivity and acts as a thermal barrier between the deposit and the titanium substrate block. Furthermore, the transverse temperature gradients within the deposit itself are probably much smaller in deposits sprayed on glass than in deposits sprayed on metal substrates. Therefore, to improve the accuracy of the deposit thermal model for deposits sprayed on metal substrates, a 2-D axisymmetric thermal model was developed.

3.7 Two-Dimensional Axisymmetric Deposit Thermal Model

3.7.1 Model geometry, mesh, and deposit growth rate

The geometries of the sprayed deposits were approximated as 2-D axisymmetric deposits with straight edges, as demonstrated in Figure 3.12. Although the substrate block is much larger, its radius was initially modeled, and later qualified, as two times the maximum radius of the deposit. Figure 3.12 also shows the model geometry and mesh for Experiment B. The vertical mesh within the deposit is based on the thickness each deposition layer, which is determined by the deposit growth rate.

Unlike the 1-D thermal model, the deposit growth rate in the 2-D axisymmetric model should include the effects of the non-uniform distribution of mass flux in the spray process. To do so, the deposit geometry is divided into two sections of different growth rates: the valley section and the peak section. The rate of deposition in the peak section must be faster than that in the valley section such that the deposit reaches its final volume at the end of the spray duration. Furthermore, the total amount of volume added to the deposit in each time step must be constant to conserve mass. Therefore, an iterative algorithm was developed in MATLAB (Mathworks, Inc.) to calculate the rate of change of the deposit height in the each section. The deposit height in the valley section is set to increase by 100 μm per time step, and then the corresponding change in deposit height in the peak section is determined over time.

As an example, the algorithm is applied to the spray conditions in Experiment B, and the output is shown in Figure 3.13. The tick marks in Fig. 3.13 correspond to the incremental layers added

to the deposit in each time step. Each layer is further divided into elements with variable thicknesses less than 50 μm to compose the vertical mesh in the deposit. Although sensitivity tests of mesh spacing in the 1-D thermal model showed that the simulation results converge when the element thickness is less than 10 μm, an alternative mesh scheme was employed in the 2-D model to decrease the computation time and size of the output file. Rather than using elements of uniform thickness, 10-μm thin elements were used at each layer interface to capture the high temperature gradient and thicker elements were used to divide the remainder of each layer. Figure 3.14 shows that the deposit thermal history simulated by using this mesh scheme is equivalent to that simulated by using elements of uniform 10-μm thickness.

The vertical mesh in the substrate is generated automatically with ABAQUS such that there is a higher concentration of nodes near the interface with the deposit. For example, the aluminum plate has an initial spacing of 17 μm and final spacing of about 65 μm. The mesh in the radial direction uses 500-μm spacing which should be adequate to model radial conduction.

3.7.2 Boundary and initial conditions

The initial temperatures of the deposit and substrate elements in the 2-D thermal model are assigned in the same manner as they were assigned in the 1-D thermal model. A constant temperature boundary condition is applied to the bottom surface of the titanium substrate block. The centerline of the 2-D model and the right side of the substrate are prescribed to be adiabatic surfaces. The outer surfaces of the deposit are assumed to convect and radiate with the same heat transfer coefficients calculated in Sec. 3.6.4.

The interfacial heat transfer coefficient between the deposit and the substrate is set at 10^5 W/m^2K. Convection from the exposed surface of the substrate block not in contact with the deposit is also included in the model. Using Equations 3.15 and 3.16, the average h_{conv} from the substrate surface is calculated to be about 12 W/m^2K.

3.7.3 Results

The 2-D axisymmetric thermal model was applied to Experiments B, F, H, J, and K, which represent each tested combination of substrate material and temperature. Due to the significantly larger number of elements and nodes utilized in this model compared to the 1-D thermal model, the computation time increased from about 0.5 hours to 8 hours. Before comparing the simulation results to the experimental temperature measurements, the thermal gradients within the model for different substrate materials were examined.

Figures 3.15 through 3.17 show the simulated temperature profiles within the deposit and substrate immediately after spray deposition for Experiments B, H, and J, respectively. As

52

shown in Fig. 3.15, the deposit sprayed onto glass is virtually isothermal compared to the thermal gradients in the glass. Furthermore, the radial thermal gradients within the glass plate are about four times smaller than axial gradients within the glass plate. However, for the deposit sprayed directly onto metal substrates, Figs. 3.16 and 3.17 show that the radial thermal gradients are comparable the axial ones inside the substrate. This explains why the 1-D thermal model was sufficient to predict the solidification time for deposits on glass substrates, but underestimated the heat loss in deposits on metal substrates. In other words, radial heat conduction cannot be neglected when the substrate material has similar thermal diffusivity as the deposit material. Figures 3.15 through 3.17 also justify prescribing an adiabatic boundary condition on the right side of the substrate block, since the temperate profiles in the substrate are relatively flat as they approach the boundary.

3.7.4 Comparison of simulation to experimental results

Figure 3.18 compares the simulated thermal histories for the deposit surface temperature to the respective thermal histories measured *in situ* by the pyrometer in Experiments B, F, H, J, and K. The agreement between the simulation results and the experimental data has improved significantly with the 2-D axisymmetric thermal model, especially for deposits sprayed onto the titanium substrate. However, during spray deposition, the transient temperature of the deposit surface measured by the pyrometer is consistently greater than the simulated temperature. This is possibly due to incident background radiation captured by the pyrometer. After deposition, the pyrometer curve closely follows the simulated curve during solidification for most cases, except Experiment J. After solidification, the pyrometer curve begins to deviate from the simulated curve probably due to a change in surface emissivity or the lower temperature limit of the pyrometer, as mentioned earlier in Sec. 2.6.1.

To further verify the 2-D thermal model, the temperature of bottom surface of the deposit measured *in situ* by a thermocouple, which is not affected by emissivity variations, is compared to the bottom surface temperature predicted by the model. Figures 3.19 shows the comparison for Experiments B, F, J, and K (there was no thermocouple data available for Experiment H). First, it is noticeable that the simulation results closely match the steady-state temperature value measured by the thermocouple. Second, the simulation results for Experiments B and F agree with the thermocouple data as well as they agree with the pyrometer data.

However, Figure 3.19 shows that there is less agreement between the thermocouple and simulation data for Experiments J and K. The predicted temperature curves underestimate the measured values during spray deposition and overestimate the values after deposition. One potential source of error in the 2-D thermal model is the interfacial heat transfer coefficient between the deposit and the substrate. As discussed in Sec. 3.6.5, the value for h_{conv} at the deposit-substrate interface was set a relatively high value for all the simulations since there was

53

strong adhesion between the glass plate and the deposits sprayed on top of glass. Furthermore, this value of h_{conv} led to good agreement between the simulated and measured thermal histories of the deposits sprayed on glass. However, there was significantly less force required to remove the deposits sprayed onto metal substrates. Thus, it is possible that the interfacial heat transfer coefficient between the deposit and a metal is lower than that between the deposit and glass. Decreasing the interfacial heat transfer coefficient would cause the simulated curve to rise. However, it would adversely increase the discrepancy between the simulation and experimental curves after deposition. One explanation may be that the value of h_{conv} between the deposit and substrate is not constant during and after spray deposition. However, it is unlikely that h_{conv} increases after deposition since the deposit is solidifying and shrinking.

The discrepancy between the simulation and measured curves after deposition may be attributed to a greater contact resistance between the thermocouple and the deposit in Experiments J and K. Figure 3.20 shows a magnified view of the curves during solidification, and it is apparent that the thermocouple less accurately captures the eutectic temperature of the Zn-20wt% Sn alloy in Experiments J and K. It is possible that as the deposit cools rapidly, it contracts away from the stainless steel thermocouple, given the fact that the coefficient of thermal expansion of Zn is more than two times that of stainless steel. If a gap develops between the thermocouple and the deposit, then the thermocouple output would be less than the actual deposit temperature predicted by the simulation. Further work is necessary to isolate the cause of these discrepancies.

3.8   Conclusions

A 2-D axisymmetric finite element model has been developed to predict the deposit thermal state during UDS forming. In Chapter 2, the thermal histories of eleven sprayed deposits were measured and characterized by three metrics, namely, the deposit solid fraction just prior to solidification, the solidification rate of the deposit immediately after deposition, and the solidification time required for the deposit to reach the eutectic temperature after deposition. As shown in Figure 3.21, these metrics, which are calculated for the 2-D simulation results for Experiments B, F, H, J and K, are compared to the metric values obtained from the experimental data. The figure shows that the 2-D thermal model is slightly better at predicting the initial solidification rate than the total solidification time of the deposit, although there is relatively good agreement between the predicted and measured values for both metrics.

Having developed a model that can adequately predict the deposit thermal history given the process parameters, the following chapter discusses how the deposit thermal history influences the final deposit microstructure.
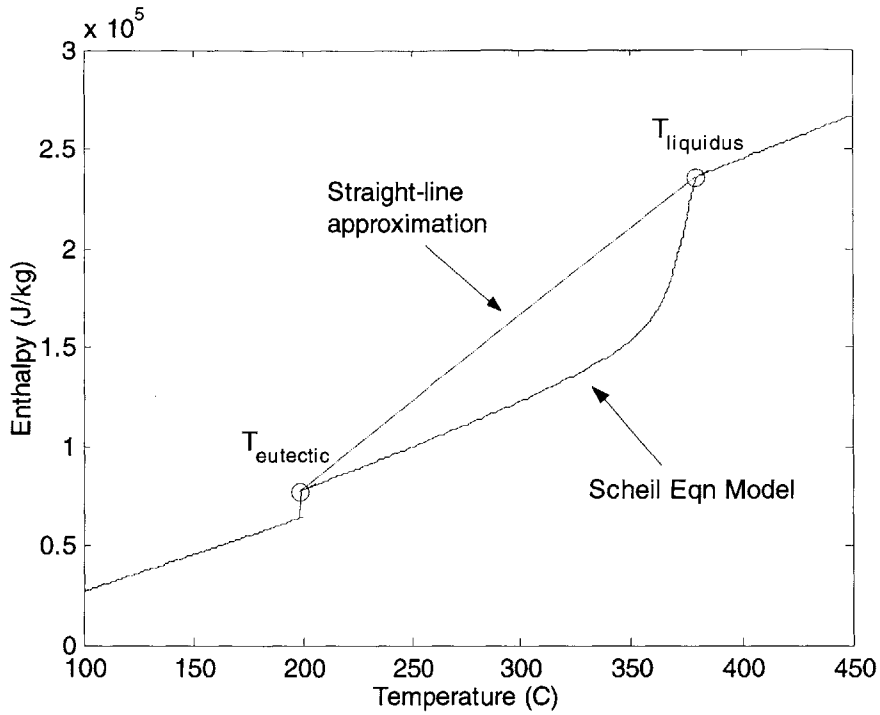
Figure 3.1. The enthalpy-temperature curve predicted by Scheil Equation compared to the straight-line approximation.
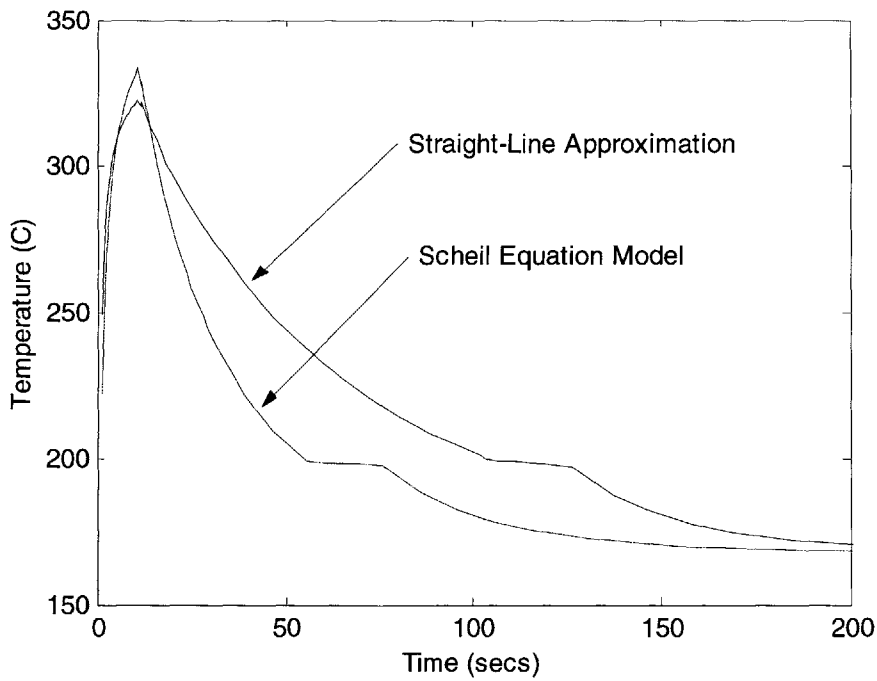

Figure 3.2. The effect of using the Scheil equation compared to using the straight-line approximation in a simple 1-D model of the deposit thermal history.
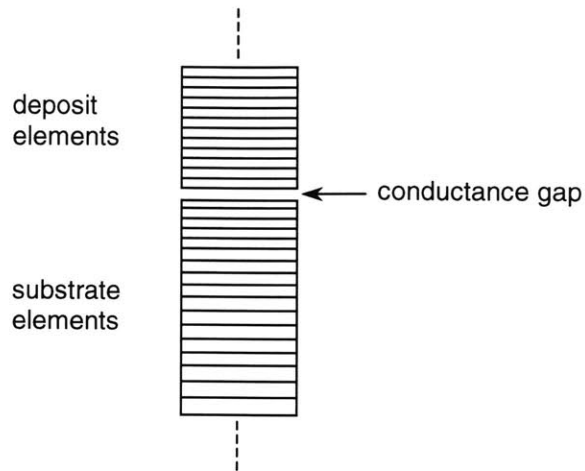
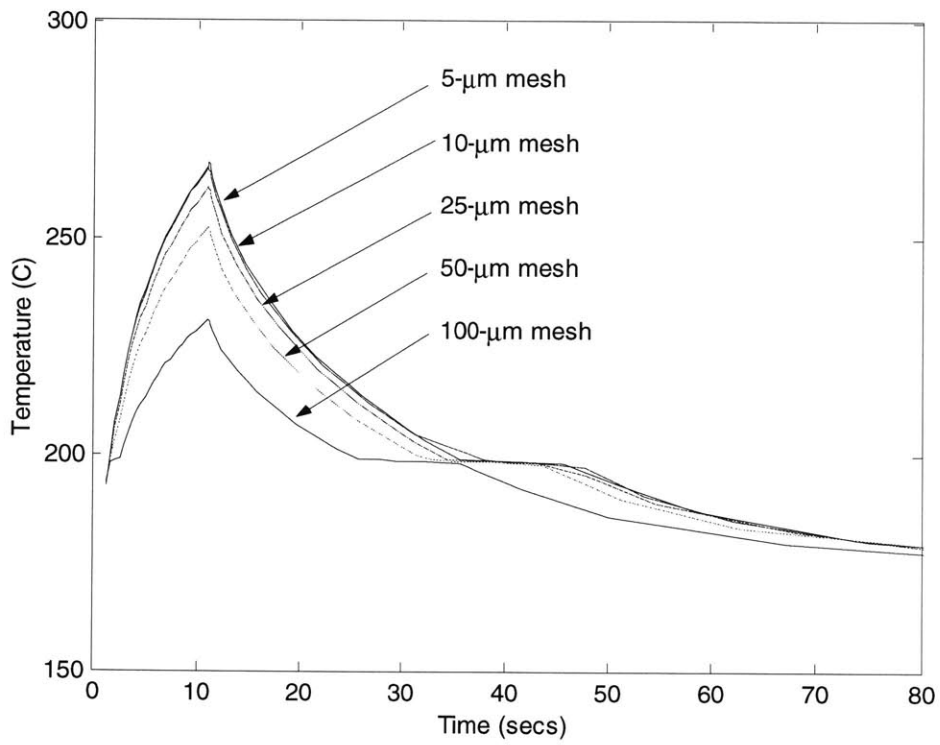Figure 3.3. The 1-D deposit thermal model geometry near the deposit-substrate interface.

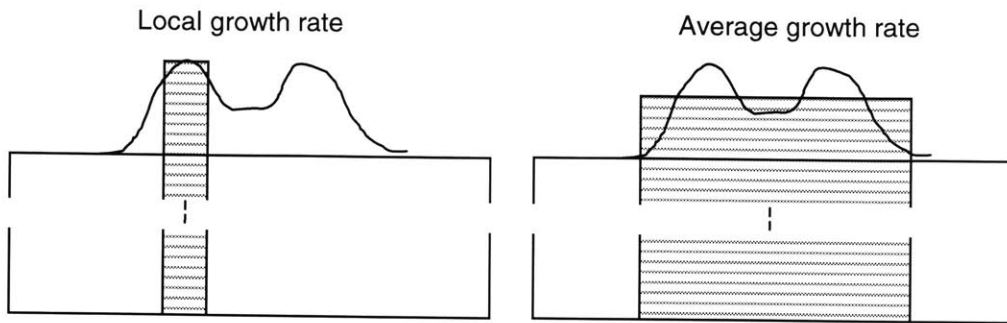Figure 3.4. The converging effect of decreasing mesh size in the 1-D model.

Figure 3.5. Approximating the growth rate of the deposit for the 1-D model.
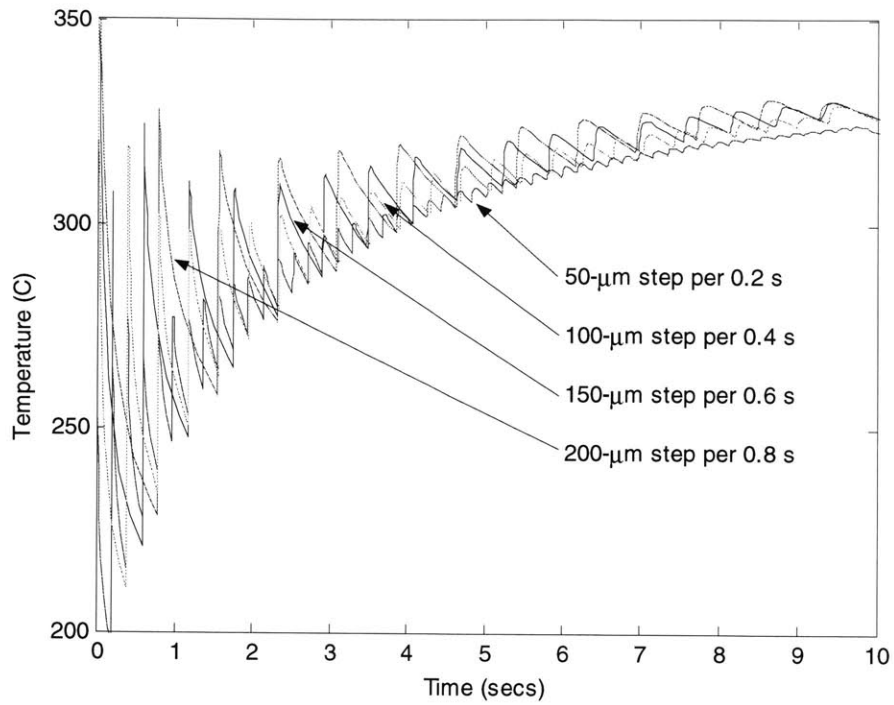
Figure 3.6. The effect of decreasing the step size during deposition, while keeping overall deposit growth rate constant, in the 1-D model.
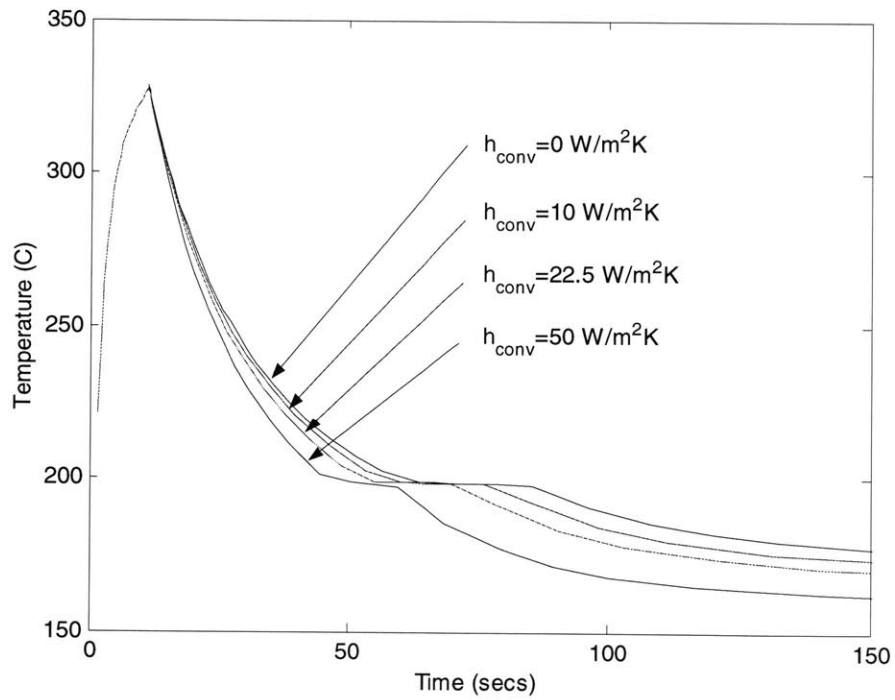

Figure 3.7. The effect of the heat transfer coefficient for natural convection from the deposit surface in the 1-D model.
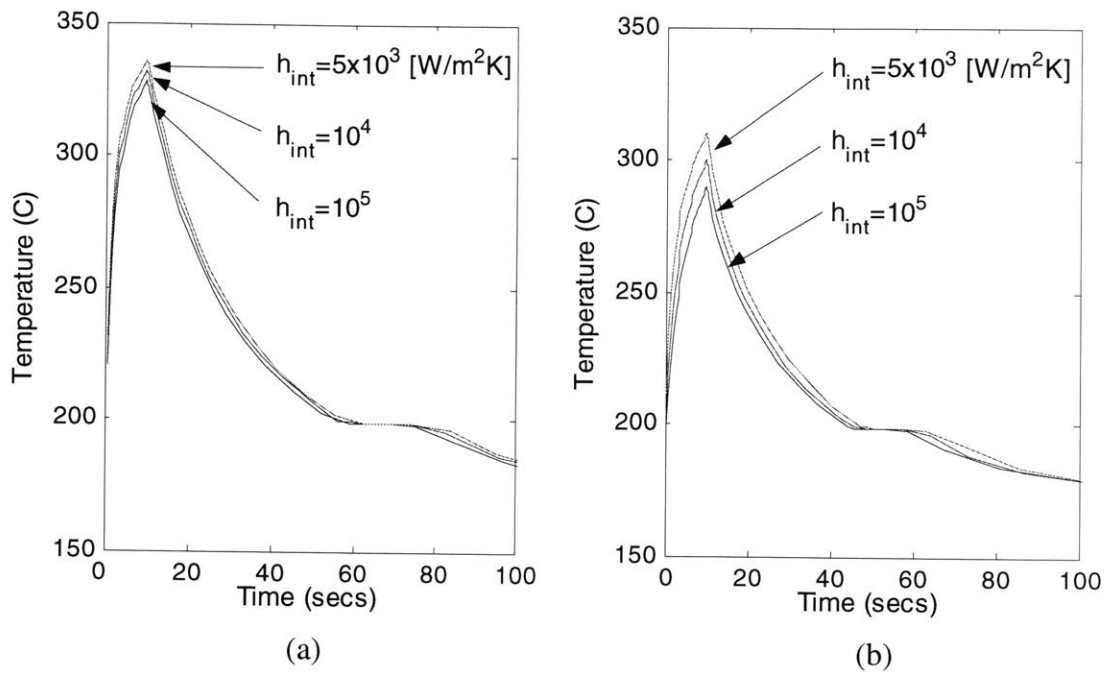
58

Figure 3.8. The effect of the interfacial heat transfer coefficient between the deposit and (a) a glass substrate, and (b) a titanium substrate in the 1-D model.

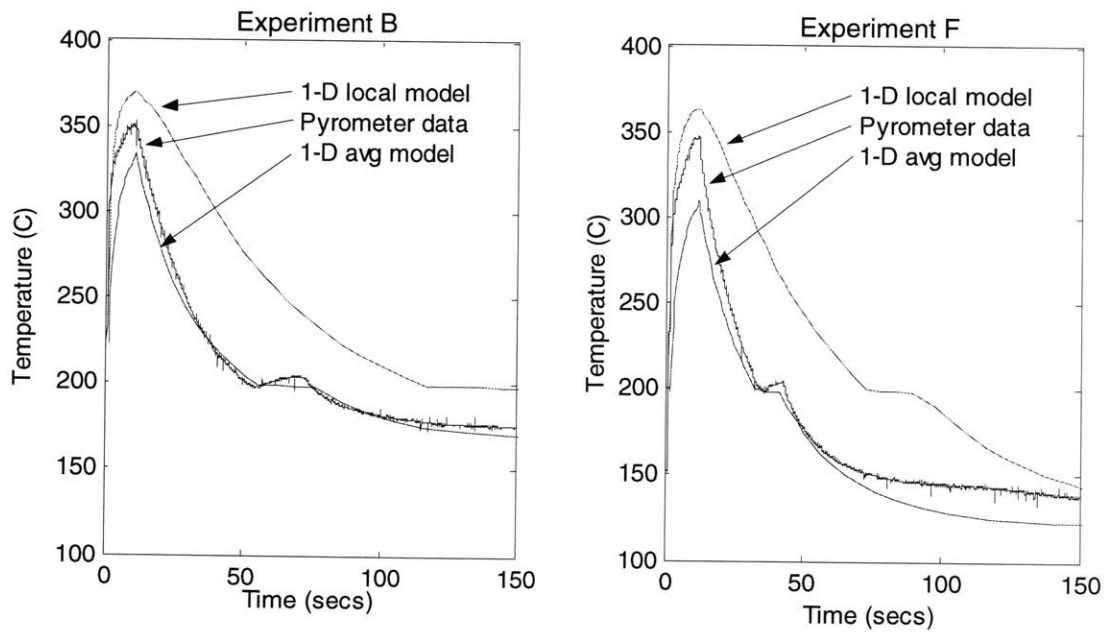Figure 3.9. Comparison of 1-D simulation results using an average and local growth rate to the deposit surface temperature measured by the pyrometer in Experiments B and F, which were sprayed onto glass substrates at 160°C and 120°C, respectively.

Figure 3.10. Comparison of 1-D simulation results using an average and local growth rate to the deposit surface temperature measured by the pyrometer in Experiments H and K, which were sprayed onto titanium substrates at 175°C and 125°C, respectively.
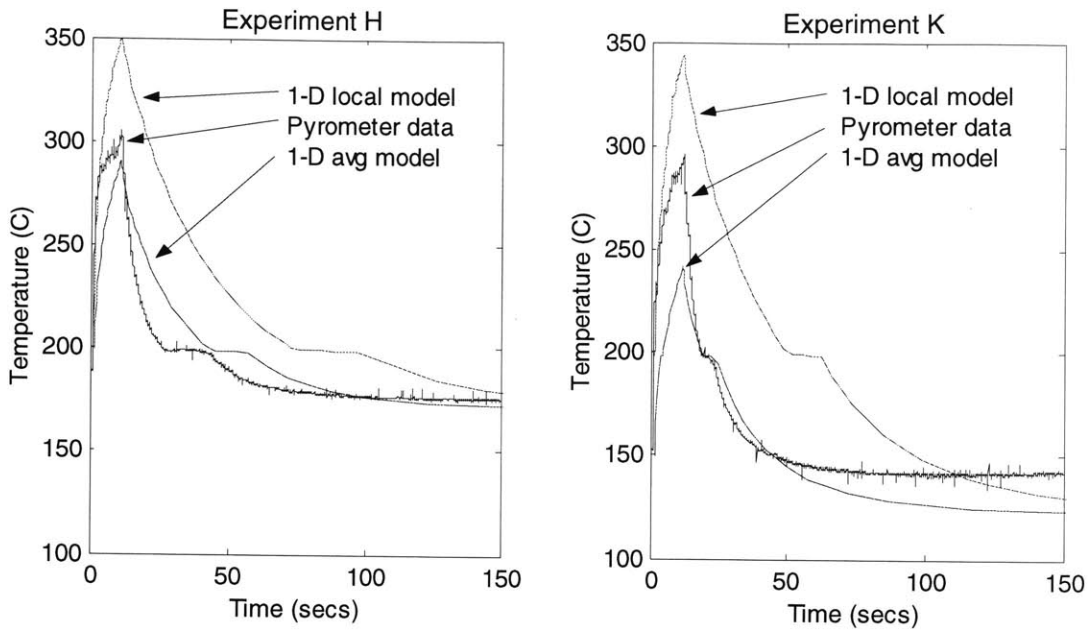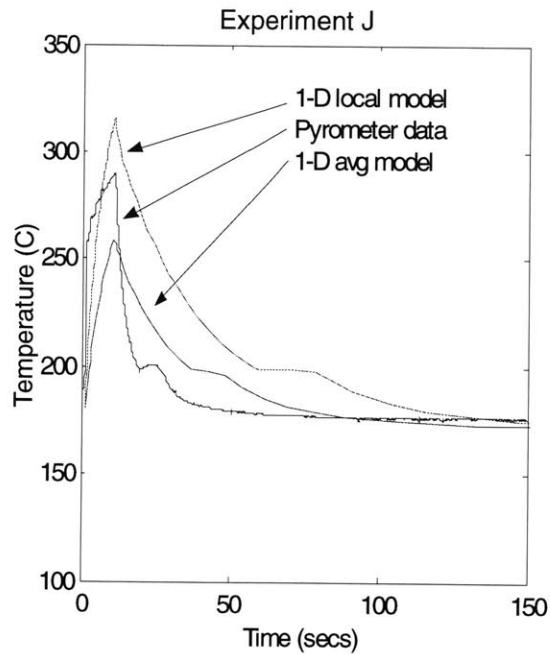

Figure 3.11. Comparison of 1-D simulation results using average and local growth rates to the surface temperature measured by the pyrometer in Experiment J, which was sprayed onto an aluminum substrate at 170°C.
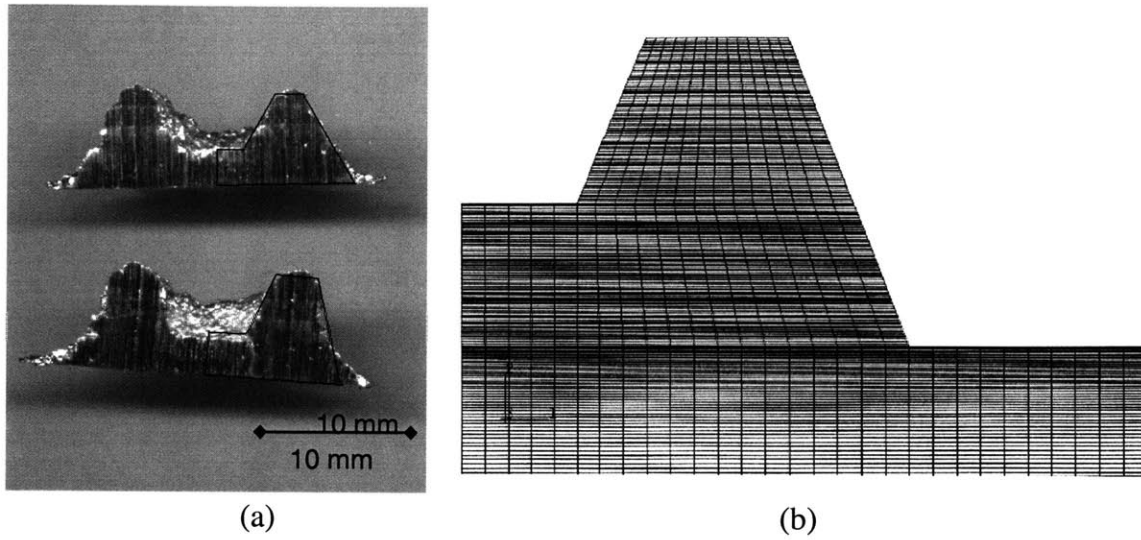
Figure 3.12. The geometries of (a) the actual sprayed deposits, and (b) the 2-D axisymmetric approximation with straight edges.
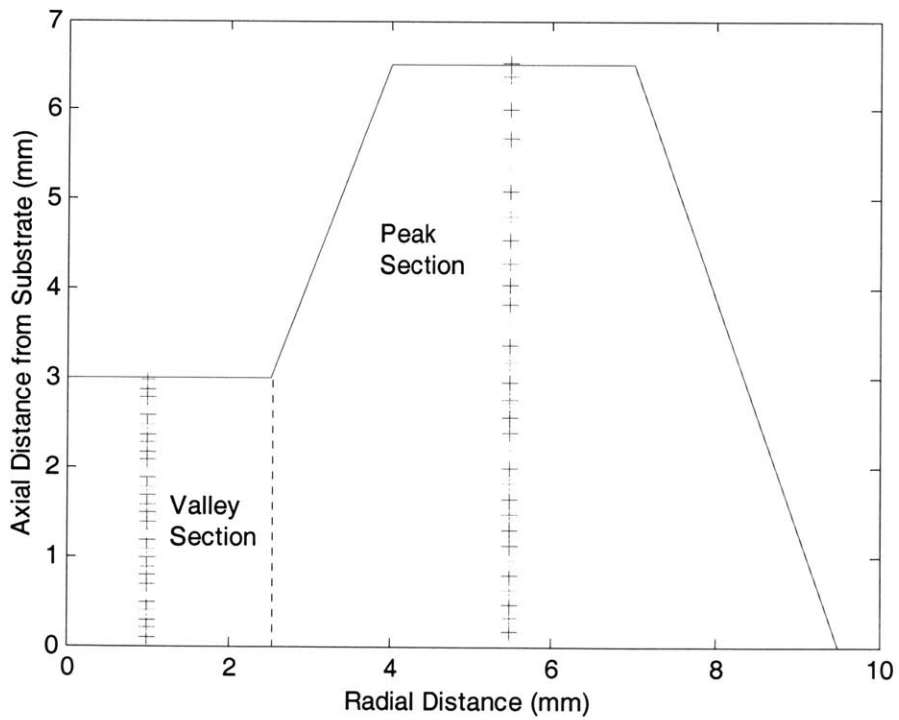
Figure 3.13. The incremental step thicknesses established for non-uniform mass flux in the 2-D axisymmetric model.
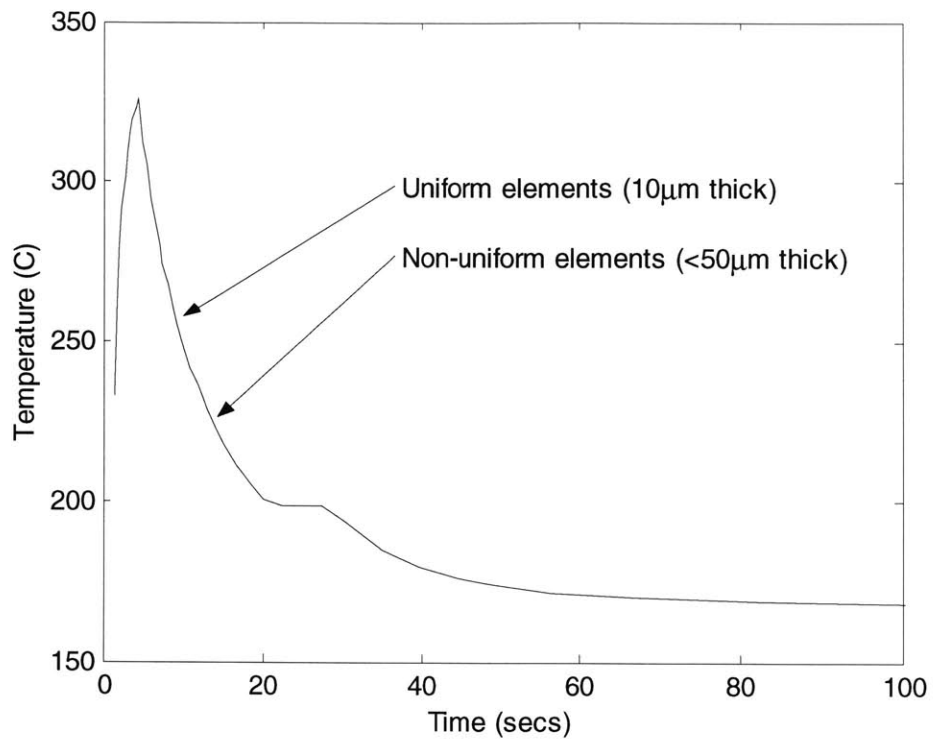
Figure 3.14. Deposit thermal history simulated by using non-uniform elements is equivalent to that simulated by using elements of uniform 10-μm thickness.
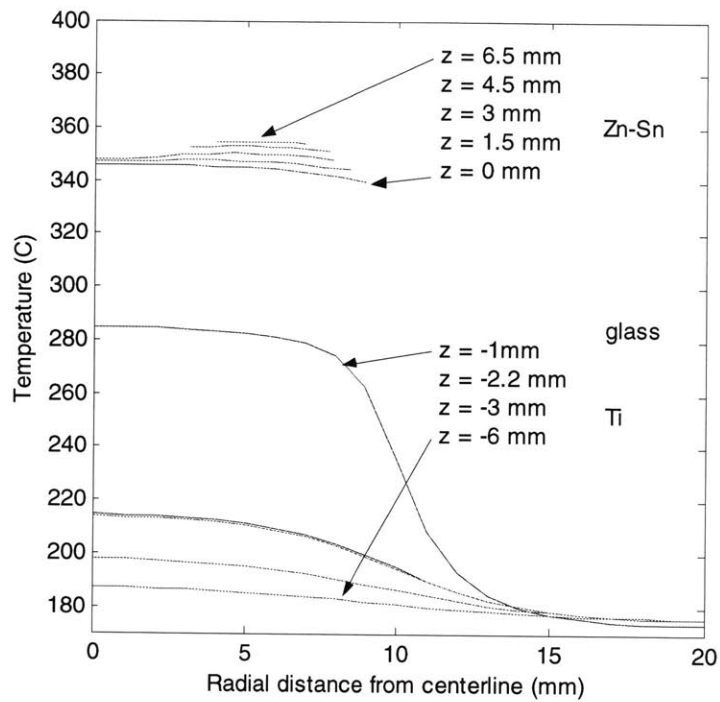
Figure 3.15. Thermal gradients within the Zn-20wt% Sn deposit and glass/titanium substrate immediately after deposition in Experiment B.
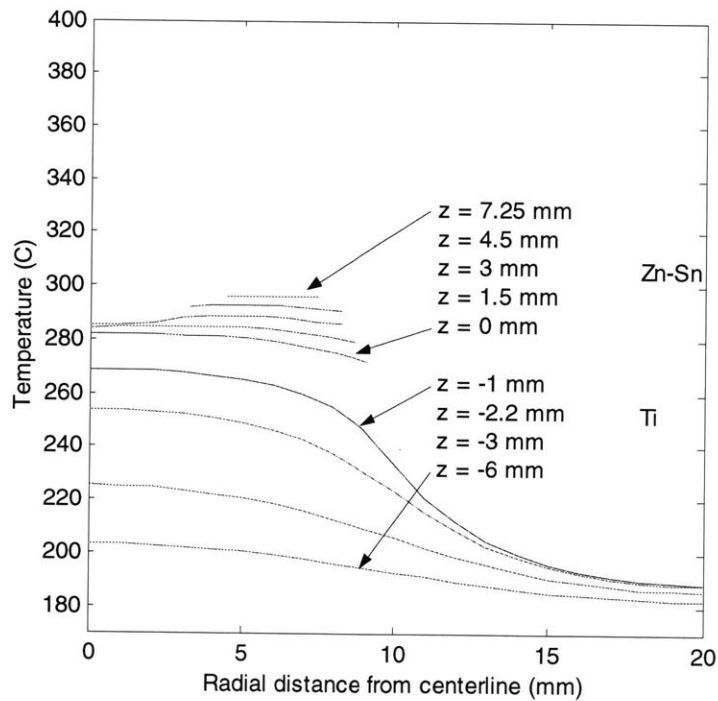
Figure 3.16. Thermal gradients within the Zn-20wt% Sn deposit and titanium substrate immediately after deposition in Experiment H.

63
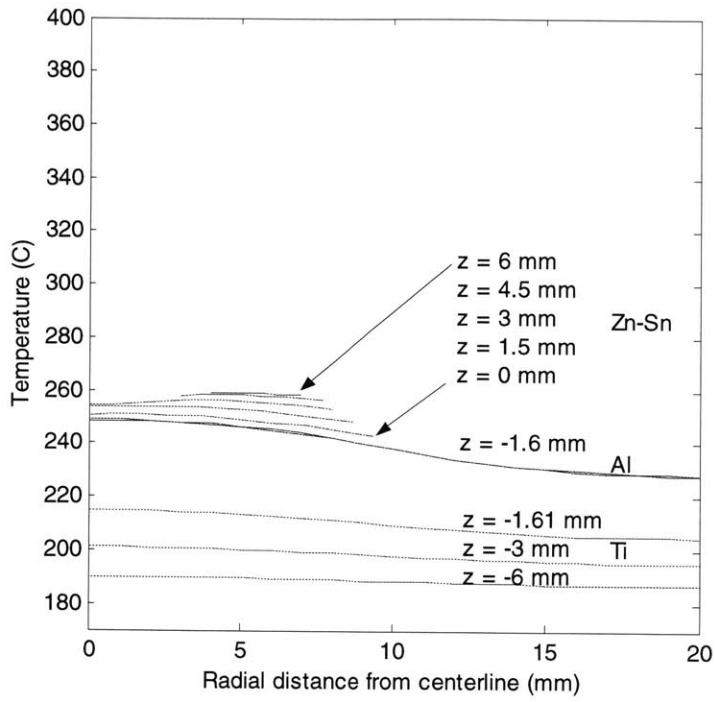
Figure 3.17. Thermal gradients within the Zn-20wt% Sn deposit and Al/paste/Ti substrate immediately after deposition in Experiment J.
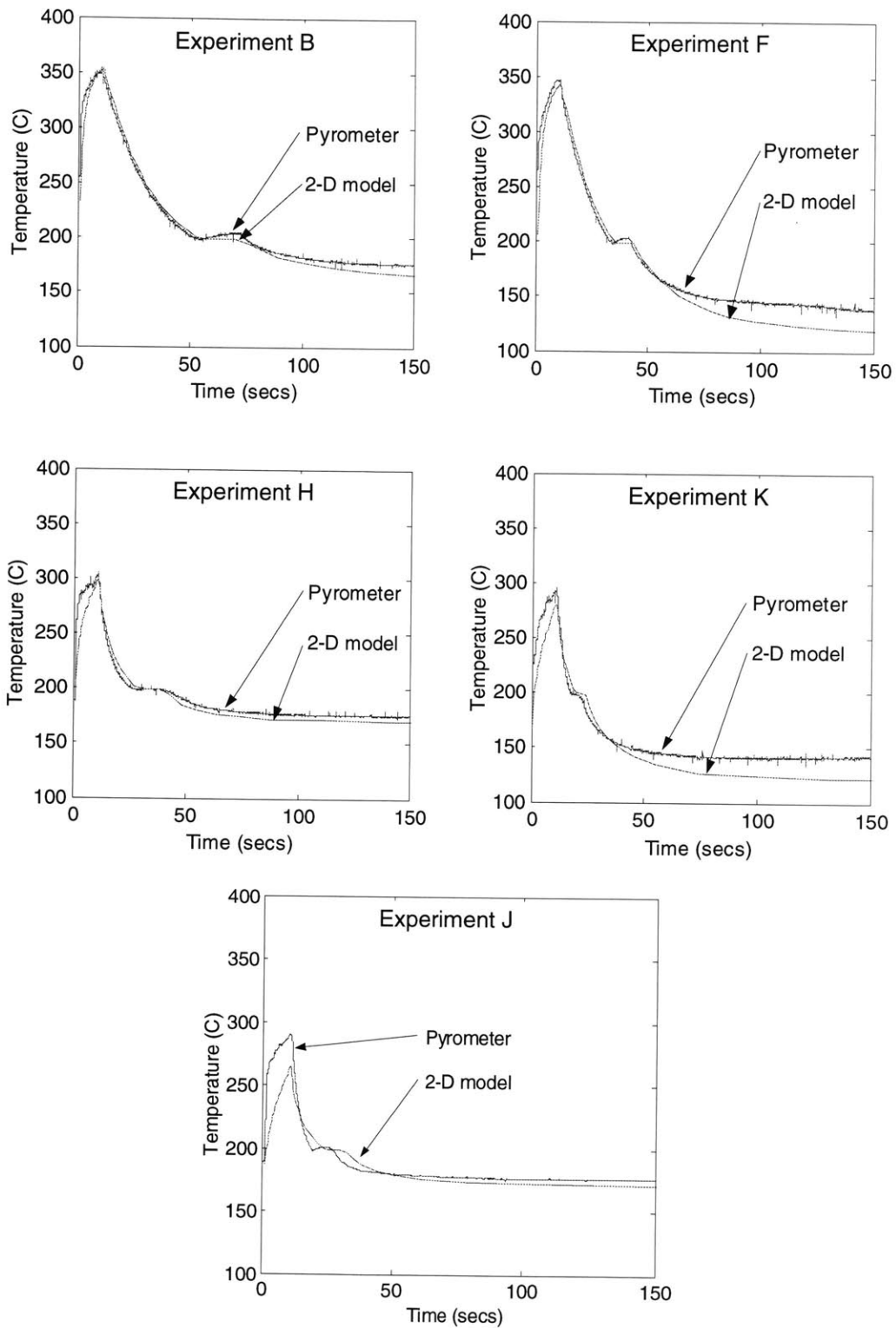
Figure 3.18. Comparison of the 2-D simulation results to the temperature curves measured by the pyrometer at the top surface of the deposit in Experiments B, F, H, J, and K.
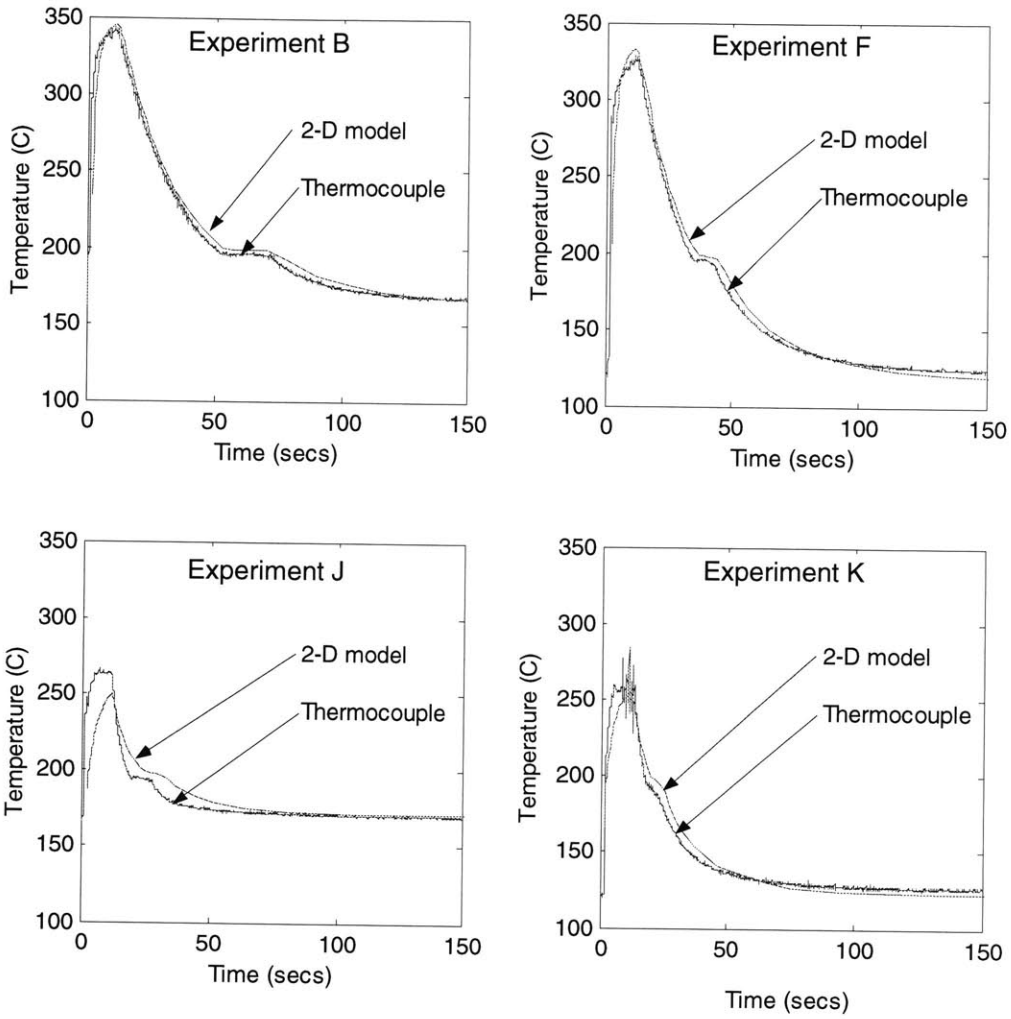
Figure 3.19. Comparison of the 2-D simulation results to the temperature curves measured by the thermocouple at the bottom surface of the deposit in Experiments B, F, J, and K.
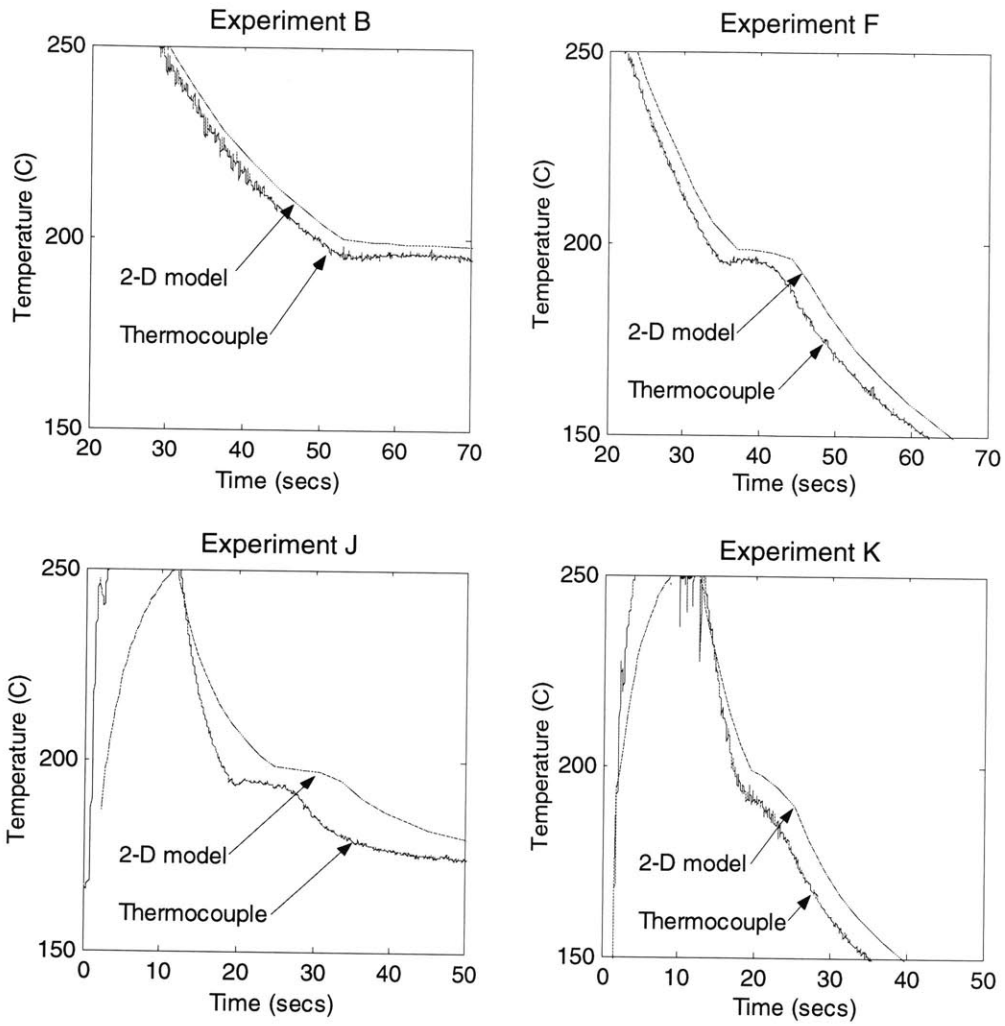
Figure 3.20. Comparison of the 2-D simulation results to the temperature curves measured by the thermocouple at the bottom surface of the deposit in Experiments B, F, J, and K (magnified).
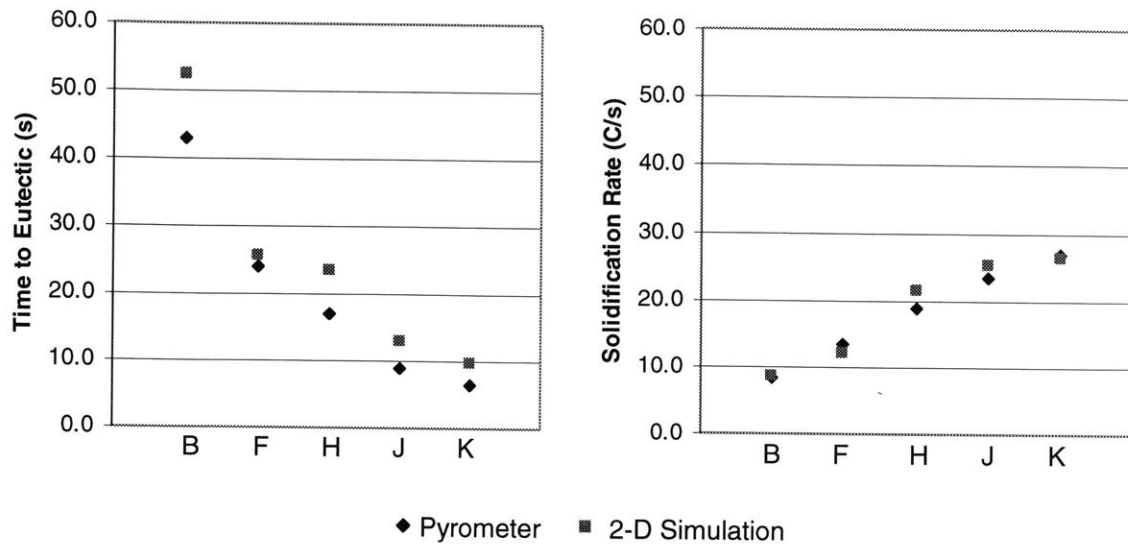
Figure 3.21. Comparison of metrics that characterize the droplet thermal history after deposition.

Chapter 4. DEPOSIT MICROSTRUCTURE

4.1 Introduction

The focus of this chapter is to measure the effects of deposit thermal history on microstructures produced by the UDS forming process with the Zn-20wt% Sn alloy. Although it is well known that increasing the solidification rate of a material will increase the refinement of its microstructure, it is useful to quantify this relationship for UDS process control. Furthermore, changes in the morphology, homogeneity, and phase segregation in the deposit microstructure are studied. This is accomplished by comparing the microstructures of deposits sprayed with different thermal histories, recorded in Chapter 2.

4.2 Kinetics of Particle Coarsening

In general, the morphology of solid particles, either dendrites or cells or grains, in a solid-liquid mixture evolves during solidification. The solid particles coarsen to reduce the interfacial free energy between themselves and the liquid matrix. Due to capillarity effects, particles with greater curvature have higher concentrations of solute in their neighboring liquid and thus, solute moves from small particles to large particles. This causes small particles to dissolve and the large particles to grow. The rate at which the solid particles coarsen can be limited by the kinetics of either solute diffusion through the liquid or solute absorption across the particle boundary.

Numerous empirical studies have been carried out to characterize particle coarsening in various solidification processes, including spray forming [Ashok 1993, Annavarapu and Doherty 1995, Underhill et al. 1995, Manson-Whitton et al. 1998, Fuxiao et al. 2001, Shukla et al. 2001]. For dendritic microstructures, different coarsening mechanisms have been observed, such as the melting of smaller dendrite arms either at their tips or their roots or cylindrical surfaces, thickening of larger dendrite arms, and coalescence of adjacent dendrite arms. For cellular microstructures, similar solution-reprecipitation and coalescence mechanisms occur between solid grains or cells. All studies report that the dendrite arm spacing or particle size increases with solidification time. These observations have led to a power-law relationship between the particle size or spacing, λ, and the local solidification time, t_f:

$$\lambda = K t_f^{\ n} \tag{4.1}$$

where K is the coarsening rate constant and n is the coarsening exponent whose value typically varies between 1/2 and 1/3. Alternatively, the particle size may be given in terms of the solidification rate, ε, which is inversely related to t_f. Thus, Equation 4.1 can be rewritten as:

$$\lambda = K \varepsilon^{-n} \tag{4.2}$$

Based on simple particle geometry and other assumptions, such as low volume fractions of the solid phase, constant temperature, and usually only one mode of coarsening, analytical models have been developed to predict the final particle size after solidification [Kirkwood 1985, Mortensen 1991, Kattamis and Voorhees 2001]. Most models assume that coarsening is controlled by diffusion through the liquid matrix and as a result, the coarsening exponent is typically equal to 3.

However, the cubic kinetic relationship only applies when there is a low fraction of solid in the mixture. At greater solid fractions, coarsening is interface-controlled, such as in grain boundary migration, resulting in a linear relationship between the square of the mean particle size and time [Mortensen 1989, Annavarapu and Doherty 1995, Okamoto and Kishitake 1975]. However, limited agreement between simulation and experimental results has been reported. For example, isothermal annealing experiments performed with spray formed materials have derived coarsening rate constants that are significantly lower than those reported in casting for similar alloys [Annavarapu and Doherty 1995, Manson-Whitton et al. 1998]. Therefore, empirical data that correlate particle size to solidification rate or time provide a valuable source of information for process control.

4.3 Deposition Experiments

As described in Chapter 2, Zn-20wt% Sn alloy droplets were sprayed with varying process parameters to produce deposits with different thermal histories. Droplet temperature and spray flux were varied to change the rate of heat input. Substrate material and temperature were varied to change the rate of heat extraction. The temperature of the deposit was measured *in situ* by a thermocouple and infrared temperature sensor. From the acquired temperature data, three metrics are used to described the deposit thermal history: the solid fraction in the deposit just prior to solidification, the solidification rate of the deposit immediately after deposition, and the solidification time required for the deposit to reach the eutectic temperature after deposition. The metrics were determined for each deposit and are listed in Table 2.3.

To investigate the effects of these metrics on deposit microstructure, a metallographic study was performed on samples obtained from the deposition experiments. Each deposit was removed from the substrate and cut in half, perpendicular to the bottom surface, as shown in Figure 3.8. The deposit sections were mounted in low-viscosity epoxy and polished to remove deformation and reveal microstructure. After grinding with 320, 600, and 800 grit silicon carbide papers, fine polishing was obtained with a 3-μm diamond suspension and then a 0.05-μm alumina suspension. Carbon sputter coating is applied on the polished surfaces for scanning electron microscopy (SEM) analysis of the microstructures. Backscattered electron imaging was used to observe the morphology of the microstructure. Furthermore, wavelength dispersive spectrometry (WDS) was used for composition element analysis of solute segregation.

4.4 Resultant Deposit Microstructure

Figures 4.1 and 4.2 show the micrographs of each deposit cross-section taken at the same magnification near the location of the pyrometer temperature measurement. The microstructures are compared to determine the effects of deposit thermal history on several aspects, including morphology, characteristic feature size, homogeneity, and phase segregation.

4.4.1 Morphology

In general, the microstructure of the as-sprayed Zn-20wt%Sn deposits consists of fine Zn-rich cells surrounded by a continuous Sn-rich matrix. Within each deposit, the cells have a wide distribution of size and shape. The smallest grains are spherical and about 2 μm in diameter, whereas the largest grains are oblong and about 15-μm wide and 110-μm long.

At lower magnification, Figure 4.3 shows that there are regions within the deposit microstructure where long slender cells appear to grow radially outward from a common nucleation center. The cells are most likely precursors to dendrites that grow in the opposite direction of heat flow. These clusters are found throughout the deposit cross-sections and are believed to represent phases that solidified in the droplet during flight, before impinging on the substrate or deposit surface. Further evidence for the nucleation of cell clusters in the droplets is given in the next section. Although the boundaries of the deformed droplets do not always remain intact, the existence of the cell clusters implies that the deposit microstructure includes a mixture of microstructures stemming from discrete droplets.

Between the clusters, the cells are typically more spherical and randomly oriented. Furthermore, these boundary cells are less densely packed than the cell clusters inside the Sn-rich matrix. This is consistent with the hypothesis that the boundary cells were initially liquid in the droplet before impact and thus, they have a greater concentration of neighboring solute. In some cases, the

71

boundary cells appear to grow parallel to each other as shown in Experiment H in Figure 4.2. This feature is likely the result of epitaxial growth across splat boundaries in the remaining liquid on the deposit surface.

For deposits that experience faster cooling rate, a different type of cell morphology was observed in addition to the cell clusters in the microstructure. Figure 4.4 shows the microstructure of deposit K at higher resolution and it reveals dark Zn-rich cells that have Sn-rich particles trapped inside. One explanation for this feature is that it is the result of incomplete coalescence of fine-scale Zn cells. If the liquid film that initially separates the cells becomes very thin, it is possible that surface tension causes the liquid to contract, resulting in direct contact between the cells. The cells continue to agglomerate while trapping the solute inside. If the solidification rate is slow enough, then the solute will eventually diffuse out of the Zn-phase. However, since the cooling rate of deposit K is relatively fast, it completes solidification before the solute can escape. This may also explain why the microstructures of deposits with slower cooling rates, below 13°C/s, do not exhibit a high population of the semi-coalesced cells.

4.4.2 Characteristic Feature Size

Although each deposit microstructure exhibits a wide distribution of cell sizes, it is noticeable in Fig. 4.1 and Fig. 4.2 that the microstructures have varying degrees of refinement from experiment to experiment. To study the effect of deposit thermal history on the scale of the deposit microstructure produced by UDS forming, it is necessary to quantify a characteristic feature size. A characteristic feature that is common to all the deposit microstructures is the cell clusters described above. Therefore, the cell spacing of this characteristic feature is used to represent the degree of microstructural refinement achieved in the deposit microstructure. The cell spacing is measured by using the lineal intercept method with a line drawn perpendicular to the direction of cell growth. The resolution of the measurement is limited by the total size of the cell cluster, and is typically less than 10% of the average cell spacing.

Several clusters in each deposit microstructure were measured near the location of the pyrometer temperature measurement. The average cell spacing as well as the maximum and minimum cell spacing for each deposition experiment are tabulated in Table 4.1. To determine the time dependence of the microstructure refinement, cell spacing is plotted against the deposit solidification rate. As shown in Figure 4.5, the correlation between solidification rate and cell spacing is found to be:

$$\lambda = 27.1\varepsilon^{-0.52} \tag{4.3}$$

For comparison, Figure 4.6 shows the cell spacing plotted against the deposit solidification

times. Once again, a line is best fit to the logarithm of the experimental data. The relationship between solidification time and cell spacing is found to be:

$$\lambda = 1.9 t_f^{0.43} \tag{4.4}$$

Although the deposit solid fraction prior to solidification did not vary significantly among the deposition experiments, this metric is plotted against the characteristic feature size as well. Figure 4.7 shows that feature size generally increases as the deposit solid fraction increases.

4.4.3 Homogeneity

The microstructure was examined at several locations in the deposit cross-section to determine its uniformity. The periphery at the base of the deposit was avoided since the low mass flux in this region creates significant porosity. Figure 4.8 shows the micrographs and their respective locations at which they were taken in deposit A. Despite the non-uniform mass flux distribution across the deposit, the microstructure in the peak section closely resembles the microstructure in the valley section in deposit A. In addition, the deposit microstructure does not change significantly from the base of the deposit near the substrate to the top of the deposit. Uniform microstructure across the deposit was found in all deposits except in Experiments C and D, which exhibited porosity.

Figure 4.9 shows the micrographs taken in the top, middle and bottom regions of the deposit cross-section in deposits C and D. In these samples, porosity is most significant at the deposit bottom and decreases as the deposit height increases. Deposit C exhibited porosity only near the substrate interface, where as deposit D showed porosity throughout its thickness. The factors that may have led to the formation of porosity in deposits C and D are discussed later in Section 4.5.

Despite the porosity, the microstructure of these deposits exhibits similar features, such as the cell clusters, found in the other deposits. Furthermore, the microstructure at the base of deposit D confirms that the cell clusters do indeed nucleate inside individual droplets prior to impact. This is based on observing how the cell clusters are located within individual splats and how they appear to control the amount of droplet deformation. When the droplets impact the substrate, the high volume of pre-solidified phases prevents significant deformation such that only the solute-rich liquid is capable of motion. Therefore, the solute-rich regions are concentrated at the splat boundaries where the remaining liquid wets neighboring splats.

As the deposit grows, its surface temperature increases and the mass flux of the spray increases. Thus, there is greater mixing of the pre-solidified phases that impact the deposit surface. As a

73

result, solute segregation and porosity decrease as the deposit height increases.

4.4.4 Segregation

To determine whether the deposit solidification rate affects microsegregation, compositional analysis was performed on deposits B and H with wavelength dispersive spectroscopy. The probe, which measured a 100-μm^2 area using 300 na of current, was focused on the Zn-rich phase to detect the weight percent of Sn solute at several locations in both samples with 0.01% accuracy. The equilibrium concentration of Sn in solid Zn is reported by the phase diagram to be less than 0.001 wt%.

In deposit B, the weight percent of Sn inside Zn-rich cells was measured to range from 0.17% Sn to 0.24% Sn. There was no apparent correlation between the solute percent and measurement location. Likewise, in deposit H, the weight percent of Sn was measured to range from 0.15% Sn to 0.35% Sn. On average, deposit H, which cooled more than two times faster than deposit B, shows greater solubility for Sn. This trend agrees with widely reported evidence of increased solid solubility in rapidly solidified materials.

On a larger scale, much greater amounts of solute are found as discrete precipitates within the Zn-rich cells, as shown previously in Figure 4.4. Here, the area fraction of the Sn-rich phase inside the Zn cell can be as high as 17%. This type of solute segregation was found only in the microstructures of deposits that experience faster solidification rates. One possible explanation is that the cells were in the process of coalescing during solidification. And, the faster solidification rate prevents the solute from diffusing out of the Zn-phase, thereby increasing the apparent solid solubility of Sn in Zn.

Furthermore, macrosegregation of the solute is observed at splat boundaries of porous deposits. As discussed previously, deposits C and D exhibit large-scale porosity and significant solute concentration at splat boundaries. In this case, the deposit cooling rate cannot fully explain the occurrence of macrosegregation since deposits C and D have neither the slowest nor the fastest cooling rates. Rather, deposits C and D were created with droplets that have the greatest solid fraction before impact. It is possible that the high solid fraction in the droplets and on the deposit surface prevents complete mixing of solid and liquid phases. Therefore, the solute-rich liquid will flow to and remain in the contact area between splats since this is a location of lowest surface energy.

4.5 Porosity Formation

Although porosity formation is outside the scope of this study, it is interesting to consider what

factors might have led to the large-scale porosity observed in deposits C and D. First of all, the recorded temperature data of these deposits makes it apparent that controlling the deposit thermal state alone is not enough to prevent porosity. For example, even though the surface temperature of deposit D is measured to be greater than that of deposits H, I, J, and K, the latter deposits do not exhibit porosity. This implies that porosity formation depends on the droplet thermal state and velocity upon impact as well the deposit thermal state.

As shown in Table 2.2, smaller diameter droplets were used in Experiments C and D in order to decrease the heat flux of the spray without decreasing the mass flux. Thus, the droplets in Experiments C and D have the lowest liquid fractions compared to the other experiments. Increasing the droplet solid fraction affects the consolidation of splats by decreasing the amount of splat deformation. The deposit microstructure in Figure 4.9 shows how the splats do not have enough liquid to flow around splat boundaries and hence, large voids are created. As the deposit height increases during deposition, there is less porosity observed in deposit C. This is mostly likely due to an increase in the liquid fraction on the deposit surface, which may be sufficient to fill in voids created by the splats. However, it is difficult to determine whether the greater mass flux arriving at top of the deposit plays a separate role in decreasing the deposit porosity.

Deposit D showed porosity throughout its thickness, which implies that the deposit thermal state requires significantly more liquid content to overcome the lack of droplet spreading, associated with the current droplet thermal state. However, a systematic study on the combined effect of droplet and deposit thermal states is necessary to reveal the conditions that prevent porosity formation.

4.6 Discussion

By analyzing the microstructure of deposits that were produced with various solidification conditions, it was possible to reveal several insights to the evolution of the deposit microstructure. First, it was observed that the deposit microstructure includes a mixture of solidified phases formed inside the droplets before impact with the deposit. The solid phases manifested themselves as clusters of cells that grow radially outward from a common nucleation center. During solidification, it appears that the cells coarsen by coalescence, which is arrested in deposits with higher cooling rates.

Several factors were considered to control the rate of coarsening in the deposit microstructure. The characteristic feature size was found to vary inversely with the square root of the solidification rate. This parabolic growth rate suggests that coarsening is interface-controlled, which is probably due to the low volume fraction of liquid in the deposit during deposition. Nonetheless, the effect of deposit solidification time did not exhibit the expected quadratic

relationship with the characteristic feature size. This is mostly likely due to the fact that the solidification rate of the deposit is not constant over time. Furthermore, comparing Figs. 4.5 and 4.6 shows that the final cell spacing has a better correlation with solidification rate than solidification time. Although the deposit solid fraction immediately after deposition varied from 63% to 75%, there is no evidence to suggest that it has an independent effect on the deposit microstructure.

The small variation in characteristic feature size within the deposit microstructure suggests that the cooling rate experienced by the individual droplet layers upon impact plays a minor role in determining the final feature size. Using the 2-D thermal model, the cooling rate of the droplet layer upon impact with the deposit is calculated at several different deposit heights. For the spray conditions in Experiment B, the local cooling rate was found to decrease from 1500°C/s to 110°C/s during deposition. If the rapid cooling rate of the droplet material during deposition were to dominate the final deposit microstructure, one would expect to see a much larger variation in feature size through the deposit. However, this is not the case because of the much slower cooling rate after deposition. Equation 4.2 shows that the change in particle size is more significant at lower coolin rates. Furthermore, the local cooling rate was measured at the top and bottom surface of the deposit after deposition to be 6.1°C/s and 5.1°C/s, respectively. Therefore, the microstructural homogeneity of the sprayed deposits is controlled by the local cooling rate after deposition.

Regarding segregation, the Zn-rich cells were measured to have greater concentrations of Sn-solute than the equilibrium phase diagram predicts. However, porosity formation can reverse the positive effects of rapid cooling on microsegregation. For example, deposits that exhibited large-scale porosity also showed regions of high solute concentration, or macrosegregation. If there is not enough mixing of solid and liquid phases on the deposit surface, then segregation will increase. However, a systematic study on the combined effect of droplet and deposit thermal states is necessary to reveal the conditions that would prevent porosity formation.
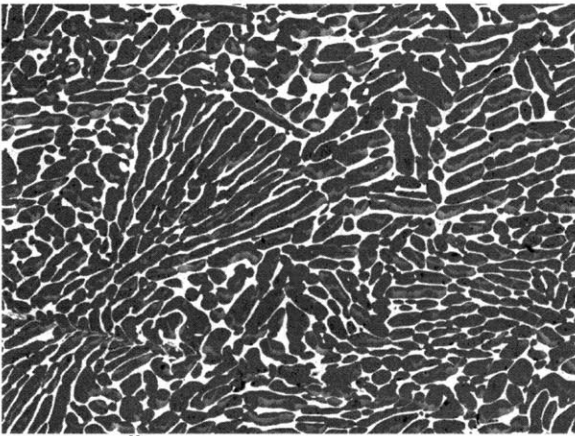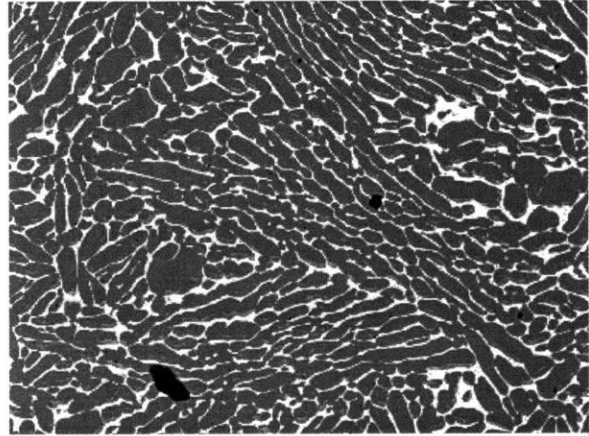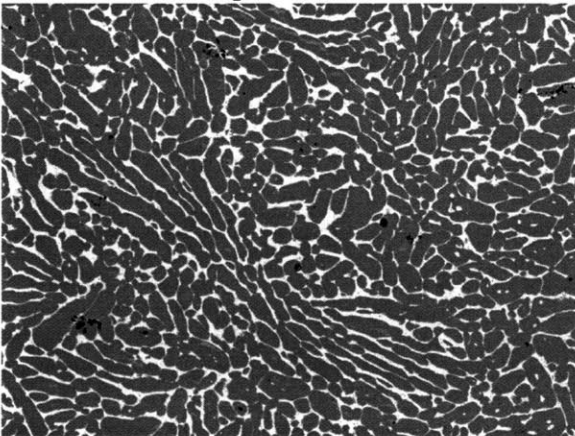
Experiment A
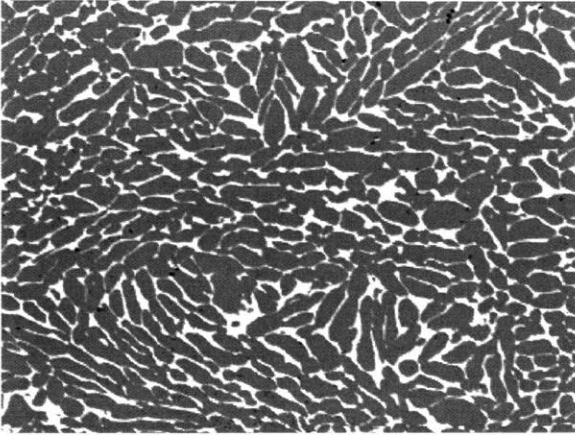
Experiment B
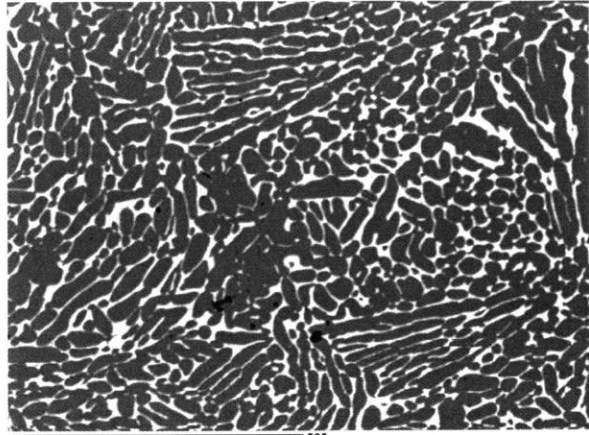
Experiment C

Experiment D

Experiment E

Experiment F

100 μm

Figure 4.1. Deposit microstructures of Experiments A through F observed near the location of the pyrometer measurement.
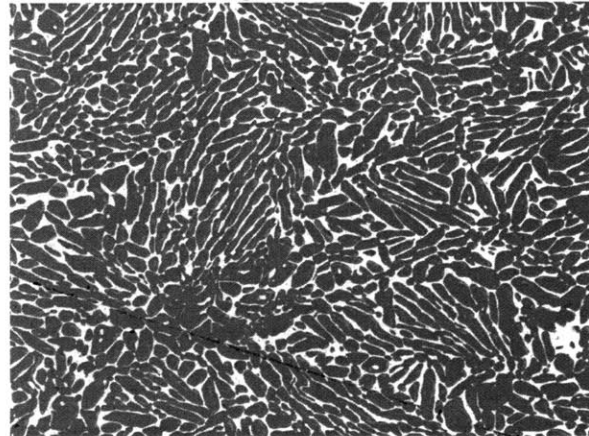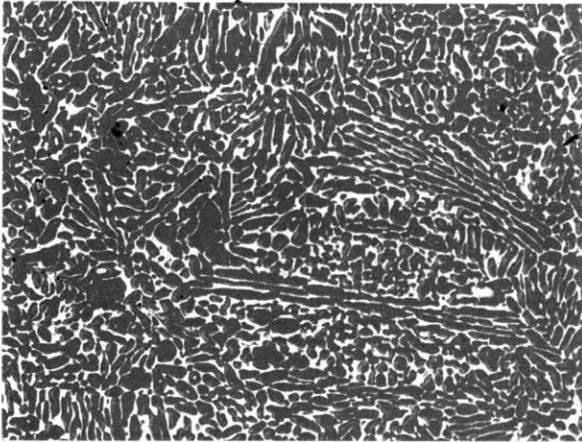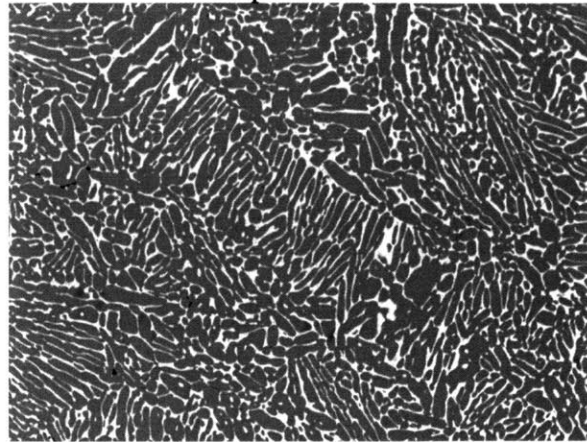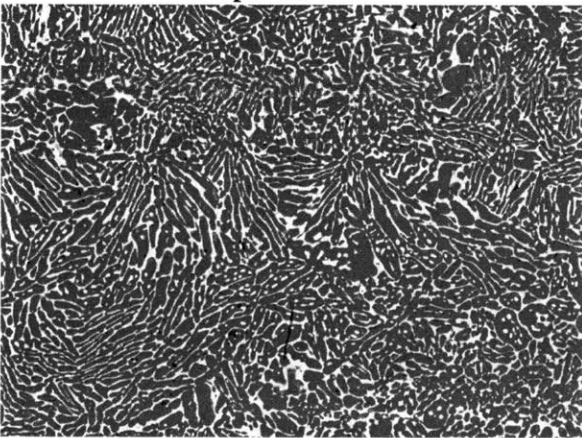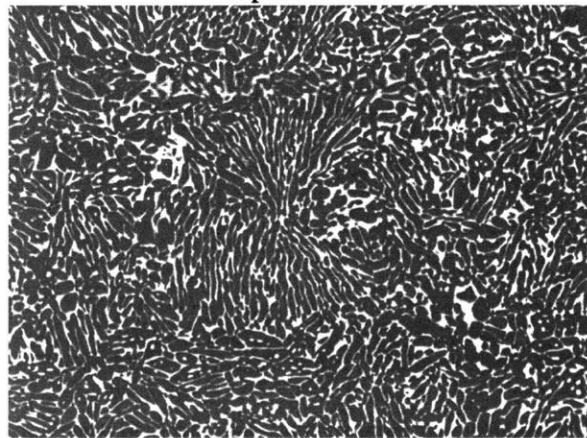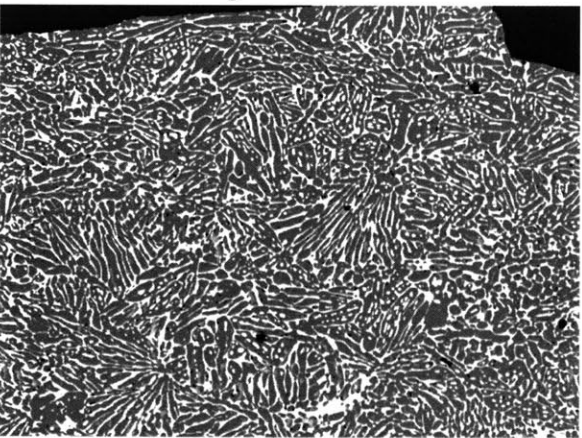
Experiment G

Experiment H

Experiment I

Experiment J

Experiment K

100 µm

Figure 4.2. Deposit microstructures of Experiments G through K observed near the location of the pyrometer measurement.
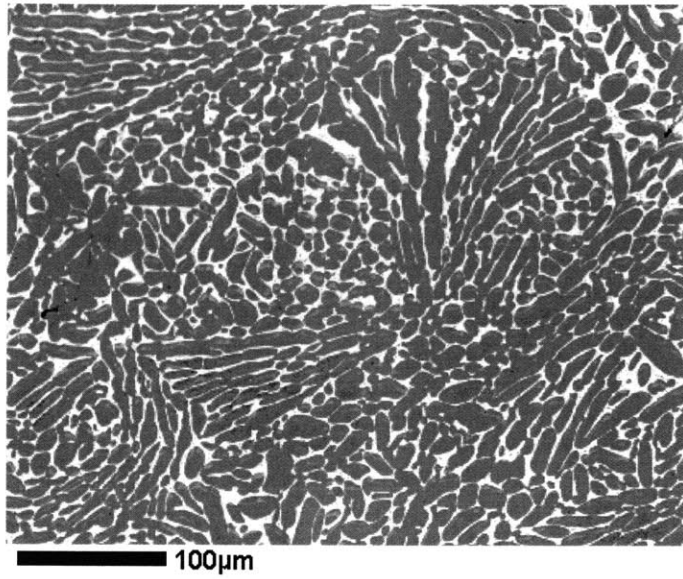
Figure 4.3. Cell cluster shown in deposit microstructure of Experiment B.
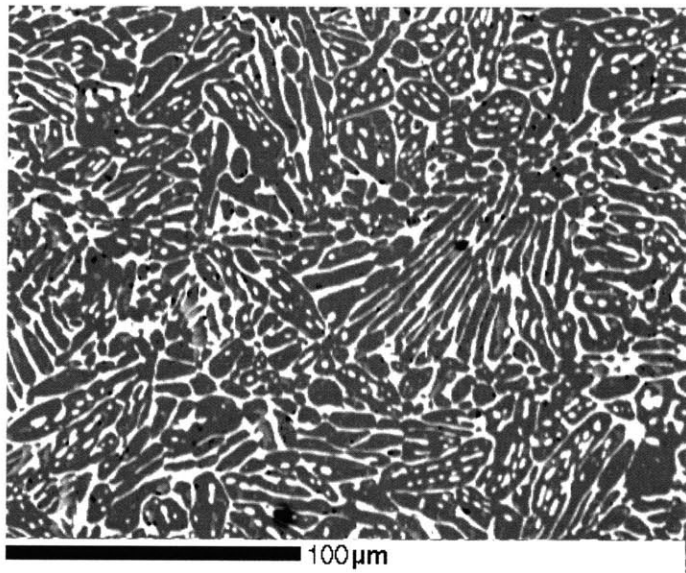
Figure 4.4. Arrested coalescence in deposit microstructure of Experiment K.

Table 4.1. Measured characteristic feature size in deposit microstructures.

	A	B	C	D	E	F	G	H	I	J	K
dep solid frac [%]	63	63	65	68	66	65	68	71	75	74	73
time to eutectic [s]	45.0	43.0	41.0	38.0	30.0	24.0	21.0	17.0	12.0	9.0	7.0
initial solid rate [C/s]	6.1	8.3	6.5	6.3	13.9	13.4	14.3	18.9	19.2	23.3	27.0
avg feat size [μm]	10.4	9.5	11.0	10.0	8.3	7.1	6.8	6.1	5.7	5.2	4.9
min feat size [μm]	9.1	9.1	10.0	9.1	8.0	6.5	6.3	5.6	5.0	4.7	4.3
max feat size [μm]	11.1	11.1	12.5	12.5	9.1	7.5	7.1	7.1	6.2	5.7	5.6

$$\lambda = 27.1\varepsilon^{-0.52}$$
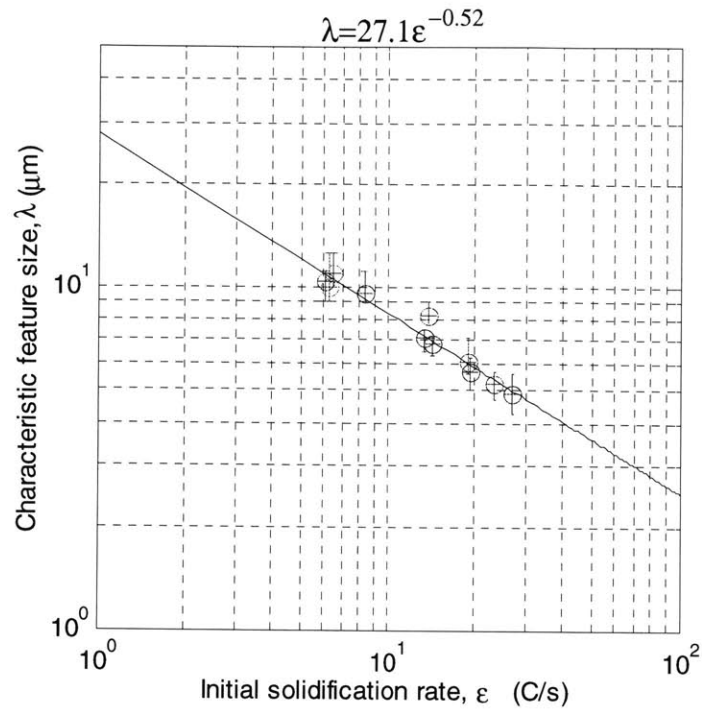
Figure 4.5. Relationship between the initial solidification rate of the deposit and the characteristic feature size of the microstructure.

$$\lambda = 1.9t_f^{0.43}$$
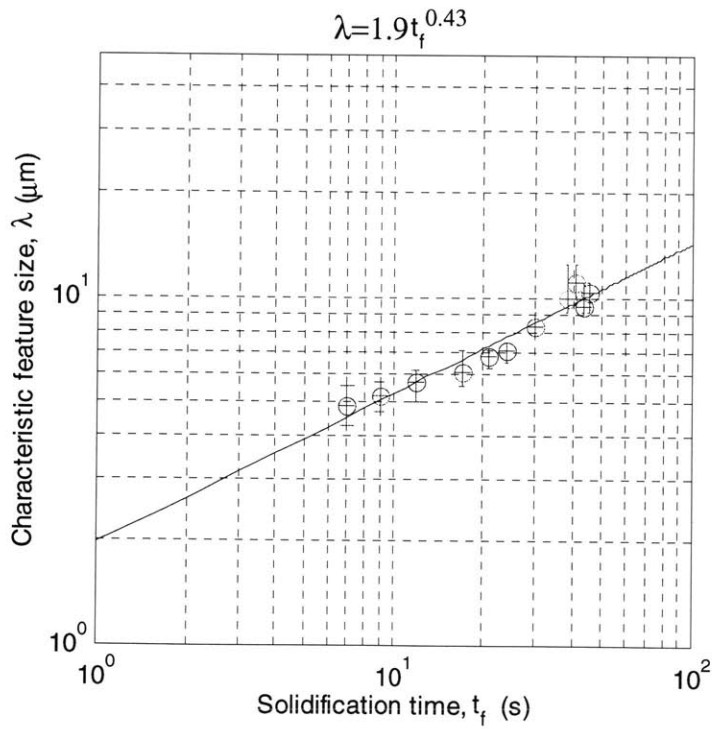
Figure 4.6. Relationship between the solidification time of the deposit and the characteristic feature size of the microstructure.

81

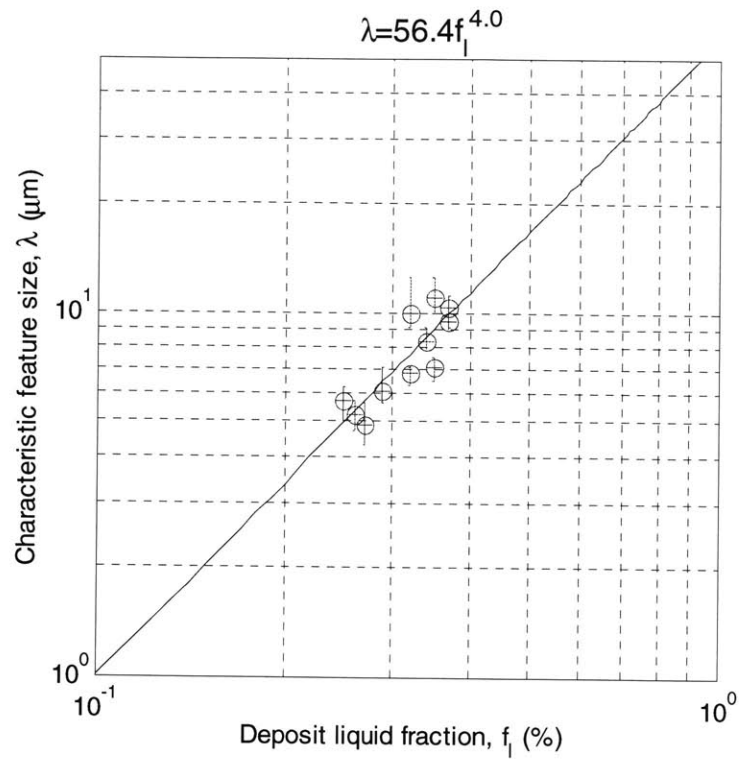Figure 4.7. Liquid fraction at the deposit surface versus characteristic feature size of the deposit microstructure.

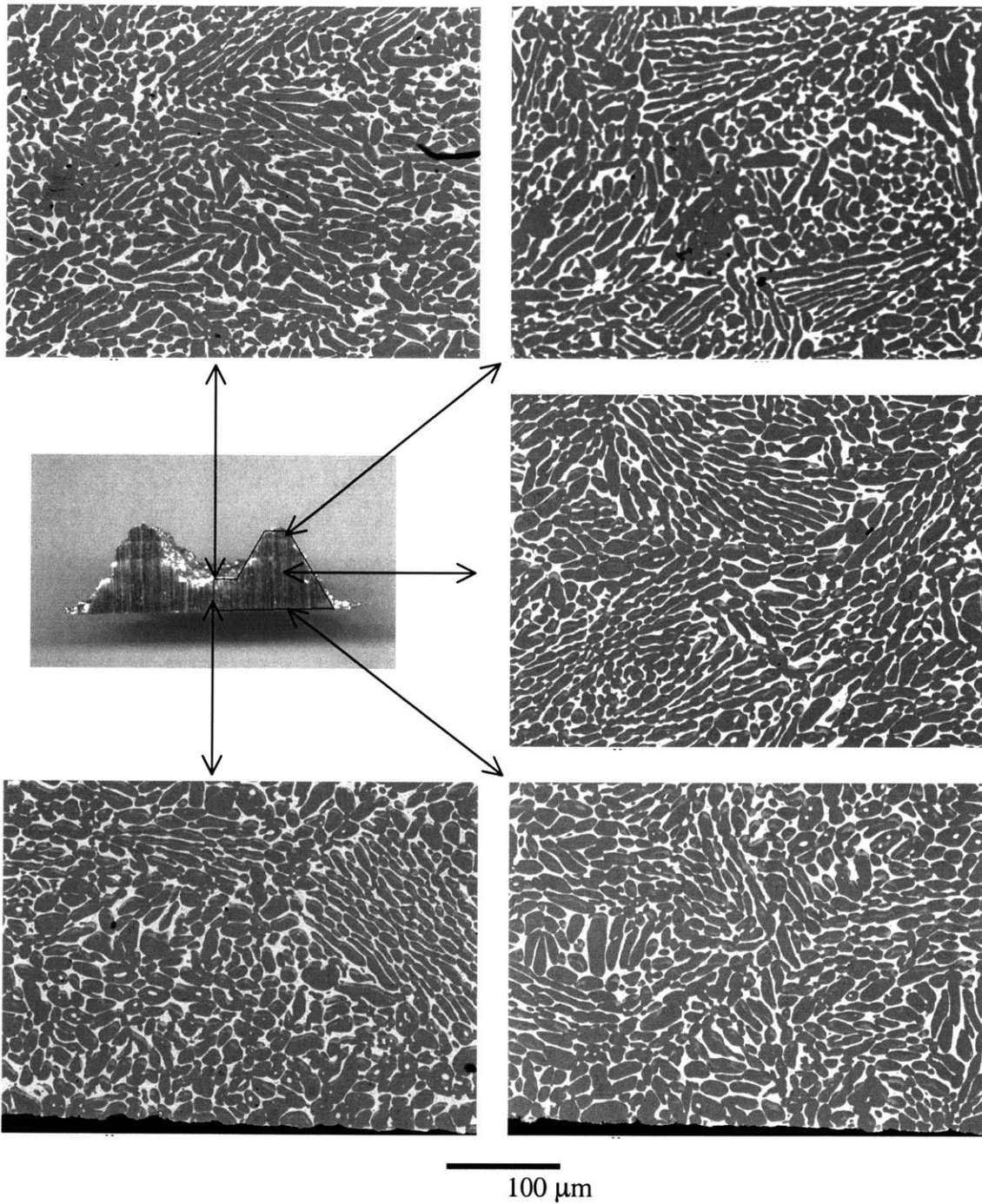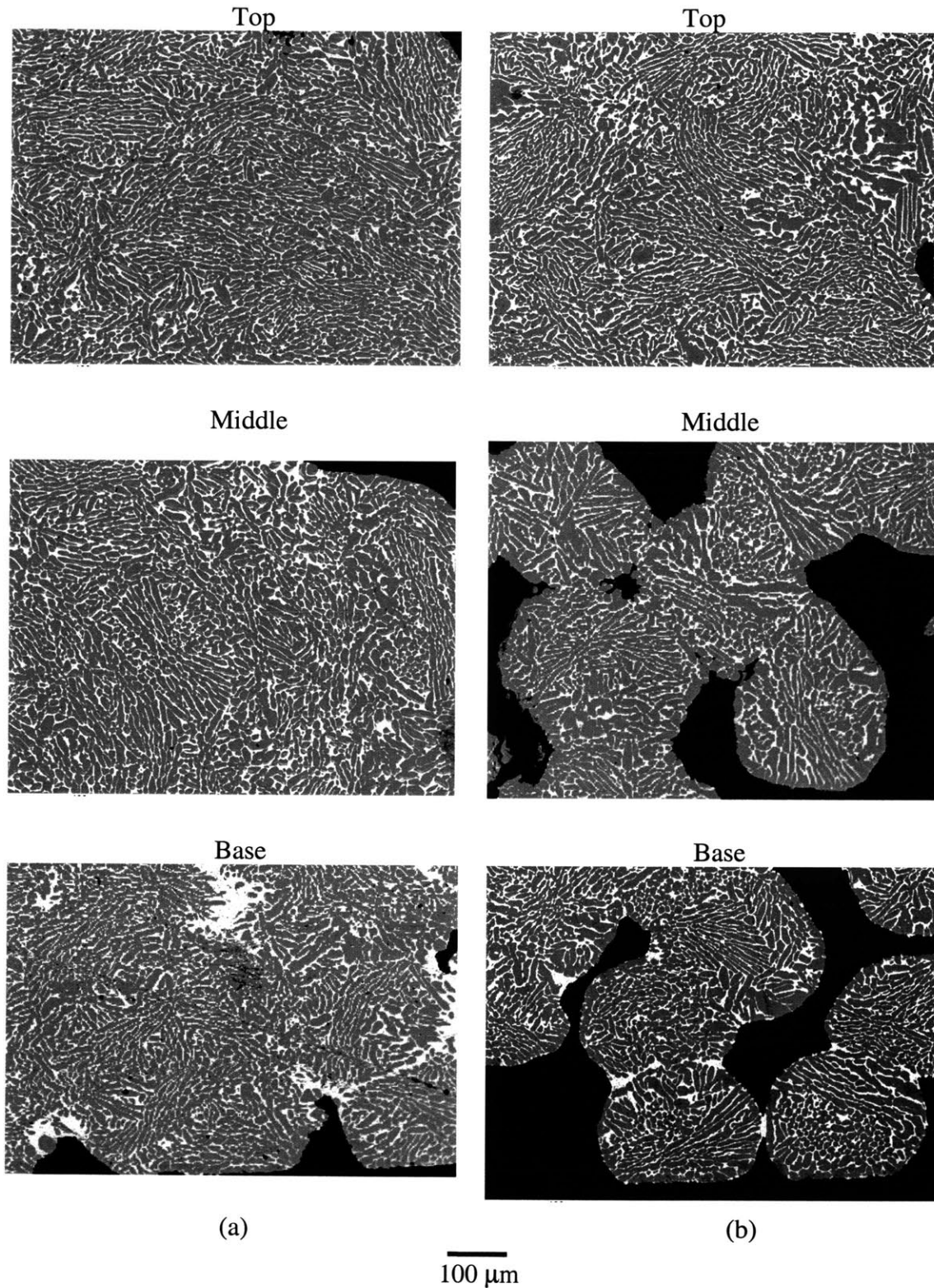Figure 4.8. Deposit microstructure at different locations in the deposit from Experiment B.

Top

Top

Middle

Middle

Base

Base

(a)

(b)

100 μm

Figure 4.9. Deposit microstructure at top, middle, and base of deposits in (a) Experiment C and (b) Experiment D.

Chapter 5. CONCLUSIONS

5.1 Summary

This thesis has investigated the effects of deposit thermal history on microstructure produced by uniform droplet spray forming. A series of experiments were conducted with Zn-20wt% Sn alloy droplets using different process parameters to vary the thermal history of the deposit. The deposit temperature at the top and bottom surface was measured *in situ* by using a fiber-optic infrared pyrometer and a thermocouple, respectively. The pyrometer output was calibrated to the emissivity of the deposit surface at the eutectic temperature plateau. The agreement between the temperature curves measured by the pyrometer and thermocouple shows that the pyrometer can accurately measure the deposit surface temperature during solidification.

The deposition experiments revealed that the deposit thermal history is more sensitive to the substrate conditions than the spray conditions. Furthermore, the cooling rate of the deposit is dominated by the heat conduction to the substrate. A finite element model was developed to predict the deposit thermal history. An 1-D heat conduction model was only capable of predicting the solidification time of deposits sprayed on glass substrates. However, when the thermal diffusivity of the substrate material is comparable to that of the deposit material, transverse conduction cannot be neglected. Using a 2-D axisymmetric approximation of the deposit, the model closely predicted the deposit thermal history in most cases.

In Experiments A through K, the solidification rate of the deposits immediately after deposition ranged from 6°C/s to 27°C/s, the deposit solidification times ranged from 9 s to 45 s, and the deposit solid fractions just prior to solidification ranged from 63% to 75%. The resultant deposit microstructures were examined with scanning electron microscopy, which revealed that the deposit microstructure includes solidified phases formed inside the droplets before impact. The coarsening kinetics of the characteristic feature size is best described by $\lambda = 27.1\varepsilon^{-0.52}$. This parabolic growth law implies that the coarsening of the microstructure is interface-controlled rather than diffusion-controlled, due to the high volume fraction of solid in the deposit during deposition. Furthermore, the homogeneity of the deposit microstructure across its thickness suggests that the rapid cooling rate of the individual droplet layers upon impact played a minor role in determining the final deposit microstructure. The deposits also exhibited increased solid solubility with faster solidification rates. However, porosity formation observed at higher droplet solid fractions overturned the positive effects of rapid cooling on microsegregation.

5.2 Future Work

Based on the findings in this study, several areas can be further explored to develop the UDS forming process for rapid prototyping applications. They include preventing porosity formation in the deposit and designing deposition strategies for a uniform local solidification rate and desired deposit geometry.

Section 4.5 described the porosity defects found in the deposits from Experiments C and D as macroscopic voids due to incomplete droplet consolidation on the deposit surface. Comparing the deposit thermal history of the porous deposits to the other deposits revealed that controlling the deposit thermal state alone is not enough to prevent porosity. The evidence suggests that the droplet thermal state also affects porosity by altering the amount of droplet deformation upon impact with the deposit surface. It is possible that increasing the liquid content on the deposit surface may be sufficient to fill in voids created by the splats. However, this might adversely affect the coarsening of the deposit microstructure. Therefore, it is necessary to examine the combined effects of droplet and deposit thermal state to determine the conditions that prevent porosity formation, while minimizing deposit solidification rate. This may involve modeling the discrete droplet impact behavior as part of the deposit thermal model.

Most likely, practical applications of the UDS forming process will require thicker deposits with more sophisticated geometries than those sprayed in this experimental study. As the deposition time increases, the thermal gradient within the deposit will also increase and lead to inhomogeneous microstructure and residual internal stress. Therefore, different schemes of intermittent deposition, active cooling with forced convection, or planned substrate motion, are necessary to maintain a uniform local solidification rate. The effectiveness of these schemes can be simulated in the 2-D axisymmetric model by altering the boundary conditions and deposit growth rate. To predict the deposit growth rate *a priori*, it is necessary to model the mass flux distribution of the spray and the substrate motion.

REFERENCES

ABAQUS/Standard User's Manual, Version 6.1, 2000, Hibbitt, Karlsson & Sorenson, Inc., Pawtucket, RI.

Acquaviva, P., 1995, "Modeling of deposit solidification in droplet based manufacturing," M.S. thesis, Massachusetts Institute of Technology, Cambridge, MA.

Amon, C.H., Beuth, J.L., Weiss, L.E., Merz, R., and Prinz, F.B., 1998, "Shape deposition manufacturing with microcasting: processing, thermal and mechanical issues," *Journal of Manufacturing Science and Engineering*, vol. 120, pp. 656-665.

Annavarapu, S., Apelian, D., and Lawley, A., 1990, "Spray casting of steel strip: process analysis," *Metallurgical Transactions A.*, vol. 21A, pp. 3231-3256.

Annavarapu, S. and Doherty, R.D., 1995, "Inhibited coarsening of solid-liquid microstructures in spray casting at high volume fractions of solid," *Acta Metall. Mater.*, vol. 43, no. 8, pp. 3207-3230.

Ashok, S., 1993, "Evolution of microstructure of Cu-4wt%Zr alloy formed by spray casting," *International Journal of Rapid Solidification*, vol. 7, pp. 283-293.

Bianchi, M.V.A. and Viskanta, R., 1995, "Thermal conductivity of the mushy zone and the completely solidified region during the solidification of a binary alloy," *Proceedings of the ASME Heat Transfer Division*, vol. 317-2, pp. 323-331.

Smithells Metals Reference Book, 7th ed., 1992, eds. Brandes, E.A. and Brook, G.B., Butterworth-Heinemann Ltd, Oxford, UK.

Brinksmeier, E. and Schünemann, M., 2001, "Generation and forming of spray-formed flat products," *Journal of Materials Processing Technology*, vol. 115, pp.55-60.

Butzer, G. and Bowen, K., 1998, "Spray forming aerospace alloys," *Advanced Materials & Processes*, vol. 3, pp. 21-23.

Chen, C.-A., 1996, "Droplet solidification and its effects on deposit microstructure in the uniform droplet spray process," Ph.D. Thesis, Massachusetts Institute of Technology, Cambridge, MA.

Chun, J.-H. and Passow, C.H., 1993, "Droplet-based manufacturing," *Annals of CIRP*, vol. 42, pp. 235-238.

Dai, S.L., Delplanque, J.-P., and Lavernia, E.J., 1998, "Microstructural characteristics of 5083 Al alloy processed by reactive spray deposition for net-shape manufacturing," *Metallurgical and Materials Transactions A*, vol. 29A, pp. 2597-2611.

DeGaspari, J., 2000, "Tools to die for," *Mechanical Engineering*, vol.3, pp. 54-57.

Doherty, R., Cheng, C., and Kohler, L., 1997, "Modeling and microstructure development in spray forming," *International Journal of Powder Metallurgy*, vol. 33, pp. 50-60.

Fuxiao, Yu, Jianzhong, Cui, Ranganathan, S., and Dwarakadasa, E.S., 2001, "Fundamental difference between spray forming and other semisolid processes," *Materials Science & Engineering*, A304-306, pp.621-626.

Gougeon, P. and Moreau, C., 1993, "In-flight particle surface temperature measurement: influence of the plasma light scattered by the particles," *Journal of Thermal Spray Technology*, vol. 2(3), pp. 229-234.

Grant, P.S., Kim, W.T., and Cantor, B., 1991, "Spray forming of aluminum-copper alloys," *Materials Science and Engineering A*, vol. 134A, pp. 1111-1114.

Hu, Ji-dih, 2001, Engineer, Luxtron Corporation, Santa Clara, CA., technical support through email correspondence.

Hu, H., Lee, Z.H., White, D.R., and Lavernia, E., 2000, "On the evolution of porosity in spray-deposited tool steel," *Metallurgical and Materials Transactions A*, vol. 31A, pp. 723-733.

Hultgren., R., Desai, P.D., Hawkins, D.T., Gleiser, M., Kelley, K.K., 1973, *Selected Values of the Thermodynamic Properties of Elements*, ASM, Metals Park, OH.

Incropera, F.P. and De Witt, D.P., 1990, *Fundamentals of Heat and Mass Transfer*, John Wiley & Sons, Inc., New York.

Kattamis, T.Z. and Voorhees, P.W., 2001, "Coarsening of solid-liquid mixtures: a review," *Proceedings of the Merton C. Flemings Symposium on Solidification and Materials Processing*, eds. Abbaschian, R. et al., pp. 119-125.

Kirkwood, D.H., 1985, "A simple model for dendrite arm coarsening during solidification," *Materials Science and Engineering*, vol. 73, pp. L1-L4.

Kurz, W. and Fisher, D.J., 1998, *Fundamentals of Solidification*, Trans Tech Publications Ltd., Switzerland.

Leatham, A.G. and Lawley, A., 1993, "The osprey process: principles and applications," International Journal of Powder Metallurgy, vol. 29, pp. 321-329.

Liang, X. and Lavernia, E.J., 1994, "Evolution of interaction domain microstructure during spray deposition," *Metallurgical and Materials Transactions A*, vol. 25A, pp. 2341-2355.

Manson-Whitton, E.D., Stone, I.C., Grant, P.S., Cantor, B., and Blackham, S., 1998, "Solid/liquid coarsening behavior of spray formed IN718," *Solidification*, pp. 415-425, eds. S.P. Marsh et al., TMS, Warrendale, PA.

Rapid Solidification Processing: Principles and Technologies, 1977, eds. Mehrabian, R., Kear, B.H., and Cohen, M., Claitor's Publishing Div., Baton Rouge, LA.

Mingard, K.P., Alexander, P.W., Langridge, S.J., Tomlinson, G.A., and Cantor, B., 1998, "Direct measurement of sprayform temperatures and the effect of liquid fraction on microstructure," *Acta Mater.*, vol. 46, no. 10, pp. 3511-3521.

Mortensen, A., 1989, "On the influence of coarsening on microsegregation," *Metallurgical Transactions A.*, vol 20A, pp. 247-253.

Mortensen, A., 1991, "On the rate of dendrite arm coarsening," *Metallurgical Transactions A.*, vol. 22A, pp. 569-574.

Okamoto, T. and Kishitake, K., "Dendritic structure in unidirectionally solidified aluminum, tin, and zinc base binary alloys," *Journal of Crystal Growth*, vol. 29, pp. 137-146.

Pasandideh-Fard, M., Bhola, R., Chandra, S., and Mostaghimi, J., 1998, "Deposition of tin droplets on a steel plate: simulations and experiments," *International Journal of Heat and Mass Transfer*, vol. 41, pp. 2929-2945.

Passow, C.H., 1992, "A study of spray forming using uniform droplet sprays," M.S. Thesis, Massachusetts Institute of Technology, Cambridge, MA.

Poirier, D.R. and Nandapurkar, P., 1988, "Enthalpies of a binary alloy during solidification," *Metallurgical Transactions A*, vol. 19A, pp. 3057-3061.

Shukla, P., Mandal, R.K., and Ojha, S.N., 2001, "Microstructural modification induced by spray forming of Al-Cu alloys," *Materials Science and Engineering*, A304-306, pp. 583-586.

Singer, A.R. and Evans, R. W., 1983, "Incremental solidification and forming," *Metals Technology*, vol. 10, pp. 61-68.

Srivastava, A.K., Anandani, R.C., Dhar, A., and Gupta, A.K., 2001, "Effect of thermal conditions on microstructural features during spray forming,"*Materials Science and Engineering*, A304-306, pp. 587-591.

Touloukian, Y. S., *Thermophysical Properties of Matter*, vol. 11, Purdue University, West Lafayette, IN, 1970-1975.

Underhill, R.P., Grant, P.S., Bryant, D.J., and Cantor, B., 1995, "Grain growth in spray-formed Ni superalloys," *Journal of Materials Synthesis and Processing*, vol. 3, no. 3, pp. 171-179.

Waldvogel, J.M. and Poulikakos, D., 1997, "Solidification phenomena in picoliter size solder droplet deposition on a composite substrate," *International Journal of Heat and Mass Transfer*, vol. 40, pp. 295-309.

Wang, G.-X. and Matthys, E.F., 1996, "On the heat transfer at the interface between a solidifying

metal and a solid substrate," *Melt Spinning, Strip Casting and Slab Casting*, pp. 205-236, eds. Matthys, E.F. and Truckner, W.G., TMS, Warrendale, PA.

Xu, Q. and Lavernia, E.J., 1999, "Microstructural evolution during the initial stages of spray atomization and deposition," *Scripta Materialia*, vol. 41, no. 5, pp. 535-540.

Xu, Q., Gupta, V.V., and Lavernia, E.J., 2000, "Thermal behavior during droplet-based deposition," *Acta Mater.*, vol. 48, pp. 835-849.

Zentner, L.K., DeWitt, D.P., White, D.A., and Gaskell, D.R., 1994, "Computer algorithms for radiometric measurement of temperature during the galvanneal process," *Metallurgical and Materials Transactions B*, vol. 25B, pp. 459-462.

Zhou, Y., Wu, Y., and Lavernia, E.J., 1997, "Process modeling in spray deposition: a review," *International Journal of Non-Equilibrium Processing*, vol. 10, pp. 95-183.

Appendix A

The phase diagram for the Zn-Sn alloy system used in the deposition experiments is shown below in Figure A.1.
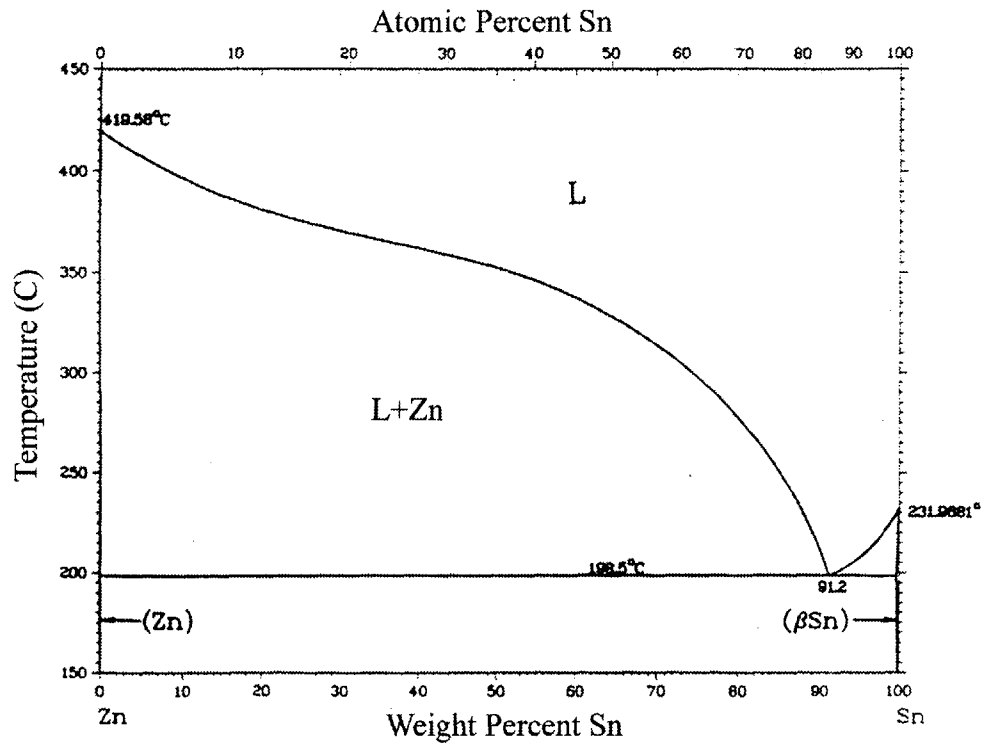

Figure A.1. Equilibrium phase diagram for Zn-Sn alloy system [Brandes and Brook 1992].

The Zn-rich liquidus curve is approximated as a polynomial function of the solute concentration in the liquid, C_l :

$$T_l = 419.58 - 323.7C_l + 757.1C_l^2 - 728.5C_l^3$$

The enthalpies (J/g-atom) of pure Sn and Zn are given as functions of temperature (K) [Hultgren et al. 1973].

$$H_{Sn,l} = -585.76 + 28.03T_k - 3.02 \times 10^5 T^{-1}$$

$$H_{Zn,l} = -3556.4 + 31.38T$$

$$H_{Sn,s} = -7243 + 21.6T_k + 9.08 \times 10^{-3}T^2$$

$$H_{Zn,s} = -7121.17 + 22.38T_k + 5.02 \times 10^{-3}T^2$$

The densities (kg/m^3) of pure Sn and Zn are given as functions of temperature (°C) [Brandes and Brooks 1992].

$$d_{Sn,l} = 7142 - 0.6127T$$

$$d_{Sn,s} = 7322 - 0.567T$$

$$d_{Zn,l} = 7036 - 1.1T$$

$$d_{Zn,s} = 7140 - 0.746T$$

The thermal conductivities (W/mK) of pure Sn and Zn are given as functions of temperature (°C) [Brandes and Brooks 1992].

$$k_{Sn,l} = 25.3182 + 0.0202T$$

$$k_{Sn,s} = 65.6393 - 0.0279T$$

$$k_{Zn,l} = 25.3089 + 0.0576T$$

$$k_{Zn,s} = 113.72 - 0.0437T$$